MASTER

Heating mechanisms in rf-driven ultracold plasmas

van der Straten, K.W.C.A.

Award date:
2014

Eindhoven University of Technology
Department of Applied Physics
Coherence and Quantum Technology

Heating mechanisms in rf-driven ultracold plasmas

K.W.C.A. van der Straten

Supervisors:
Dr. ir. G. J. H. Brussaard
Prof. dr. ir. O. J. Luiten

December 7, 2013

Abstract

Ultracold plasmas (UCPs) are created by photo-ionization of a cloud of laser-cooled atoms, and have initial electron temperatures in the range 1-100 K and initial ion temperatures in the range 0.001-1 K. As a consequence UCPs can be in the strongly coupled regime, where the typical Coulomb interaction between the particles exceeds the thermal energy of the particles; a clear distinction with conventional plasmas. UCPs are not stable systems and the electron and ion temperature will rise during their evolution. The introduction of a disturbing rf-field to the UCP is expected to speed up the heating of the plasma.

In this thesis the intrinsic electron heating mechanisms are studied as well as the heating mechanisms induced by an external rf field. Numerical simulations were performed with the General Particle Tracer code and compared to analytical theories. Two intrinsic heating mechanisms were studied: disorder-induced heating and heating by three-body recombination (TBR). Disorder-induced heating arises due the random initial positions of the electrons. An excess of potential energy exists in the electron distribution which is rapidly converted into thermal energy. The time scale of disorder-induced heating was found to be on the order of the inverse Mie-frequency, confirming analytical theories. TBR was identified in the simulations and the TBR heating rate was found to agree well with analytical models.

Two rf-induced heating mechanisms were studied: collisionless energy absorption and collisional absorption. Collisionless absorption of the electrons in the plasma was modeled as an electron cloud oscillating in an electrostatic plasma potential perturbed by an oscillating rf field. Two proposed plasma potentials were studied, for different rf field frequencies. First the collisionless absorption was calculated classically as well as quantum-mechanically in the 1D harmonic potential. The expected irreversible energy absorption was at the resonance frequency of the potential and reversible energy absorption for other field frequencies, also confirmed by GPT simulations. For the more realistic anharmonic 3D error potential a net absorption was found that depended strongly on the ratio of the oscillation frequency of the electron cloud to the external field frequency.

Collisional absorption was studied in a regime that collisionless absorption is negligible. Absorption arises because the electrons, which are oscillating at the rf field frequency, are deflected by the Coulomb fields of the ions. The amount of collisional absorption was found to depend strongly on the amplitude of the rf field. It was found that the rf field effectively suppresses the electron-ion collision frequency as a function of increasing field amplitude, confirming analytical theories. For low to moderate amplitudes the amount of energy absorption increases, but less than one might intuitively expect due to the decrease in collision frequency. For very strong field amplitudes the energy absorption even decreases as a function of field amplitude.

Contents

Introduction

The plasma state is one of the four fundamental states of matter and the most common phase of ordinary matter in our universe. A plasma is a substance containing many free electrons and ionized atoms whose macroscopic behavior is governed by the long-range Coulomb forces. There are two fundamental parameters describing the macroscopic behavior of a plasma: the particle electron and ion densities, n_e an n_i, and the electron and temperature ,T_e and T_i [1]. An overview showing different types of plasma classified by electron temperature and electron density is shown in figure 1.1. The diagonal lines show different values of the Coulomb interaction parameter Γ. This parameter quantifies the ratio of the Coulombic interaction energy with the thermal energy of the particles:

$$\Gamma = \frac{e^2}{4\pi\epsilon a_0 k_b T} \tag{1.1}$$

where $a_0 = [3/(4\pi n)]^{1/3}$ is the Wigner-Seitz radius which can be regarded as the manoeuvring room of a particle in the plasma or as half the average inter-particle distance in the plasma [2].

One distinct group of the plasmas shown in figure 1.1 will be the central subject in this thesis: the ultracold plasma (UCP). UCPs have electron temperatures smaller than 100 K and ion temperatures smaller than 1 K. The main distinction between UCPs and other plasmas is in the Coulomb parameter Γ. Ultracold plasmas can be in the strongly coupled regime, defined by $\Gamma \gg 1$, in which the Coulomb interaction between the particles exceeds the thermal energy.

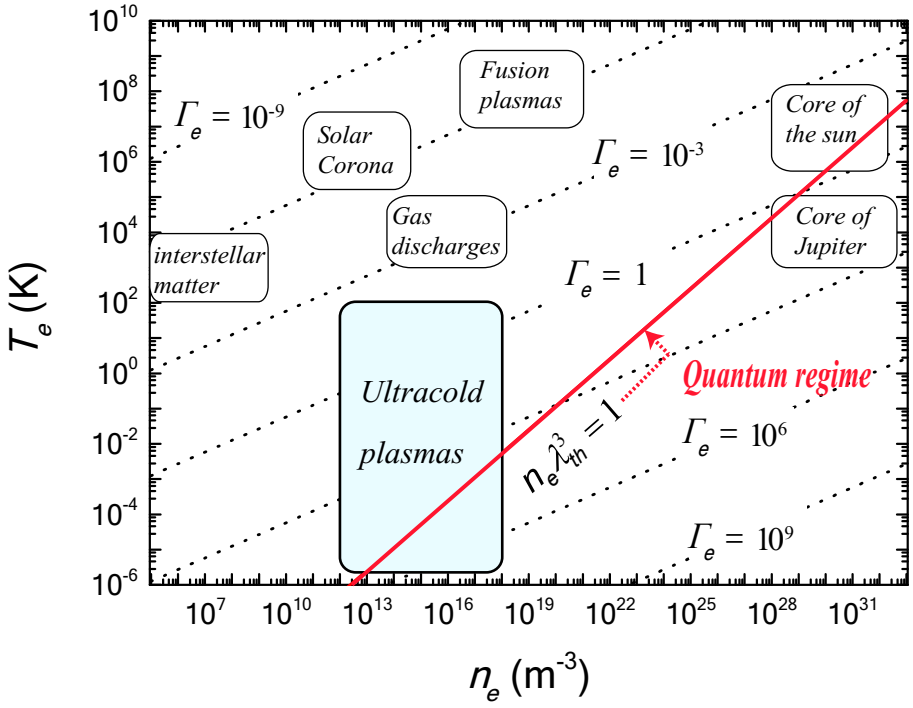

Figure 1.1: *Overview of plasmas in the electron density-temperature parameter plane [2].*

1.1 Creation and evolution of ultracold plasmas

Ultracold plasmas are not created by ionizing collisions between charged particles, but by photo-ionization of a cloud of ultracold atoms, which succeeded for the first time in 1999 [3]. First, an atomic gas is trapped and cooled in a magneto-optical trap, which consists of several laser beams to cool the atoms and a magnetic field to trap the atoms [4]. In such a configuration a gas with particle density $n < 10^{18}$ m^{-3} can be cooled to temperatures as low as $T \approx 100$ μK. The laser-cooled gas has a Gaussian density, with rms-sizes smaller than 1 mm and a Wigner-Seitz radius $a_0 \gtrapprox 1$ μm.

Most ultracold plasma experiments are based on a two-photon ionization, where one photon of the cooling laser excites atoms to the upper level of the cooling transition [2]. A second pulsed narrow-band dye laser is used to excite the electrons above the ionization threshold, giving the electrons a kinetic energy approximately equal to the difference between the photon energy and the required ionization energy. The minimal initial kinetic energy is determined by the bandwidth of the laser, which can result in initial electron temperatures as low as $T_e \approx 100$ mK. The ion temperatures is approximately equal to the temperature of the atoms before photo-ionization.

The creation of the plasma is illustrated in figure 1.2.

Creation of an ultracold plasma in a magneto-optical trap

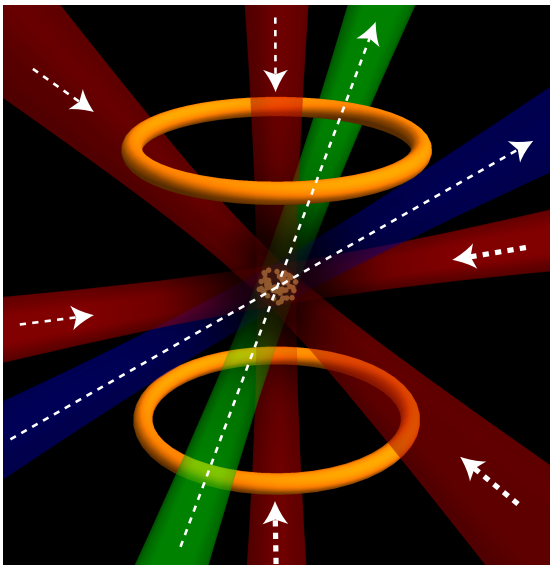

Figure 1.2: *Red beams: Three pairs of counterpropagating laser-beams (red beams) in combination with the magnetic field due to a pair of coils (orange rings) in anti-Helmholtz configuration cool and trap the atom cloud.*
The trapped atom cloud is excited to the upper level of the cooling transition (blue beam) and ionized by pulsed narrow-band dye laser (green beam).
N.B. : colors are not related to wavelengths. Image from: **[5]**

The essential dynamics of an ultracold plasma are captured by classical physics, despite their low particle temperatures. The densities of ultracold plasma are low enough such that the quantum-mechanical wave functions do not overlap. The importance of quantum effects can be described by the Brückner parameter r_s [6], which is the ratio between the Wigner-Seiz radius and the Bohr radius $a_B = 4\pi\varepsilon_0\hbar^2/m_e e^2$. For quantum effects to be relevant $r_s < 1$, while for UCPs r_s values are in the range $r_s \approx 10^5 - 10^6$.

A second parameter used to describe the importance of quantum effects is the thermal De Broglie wavelength $\lambda_{th} = h/\sqrt{2\pi m_e k_b T_e}$ where h is the Planck constant. Quantum-mechanical many-body phenomena will occur if the thermal wavelength is larger than the Wigner-Seitz radius a_0, or differently expressed as $\lambda_{th}^3 n_e > 1$. For electrons with the aforementioned lowest experimentally accessible temperature $T_e = 100$ mK, the thermal wavelength equals $\lambda_{th} \approx 0.2$ μm. This is already one order of a magnitude smaller than the corresponding Wigner-Seitz radius $a_0 \approx 1$ μm at $T_e = 100$ mK.

The boundary at which quantum-mechanical behavior becomes significant, $n_e\lambda_{th}^3 = 1$, is given by the red line in figure 1.1.

An ultracold plasma is not a stable system and evolves in three stages after its creation as shown in figure 1.3. The fastest process is the equilibration of the electrons, because of their relatively small mass and high kinetic energy. This takes place on a time scale related to the inverse electron plasma frequency $\omega_{p,e}^{-1} \sim \sqrt{m_e}$ which is typically in the nanosecond range. The electron temperature quickly increases due to two heating mechanisms: disorder-induced heating and heating by electron-ion three-body recombination. The first of these processes arises from an excess of potential energy in the electron distribution and the second is related to the formation of highly-excited Rydberg atoms. Both mechanisms will be studied in detail in chapter 3.

The ions equilibrate on the microsecond timescale due to their higher mass, related to the inverse ion plasma frequency $\omega_{p,i}^{-1} \sim \sqrt{m_i}$. In a ultracold rubidium plasma the ratio between the ionic and electronic time scales equals $\frac{\omega_{p,i}^{-1}}{\omega_{p,e}^{-1}} = \sqrt{\frac{m_i}{m_e}} \approx 395$. The main heating mechanism in this stage is ionic disorder-induced heating.

In the third stage the plasma expands into the surrounding vacuum, driven by the thermal pressure of the electrons and ions [2], and falls apart.

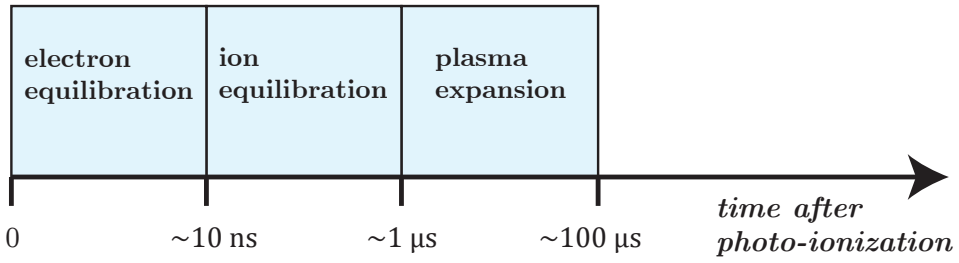

Figure 1.3: *The three different time scales in the dynamics of an ultracold plasma.*

1.2 Significance and applications of ultracold plasmas

The main interest in ultracold plasma is due to the fact that they can provide access to the strongly coupled regime, defined by $\Gamma \gg 1$. Standard plasma physics concepts such as Debye screening are all based on the assumption that the thermal energy of the particles exceeds the average Coulomb potential between the particles. Therefore it is necessary to develop new analytical theories and numerical tools to describe these systems.

Strongly coupled conditions can also be found in some high-density plasmas such as in laser-ionized clusters, inertial confinement fusion and astrophysical plasmas [7]. The dynamics of these plasmas evolve on the atto- to femtosecond timescales which makes

it difficult to study them. Ultracold plasmas on the other hand evolve on the timescale of picoseconds to microseconds, due to their much lower density. On these timescales it is possible to study an UCP using time-resolved techniques such as charged-particle detection and absorption imaging [8]. Therefore, UCPs could serve as a toy model to study experimentally the phenomena occurring in other, less accessible strongly coupled systems.

The ultracold temperature of UCPs make them interesting for new sources of high-brightness electron and ion beams, due to their low temperatures. Accelerator structures are constructed around a UCP set-up to extract an ultracold electron beam as well as an ultracold ion beam [9].

Theoretical studies by Peter Smorenburg et. al. showed the possibility of another remarkable application in accelerator physics: to accelerate the neutral UCP as a whole with ion energies in the range of keV [10]. The principles of this mechanism are in the radiation effects on the electrons and are illustrated in figure 1.4. An incoming a electromagnetic wave is imposed on an ultracold plasma of R_b in this case. All the electrons in the plasma will oscillate coherently if the wavelength of the incoming wave is larger than the size of the plasma. As a result the oscillating electrons will emit dipole radiation and the incoming EM wave will lose momentum. The electrons on the other hand will increase their momentum in order to conserve momentum of the total system consisting of the incoming wave and the plasma. The electrons will pull the ions with them leading to a net acceleration of the plasma as a whole. The stability of the plasma is strongly dependent on the temperature of the plasma. Therefore it is important to study the initial heating of the plasma during its acceleration. Due to their much lower mass compared to the ions, this initial heating is governed by the electrons.

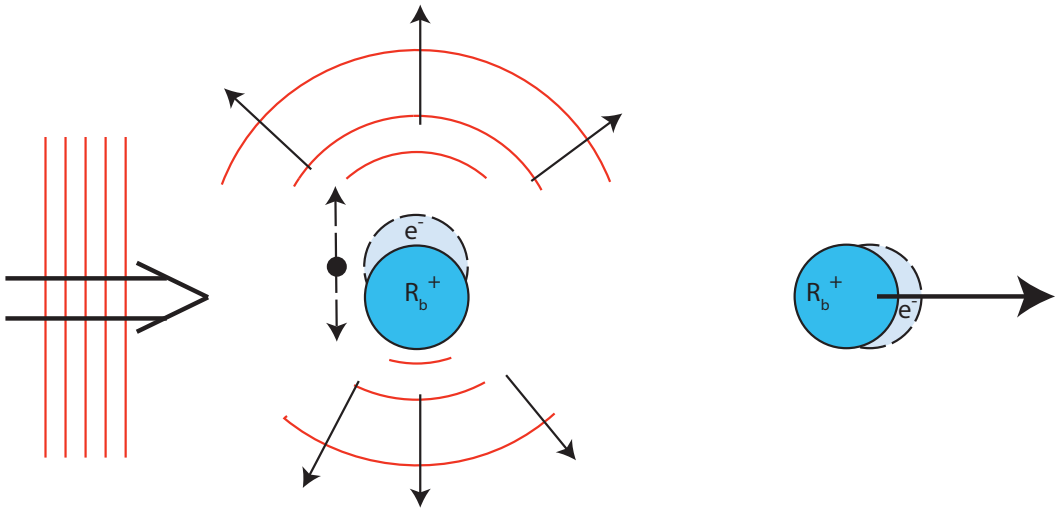

Figure 1.4: *The three different time scales in the dynamics of an ultracold plasma.*

1.3 This thesis

The goal of this thesis is to study the *electron* heating mechanisms of ultracold plasmas by particle tracking simulations. Therefore, the first stage of the plasma evolution, illustrated in figure 1.3, will be studied. The General Particle Tracer (GPT) code [11] makes it possible to simulate the particle paths taking into account all pairwise Coulombic interactions; a task impossible to succeed analytically. Details of the GPT code will be explained in chapter 2. In chapter 3 the heating mechanisms will be studied in a plasma without any external fields. The focus will be on two electron heating mechanisms: disorder-induced heating and three-body recombination.

In chapter 4 and 5 an external rf field will be introduced and the induced energy absorption mechanisms will be studied. In chapter 4, an absorption mechanism will be studied that does *not* depend on individual electron and ion interaction: collisionless absorption. Collisionless absorption arises because the rf field disturbs the trajectories of the electrons in the plasma.

A second rf-induced heating mechanism, that will be studied in chapter 5, depends solely on the electron-ion interaction: collisional absorption. The nature of this absorption mechanism is that the electrons oscillating in the rf field are deflected by the Coulomb fields of the ions.

In chapter 6 general conclusions from the foregoing chapters will be drawn as well as suggestions for future work.

Simulation software

The program used for the simulations is *General Particle Tracer 3.10* written by S.B. van der Geer and M.J. de Loos [11]. The GPT-code is a simulation method to track the 3D positions and velocities of a set of charged particles, taking into account the inter-particle (Coulombic) forces as well as external fields. It uses an embedded fifth order Runge-Kutta driver with adaptive stepsize control.

2.1 Coulomb interactions

GPT uses the Coulomb model the calculate the inter-particle forces. Three simplifications are made in this Coulomb model.

The first approximation is that magnetic fields produced by the moving charges are ignored. This approximation is appropriate as long as the velocity differences between the particles in a set are significantly smaller than the speed of light. In an ultracold plasma the electrons velocities are on the order $10^3 - 10^4$ m/s such that the Lorentz force that an electron i experiences due to the *relative* velocity of a second electron or ion j, $\vec{v_{rel}} = \vec{v_j} - \vec{v_i}$ is small compared to the inter-particle Coulomb force: $e\vec{v_{rel}} \times \vec{B_j} \ll q_j \vec{E_j}$.

Secondly, the Coulomb model is based on instantaneous forces. The forces on a certain test particle depend on the *instantaneous* positions of the other particles. If one other electron moves the force at the test particles changes immediately. However, information can not travel faster than light according to special relativity and retarded positions of the other particles should be used formally. Again, this assumption is appropriate as long as the velocity differences between a test-particle and the other particle are small compared with the speed of light.

The third approximation is that the radiation fields of accelerating charges are absent. If an external rf field is applied the electrons will start to oscillate and emit radiation. The significance of these radiation fields in an rf-driven ultracold plasma will be discussed in section 2.3.

All the particle interactions are calculated in the rest-frame of the particle set, which is the frame in which the total momentum is zero. It has a velocity $\vec{\beta}_0 = \frac{\sum_i \gamma_i m_i \vec{v}_i / c}{\sum_i \gamma_i m_i}$ with γ_i the Lorentz factor of the particle i in the rest frame of the particle set. So $\vec{\beta}_0$ is the velocity weighted with the relativistic mass $\gamma_i m_i$ and it has a Lorentz factor with respect to the laboratory frame of $\gamma_0 = 1/\sqrt{1 - (\vec{\beta}_0)^2}$.

The particle coordinates in the rest frame $\vec{r_i}'$ are calculated in the following way:

$$\vec{r_i}' = \vec{r_i} + \frac{\vec{r_i} \cdot \gamma_0 \vec{\beta_0}}{\gamma_0 + 1} \gamma_0 \vec{\beta_0} \tag{2.1}$$

where $\vec{r_i}$ are the coordinates of the particle i in the lab frame. After that the Coulomb model is used to calculate the electric field $\vec{E_i'}$ that the particle i experiences in the rest frame:

$$\vec{E_i'} = \left[\sum_{j \neq i} \frac{q_j \left(\vec{r_i}' - \vec{r_j}' \right)}{4\pi\varepsilon_0 \left(\left| \vec{r_i}' - \vec{r_j}' \right|^2 + R^2 \right)^{3/2}} + \vec{E}_{ext} + \vec{v_i}' \times \vec{B}_{ext} \right] \tag{2.2}$$

where $\vec{E}_{ext}$ and $\vec{B}_{ext}$ are external fields and R is a Coulomb round-off parameter used to avoid singularities in the computations. Figure 2.1 shows the effect of the use of the round-off parameter on the following scaled potential between the particles 1 and 2:

$$\frac{U_{pot}}{U_0} = \frac{U_{pot}}{\frac{e^2}{4\pi\epsilon_0 a_0}} = -\frac{1}{\sqrt{\frac{\left| \vec{r}_1' - \vec{r}_2' \right|^2}{a_0^2} + \left(\frac{R}{a_0} \right)^2}} = -\frac{1}{\sqrt{\frac{r'^2}{a_0^2} + \epsilon^2}} \tag{2.3}$$

where a_0 is the Wigner-Seitz radius and $\epsilon = \frac{R}{a_0}$ is the round-off parameter scaled with the Wigner-Seitz radius. The depth of the potential follows immediately by applying $r = 0$: $U_{pot}/U_0 = 1/\epsilon = a_0/R$.

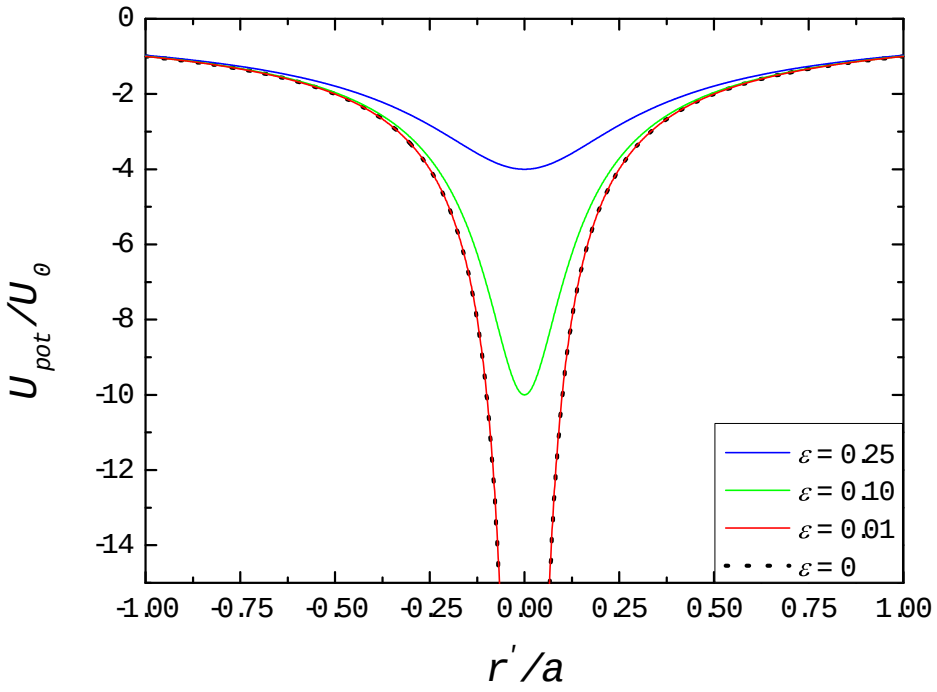

Figure 2.1: *Electron-ion potential with four different values for the round-off parameter ϵ.*

In the simulations a value of $\epsilon = 0.01$ will be used, implying that the Coulomb round-off parameter is equal to $R = \frac{a_0}{100}$, is considered to be sufficient to capture the essential dynamics in the plasma.

The calculated electric field $\vec{E}_i'$ from equation (2.2) is transformed back into the laboratory frame to obtain the required $\vec{E}$ and $\vec{B}$ fields for tracking:

$$\begin{aligned} \vec{E}_i &= \gamma_0 \left[\vec{E}_i' - \frac{\gamma_0}{\gamma_0 + 1} \left(\vec{\beta}_0 \cdot \vec{E}_i' \right) \vec{\beta}_0 \right] \\ \vec{B}_i &= \frac{\vec{\beta}_0 \times \vec{E}_i'}{c} \end{aligned} \tag{2.4}$$

where the left-hand side of the second equation indicates that a magnetic field can be present in the *laboratory frame*, provided the particle set has a significant velocity $\vec{\beta}_0$. The magnetic field $\vec{B}_i$ in the *laboratory* frame is just a relativistic effect and is negligible if $\vec{\beta}_0 \ll 1$.

For an approximately stationary plasma ($\vec{\beta}_0 \ll 1$) with non-relativistic particles the expected result $\vec{E}_i = \vec{E}_i'$, $\vec{B}_i = 0$ is found.

2.2 The Barnes-Hut algorithm

The program has a number of built-in elements to calculate the Coulomb interactions in equation (2.2) in an efficient way, each optimized for a different application. In this report the *Spacecharge3Dtree* element will be used that uses a Barnes-Hut algorithm which scales in computing time as $N \log N$, with N the total number of particles in the simulation [12].

The Barnes-Hut algorithm calculates the force by grouping particles together in a hierarchical way. The interactions between near neighbors are calculated individually while distant charges are grouped together in increasingly larger clusters as a function of distance, thereby speeding up the total computation time.

The principle is shown in figure 2.2. First the algorithm splits the volume around the particles into successively smaller octants until each octant cell contains 1 or 0 particles. All the particles are stored in the so-called octree, illustrated in the right of figure 2.2, where each cell forms an internal node of the tree. Each internal node represents the group of particles beneath it and stores the center of mass and the total mass of all its children. For example, the topmost node represents the whole space and its four children represent the four octants of the whole space.

Not all the interactions of a particle i with the other particles are calculated individually; the hierarchical structure of the octree is used to approximate the net force on the particle i. A dimensionless parameter θ is set to decide whether an internal node of the tree is far enough away from the particle i to approximate the exerted force. The parameter is given by $\theta = \Delta x/d$ where Δx is the width of the region represented by the internal node and d is the distance from the particle i to the internal node. The parameter θ is calculated for each node in the tree and if the value of θ lies below a certain threshold value θ_{thr}, only the interaction of the particle i with the center of mass of that specific node is considered. A threshold value of $\theta_{thr} = 0$ results in a complete point-to-point calculation at the expense of a much longer computation time. A threshold value of $\theta_{thr} = 1$ is generally considered to be sufficiently small to capture the essential dynamics for Coulombic interactions [12].

An example is shown in figure 2.2. The center of mass of the purple dashed cell is far enough away from particle i, such that only the interaction with the center of mass of the purple cell is considered. The orange dashed cell on the other hand is close enough to the particle i, such that the interactions with the particles in the orange cell are calculated individually.

2.3 Significance of missing radiation effects

If an external field is applied to a plasma the electrons will start to oscillate and as a consequence will start to emit radiation. As a result the electron will lose energy and experiences a recoil force: the well-known radiation reaction [13].

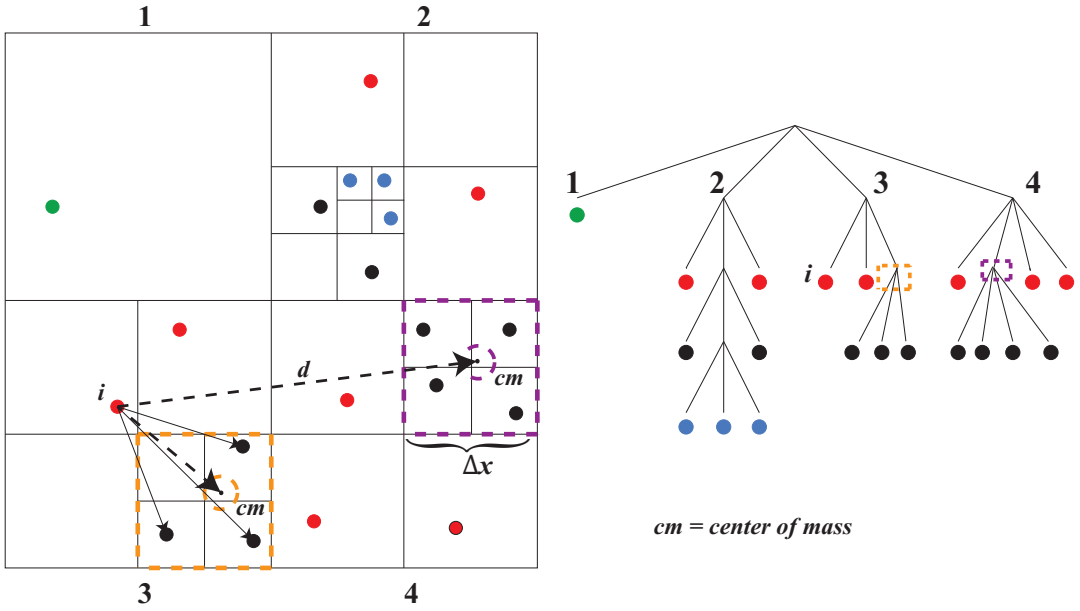

Figure 2.2: *Principle of the Barnes-Hut algorithm.*

The time-averaged energy of an electron in an oscillating EM field is given by:

$$U_e = \langle \frac{1}{2} m_e v(t)^2 \rangle = \frac{e^2 E_0^2}{4 m_e \omega_d^2} \equiv U_p \tag{2.5}$$

where U_p is the so-called ponderomotive potential.

The amount of lost or radiated energy per unit time P_{rad} can be found from the Larmor formula $P_{rad} = (\mu_0 e^2/6\pi c)a^2$ with a the acceleration of the electron [14, 13]. In an rf field $E_0 \cos(\omega_d t)$ the acceleration of an electron is given by $a = -(eE_0/m_e)\cos(\omega_d t)$, such that the time-averaged P becomes $\langle P \rangle = \mu_0 e^4 E_0^2/(12\pi c m_e^2) = (\omega_d^2 e^2 \mu_0)/(3\pi m_e c) U_p$.

If the total amount of lost radiation in a time interval is negligible compared to the typical energy of the electrons, then the effects of the radiation reaction on the motion of the electrons will be negligible. The simulation time in this thesis is typically about $t_{sim} = 200\pi/\omega_d$ with ω_d the frequency of the external rf field and this corresponds to a total amount of radiated energy $U_{rad} = \langle P \rangle \cdot t_{sim} = (200\omega_d e^2 \mu_0)/(3 m_e c) U_p$. The significance of the radiated energy is: $U_{rad}/U_p = (200 e^2 \mu_0)/(3 m_e c)\omega_d \approx 10^{-20} \cdot \omega_d$. In this thesis a field frequency in the range $\omega_d \sim 10^{10}$ rad/s will be used resulting in $U_{rad}/U_p \sim 10^{-10}$ and therefore the radiative effects on the motion of an electron are very small.

However, a few very subtle dielectric properties of the plasma are missing by using the Coulomb potentials for the interactions instead of the retarded Liénard-Wiechert potentials, despite the fact that the velocities of the particles are in the non-relativistic regime. For the case of an rf-driven ultracold plasma ponderomotive forces arise leading to an acceleration of the plasma as a whole [10]. This acceleration cannot be simulated with the GPT code, since the acceleration only arises if the retarded interaction potentials are used.

2.4 Limitations of the GPT software

The duration of the simulations in GPT is limited, but not only because of limited computation speed or time. The GPT code uses a Runge-Kutta solver which is not symplectic [11], which means that the total energy of the system is not exactly conserved in the simulations. Fluctuations in the total energy generally increase as a function of simulation time. The fluctuations can be suppressed in the electron equilibration phase from figure 1.3, but it is not possible to extend the simulation into the ionic equilibration phase or plasma expansion phase while conserving total energy. A maximum energy deviation of 1 % in the simulation was considered to be good enough to capture the essential dynamics.

In summary, the GPT code is a powerful tool to study the trajectories of the ions and electrons in the electron equilibration phase. However, it is important to be aware that for an ultracold plasma, even in the non-relativistic regime, some subtle dielectric properties are missing.

Intrinsic heating mechanisms in ultracold plasmas

In this chapter simulation results will be shown of the heating mechanisms in an ultracold Rb plasma, without any external fields. The initial electron and Rb^+ ion temperatures are 0 K in all the following simulations. The electrons and Rb^+ ions, $N_e = N_i = 2000$ of each, will be initialized inside a spherical volume with a radius $r_b = (\frac{3N_e}{4\pi n_e})^{1/3}$ with electron density $n_e = n_i$, as shown in figure 3.1. The initial electron and ion densities are chosen to be uniform but randomly distributed.

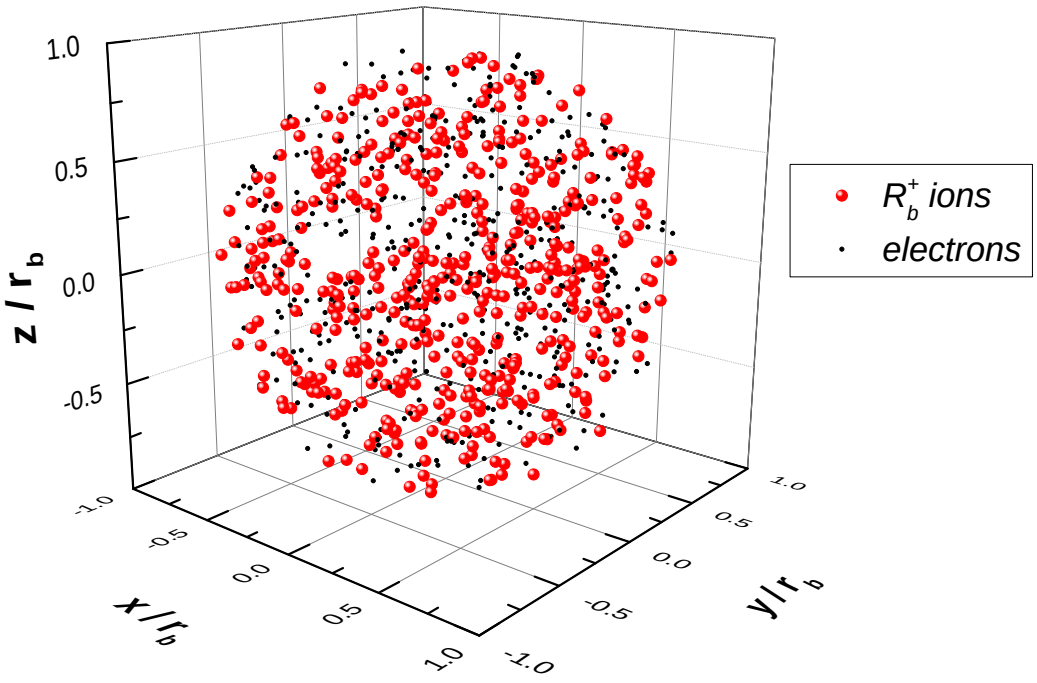

Figure 3.1: *The initial particle distribution which will be simulated.*

Scaled length and time units are used to reduce the number of parameters that define a simulation. The lengths are scaled by the Wigner-Seitz radius a_0 and time is scaled by the inverse of the plasma frequency ω_p^{-1}. Since the electron velocities $v_e \sim 10^3 - 10^4$, the non-relativistic equation of motion (2.2) can be used:

$$\frac{m_i}{m_e}\frac{\mathrm{d}^2\vec{x_i}}{\mathrm{d}\tau^2} = \frac{2}{3}\sum_{j\neq i}\frac{q_i q_j\,(\vec{x_i} - \vec{x_j}\,)}{e^2\,|\vec{x_i} - \vec{x_j}\,|^3} \tag{3.1}$$

where $\vec{x_i} = \vec{r_i}/a_0$ and $\tau = \omega_p t$. On the right-hand side the substitutions $\omega_p = \sqrt{n_e e^2/(m_e\varepsilon_0)}$ and $a_0 = (3/(8\pi n_e))^{\frac{1}{3}}$ have been used.

Similarly, the inverse coupling Coulomb parameter in equation (1.1) can be written as:

$$\Gamma_e^{-1} = \frac{1}{2}\left\langle\left(\frac{\mathrm{d}\vec{x_i}}{\mathrm{d}\tau}\right)^2\right\rangle \tag{3.2}$$

where the assumption of thermodynamic equilibrium $1/2m_e\langle v^2\rangle = 3/2k_bT_e$ has been used. The applicability of thermodynamic equilibrium will be discussed in section 3.1.2. Conclusively, the scaled equations of motion as well as the coupling parameter do not depend on the density.

The focus will be on the heating of the electrons. The typical times that will be used are $0 < \tau < 20$ and do not not extend into the regime in which the dynamics of the ions become relevant. The time scale on which effective ionic heating occurs is $\tau_i = \omega_{p,i}t \approx 1$ [2], which relates to electron time scale as: $\tau_i = \sqrt{m_i/m_e}\tau \approx 395\tau$. The energy drift in the simulation cannot be suppressed on the ionic timescales as mentioned in section 2, if all the electron interactions are taken into account. Different simplifying simulation models would be required to proceed into the ionic heating regime such as the use a Yukawa model where only the ions are traced and the presence of the electrons is taken into account by a Yukawa potential [15, 16].

In the next sections, two different heating mechanisms will be considered: disorder-induced heating in section 3.1 and three-body recombination in section 3.2.

3.1 Disorder-induced heating

Ultracold plasmas are created in a state far from equilibrium. Due to the nature of the photo-ionization process, both the ions and electrons are initially at random positions. As a result some of the charged particles will be rather close to each other leading to large interaction energies. An excess of potential energy exists compared to a crystalline state in which spatial correlations prevent the particles from being close to each other such as in laser-cooled ionic plasmas inside Penning traps [17].

As a result the particles redistribute themselves in order to diminish their excess of potential energy. Total energy is conserved in the system and therefore the kinetic energy

of the particles has to increase. This increase in kinetic energy is called disorder-induced heating.

The amount of increase in kinetic energy is estimated to be half of the conserved total energy. If thermal equilibrium is accomplished after the disordered-heating phase, the average kinetic energy $\langle U_{kin} \rangle$ equals the average potential energy $\langle U_{pot} \rangle$ of the electrons according to the law of equipartition of energy [18]. The Coulomb coupling parameter from equation (1.1) then approaches:

$$\Gamma_e = \frac{e^2}{4\pi\varepsilon_0 a_0} \frac{1}{k_b T_e} \approx \frac{\langle U_{pot} \rangle}{\langle U_{kin} \rangle} = 1 \tag{3.3}$$

in which the Wigner-Seitz radius is *half* the typical inter-particle distance defined by:

$$a_0 = \left(\frac{3}{4\pi n_{tot}} \right)^{1/3} = \left(\frac{3}{8\pi n_e} \right)^{1/3} \tag{3.4}$$

where n_e is the electron density and $n_{tot} = n_e + n_i$ in the plasma. The value of the coupling parameter Γ as defined in equation (3.3) depends on the existence of a well-defined electron temperature T_e. In situations far off equilibrium the average kinetic energy is usually taken as a measure for the temperature T_e.

3.1.1 Analytical model of disorder-induced heating

A relaxation time $t_{rel,e}$ is defined in which the electrons relax towards their equilibrium position at the end of the disorder-induced phase. This time can be estimated as the amount of time it takes an accelerated electron to cover a distance half the average inter-particle distance, which is equal to the Wigner-Seitz radius a_0. Such an electron will experience a typical Coulomb force of magnitude $\frac{e^2}{4\pi\epsilon_0} \frac{1}{a_0^2}$ leading to the equation of motion:

$$m_e \frac{\mathrm{d}^2 r}{\mathrm{d}t^2} = \frac{e^2}{4\pi\epsilon_0} \frac{1}{a_0^2} \tag{3.5}$$

Assuming an initial speed $v(0) = 0$ the covered distance Δr can be written as:

$$\Delta r = \frac{1}{2} \frac{e^2}{4\pi\epsilon_0 m_e a_0^2} t_{rel}^2 = a_0 \tag{3.6}$$

By substitution of a_0 from equation (3.4) the time to cover this distance is:

$$t_{rel,e} = \frac{1}{\omega_p/\sqrt{3}} = \frac{1}{\omega_m} \tag{3.7}$$

where $\omega_m = \omega_p/\sqrt{3}$ is the so-called Mie frequency. This is the eigenfrequency of the center-of-mass of the electron cloud in a spherical plasma. In chapter 4 a derivation of the Mie frequency will be given.

In light of the expression for the relaxation time the time $\tau = \omega_m t$ will be used in the remainder of the chapter, which obviously will not alter the dimensionless form of the equations of motion as defined in equation (3.1).

The derivations of the disorder-induced heating of the ions follows the same path as the electrons apart from the time scale. The time scale of the ionic heating will be on the order of the inverse ionic plasma frequency [19] related to the electron time scale as: $t_{rel,i} = \sqrt{3} \cdot \omega_{p,i}^{-1} = \sqrt{m_i/m_e} t_{rel,e} \approx 395 t_{rel,e}$.

In this time the ionic Coulomb parameter increases quickly to $\Gamma_i \gtrsim 1$, but this time the final value depends on the influence of the screening of the electron background which passed its disorder-induced phase long time before. The significance of the screening depends on the temperature of electron background as was shown analytically [20] as well as numerically and experimentally [15, 21].

3.1.2 Simulation results disorder-induced heating

GPT simulations were performed using a density $n_e = 1 \cdot 10^{-14}$ m^{-3}. The electron temperature in the plasma $T_e(t)$ at a certain time t was obtained by making a cumulative velocity distribution and fitting it with a cumulative Maxwell-Boltzmann (MB) distribution function. An example of such an cumulative distribution, at $\omega_m t = 10$, is shown in figure 3.2. The red bars display the number of particles with a velocity component in the $x-$direction smaller than v_x/c. The solid black line is the cumulative MB fit function defined as:

$$\int_{-\infty}^{v_x'} \exp\left(-\frac{m_e v_x^2}{2k_b T_e(t)}\right) \mathrm{d}v_x = \sqrt{\frac{\pi k_b T_e(t)}{2m_e}} \left[1 + \mathrm{erf}\left(\sqrt{\frac{m_e}{2k_b T_e(t)}} v_x'\right)\right] \tag{3.8}$$

with the error function defined as:

$$\mathrm{erf}(x) = \frac{2}{\sqrt{\pi}} \int_0^x \exp\left(-t^2\right) \mathrm{d}t$$

where the electron temperature $T_e(t)$ is used as the fitting parameter. The cumulative MB fit agrees well with the GPT data and the fitting parameter T_e, required to obtain the black solid line, is $T_e(10/\omega_m) = 1.5$ K.

In figure 3.3 the increase in the inverse coupling parameter is shown as a function of time $\omega_m t$. The red line is obtained by using the temperature $T_e(t)$ from the MB fit. The black points in figure (3.3) are obtained by using the average kinetic energy as a measure for the thermal energy $\frac{3}{2} k_b T_e \equiv \frac{1}{2} m_e \langle v_e^2 \rangle$. In thermal equilibrium these two identities should be equal [18]. The two functions agree very well for $\omega_m t > 1$ suggesting that there is indeed a local thermal equilibrium in the electron distribution for $\omega_m t > 1$. For $\omega_m t < 1$ there is a significant difference between the red line and the black point,

suggesting that the electron distribution is not in thermal equilibrium.

The advantage of the MB-fit is the suppression of large fluctuation compared to the method of the average kinetic energy on the longer time scales $\omega_m t > 1$, as can be seen in figure 3.3. The influence of a few very fast electrons can cause the average kinetic energy $\langle U_{kin} \rangle$ to obtain a peaked value, while those few outer electrons do not significantly change the shape of the MB fitting function.

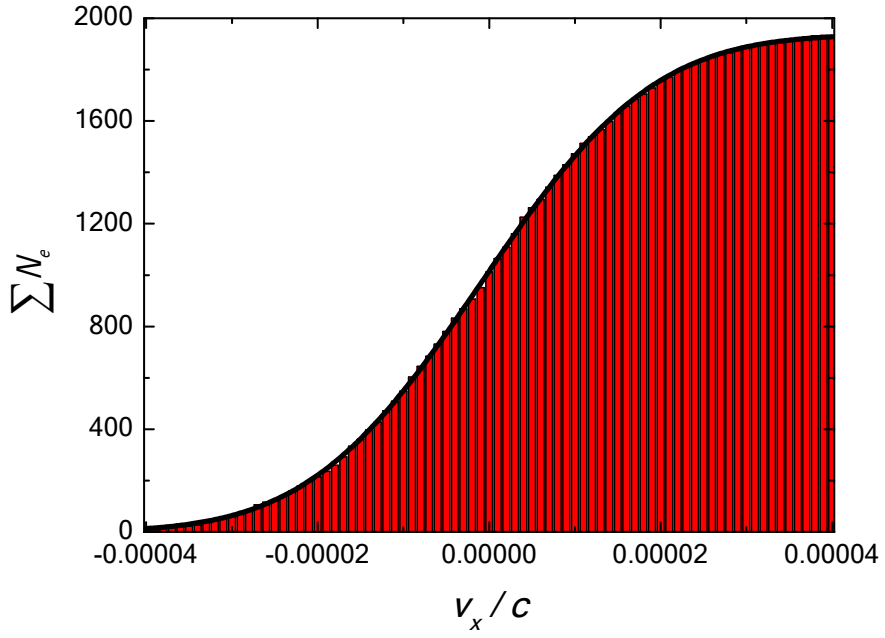

Figure 3.2: *Fit (solid line) with Boltzmann distribution (red bars) for the x-component of the velocity at $\omega_m t = 10$.*

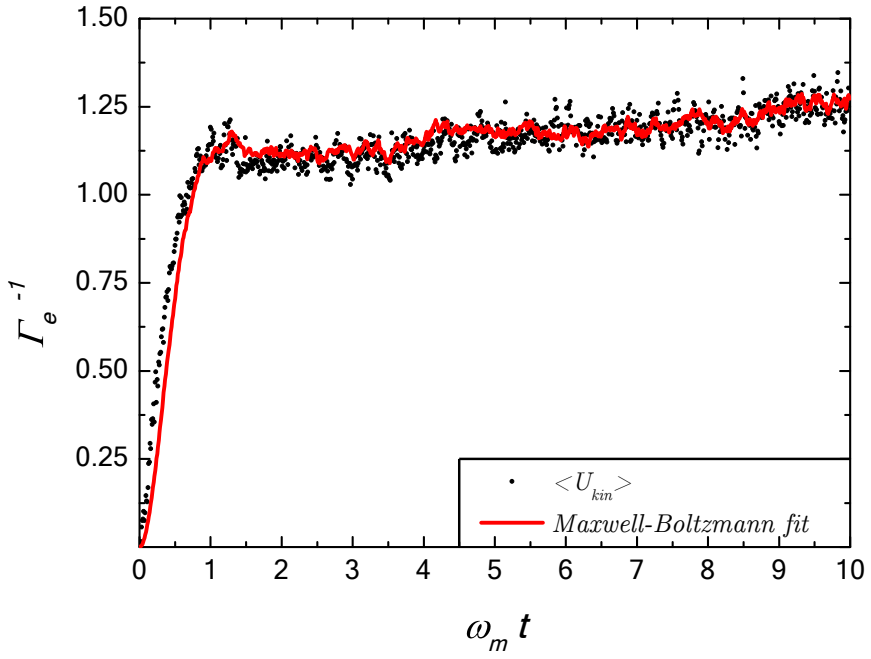

Figure 3.3: *Inverse coupling parameter Γ_e^{-1} determined via a Maxwell-Boltzmann fit (red line) and via the average kinetic energy (black points).*

In the initial time $\omega_m t \lesssim 1$ a rapid initial heating is clearly visible, corresponding to the disorder-induced heating phase. The time scale of this phase is approximately $t \approx \omega_m^{-1}$, confirming our expectations from equation (3.7). Furthermore, the coupling parameter rapidly increases to a value approximately equal to the predicted value $\Gamma_e^{-1} = 1$. This result is also in correspondence with previous simulations of Kuzmin et al. [22], although they used a finite simulation box with reflective walls and a lower particle mass ratio of $m_e : m_i = 1 : 100$ to speed up the numerical calculations.

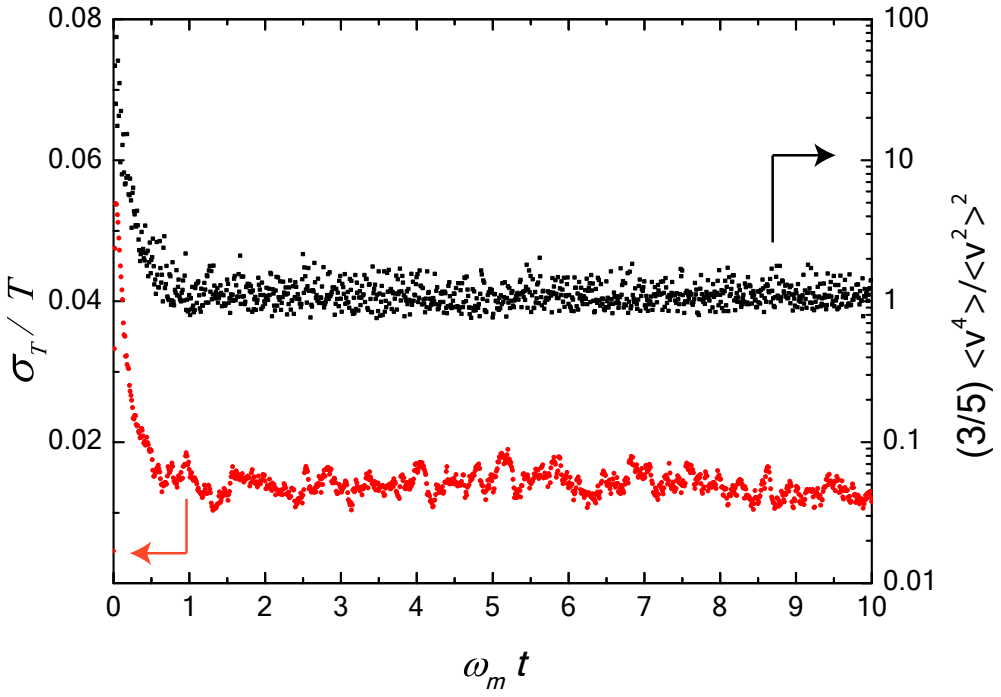

Figure 3.4: *Red: relative uncertainty of the temperature, obtained by a Maxwell-Boltzmann fitting function.*
Black: moment ratio of fourth and second moment distribution.

Figure 3.3 seems very convincing, but to check the assumption of thermal equilibrium more thoroughly two additional quantities are calculated.

The left axis of figure 3.4 shows the relative uncertainty in the electron temperature, indicating the applicability of the Maxwell-Boltzmann distribution. Apart from the initial disorder-induced heating phase the uncertainty in the temperature is smaller than 2%, which is considered small enough to assume the electrons have a local Maxwell-Boltzmann distribution [18].

On the right axis is another measure to determine resemblance of the simulated electron distribution to the Maxwell-Boltzmann function. Since all the electron velocities are known, the expression $(3/5)\left\langle v^4 \right\rangle / \left\langle v^2 \right\rangle^2$ can be calculated for the simulated electrons

as a function of time. For a Maxwell-Boltzmann function $(3/5)\left\langle v^4\right\rangle / \left\langle v^2\right\rangle^2 = 1$, which is indeed quickly approached for $\omega_m t \gtrsim 1$. Again it is shown that the electrons approach a local thermodynamic equilibrium immediately after the disorder-induced phase, despite the presence of the ions still being in a completely disordered state.

In figure 3.5 the result is shown for five independent simulations, each with a different initial uniform random distribution. The differences in the microscopic order at $\omega_m t = 0$ appear to be irrelevant for the value of the coupling parameter in the disorder-induced heating phase. In the more slowly heating regime $1 < \omega_m t < 20$ the influence of the initial microscopic order is clearly visible since the five independent simulations do not overlap anymore. Some of the electrons in the initial distribution have a somewhat larger excess of potential energy leading to a higher the amount of unleashed thermal energy resulting in a higher value of the inverse coupling parameter at the end of the disorder-induced heating phase. Close inspection of the right image of figure 3.5 also shows that at the end of the disorder-induced phase, $0.8 < \omega_m t < 1.2$ the coupling parameter slightly overshoots its 'equilibrium value' before settling to it.

This could be caused by the motion of each electron in its local potential. As an electron approaches the minimum of the potential, expected at a distance equal to a_0 it will not suddenly stop at the bottom, but it will overshoot and climb up the potential hill again. Therefore a certain harmonic motion is expected to persist for some time, as kinetic and potential energy are exchanged. This suggest an kinetic energy oscillation ($\sim \Gamma_e^{-1}$) at a frequency $2\omega_m$. These oscillations were also experimentally observed for *ionic* disorder-induced heating [21], but the fluctuations in figure 3.5 are too noisy to extract a $2\omega_m$ harmonic motion.

In figure 3.6 the average of the five simulations is taken, which reduces the noise of the aforementioned long-term oscillations. After the fast increase of the inverse coupling parameter during the disorder-induced phase the coupling parameter, a slower but significant heating can be observed. This heating is assumed to be caused by three-body recombinations, which will be the topic of the next section.

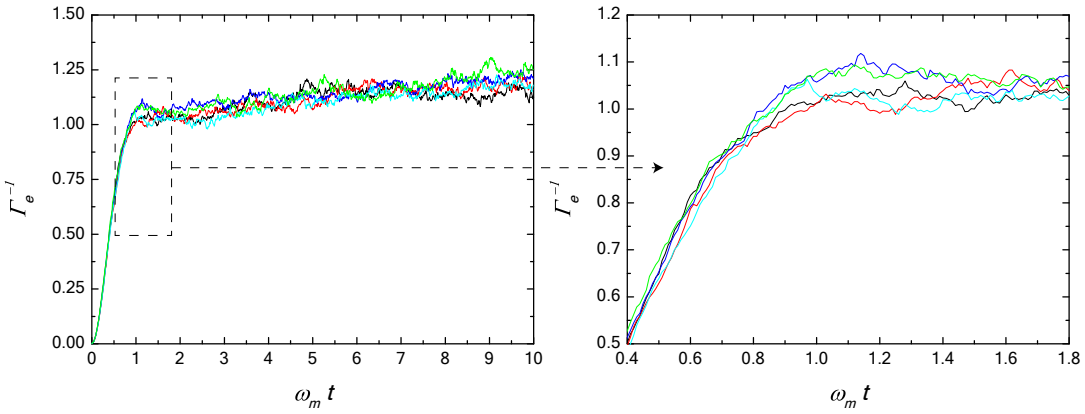

Figure 3.5: *Five different initial distributions.*

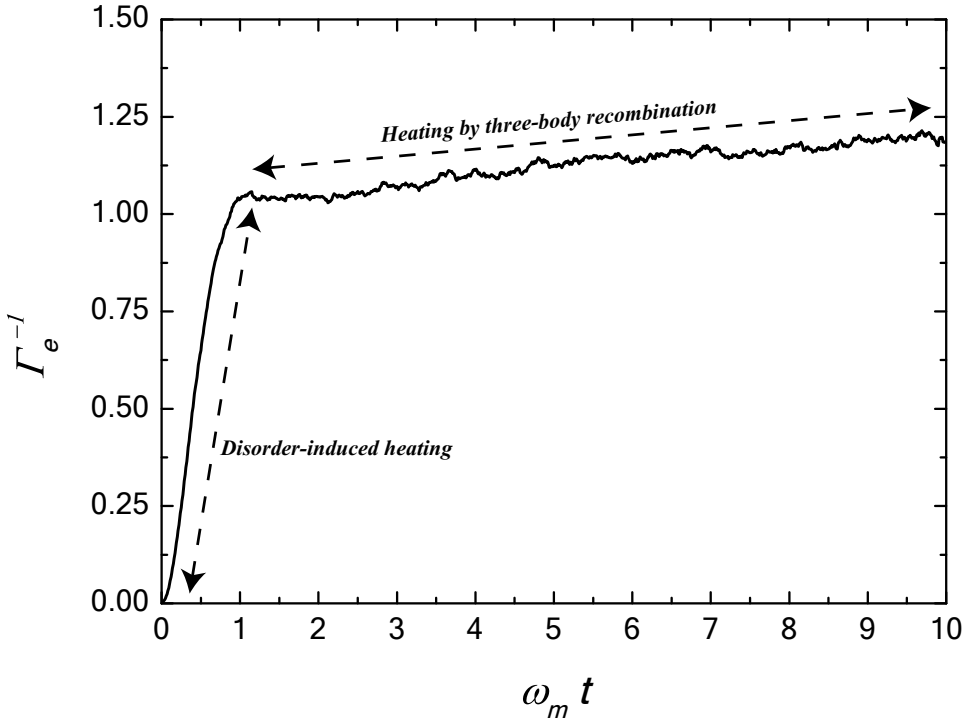

Figure 3.6: *Average distribution of the shown distribution in figure 3.5.*

3.2 Three-body recombination

The second mechanism responsible for the heating of an ultracold plasma is heating by three-body recombination (TBR), in which one electron recombines with an ion while a second electron takes up the excess of potential energy. Although this process is by nature a quantum-mechanical process, a classical treatment agrees well with both more elaborate theories and experiments [23]. Quantum-mechanically, the electrons will generally only recombine in highly-bound Rydberg states, which resemble classical Kepler orbits. Moreover the energy spacing of adjacent Rydberg levels becomes very narrow for $n \gg 1$ since the energy level spacing scales as $1/n^3$ for an energy level n, such that the highly-bound states form almost a continuum of possible orbits. Besides, the GPT software ignores the radiation fields of an electron which would force the electron to spiral inwards to the ion, making the GPT software able to mimic those highly-bound Rydberg states.

3.2.1 Classical model for three-body recombination

The original derivation by J.J. Thomson based on classical mechanics will be briefly discussed below [23]. The goal is to give basic insight into the temperature dependence and the magnitude of the TBR-rate. The Thomson theory was originally developed for

ion-ion recombination reactions but also applies for electron-ion recombinations:

$$e^- + R_b^+ + e^- \rightarrow R_b + e^- \tag{3.9}$$

with two electrons e^- and a R_b^+ ion. If one of the electrons and the R_b^+ ion approach each other their relative kinetic energy increases at the expense of potential energy.

The mathematics of this three-body problem is most convenient in the center-of-mass frame formed by the R_b^+ ion and one of the electrons. The total relative energy of the two particles, separated a distance r with relative speed v_{rel}, is:

$$U_{rel} = \frac{\mu v_{rel}^2}{2} - \frac{e^2}{4\pi\epsilon_0 r} \cong \frac{m_e v_{rel}^2}{2} - \frac{e^2}{4\pi\epsilon_0 r} \tag{3.10}$$

where $\mu = \frac{m_e m_i}{m_e + m_i} \cong m_e$ is the reduced mass of the the system of ion and electron, and $v_{rel} = |\vec{v_e} - \vec{v_i}|$ is the relative speed.

In the limit for a free electron ($r \rightarrow \infty$) the relative kinetic energy becomes $U_{rel} = \frac{1}{2} m_e v_{rel}^2 = \frac{3}{2} k_b T_e > 0$ in which the ion kinetic energy $\frac{3}{2} k_b T_i$ is assumed to be negligible. The total relative energy is conserved with $U_{rel} > 0$, so recombination cannot occur without interactions with other particles.

At some finite value r the relative kinetic energy $\frac{1}{2} m_e v_{rel}^2$ will exceed the value $\frac{3}{2} k_b T_e$. In that case the approaching electron could experience a thermalizing collision with a second electron, in which the relative kinetic energy reduces on average back to $\frac{3}{2} k_b T_e$. The new relative energy $U_{rel}^{'}$ then becomes:

$$U_{rel}^{'} = \frac{3}{2} k_b T_e - \frac{e^2}{4\pi\epsilon_0 r} \tag{3.11}$$

A bound state will be the result if the new energy $U_{rel}^{'} < 0$. The energy difference before and after the collision, $-\Delta U_{rel}$, is carried away by the second electron and equals $-\Delta U_{rel} = \frac{3}{2} k_b T_e - U_{rel}^{'} > \frac{3}{2} k_b T_e$. This leads to a condition for the separation distance r between an electron and an ion for which recombination can occur:

$$r < r_0 = \frac{e^2/4\pi\epsilon_0}{\frac{3}{2} k_b T_e} = \frac{2}{3} a_0 \Gamma_e(T) \cong 0.26 \cdot d_i \Gamma_e(T) \tag{3.12}$$

where r_0 is the so-called Thomson radius and a_0 is the Wigner-Seitz radius and $d_i = 2 \cdot \sqrt[3]{2} a_0$ is the average distance between two ions, which follows from equation (3.4). It follows from equation (3.12) that for $\Gamma_e \gtrsim 2$ the Thomson spheres from neighboring ions overlap (since $r_0 > d_i$ in that case) implying that the total available space for recombination for the electrons is larger than the total volume of the plasma. For a value of $\Gamma_e > 2$ the Thomson theory would evidently overestimate the amount of three-body recombinations.

Next an analytical expression will be derived for the recombination rate of the three-body collisions the plasma. The first requirement is an expression for the frequency $\bar{\nu_{ei}}$

at which one electron encounters the R_b^+ ion within a distance r_0:

$$\overline{\nu_{ei}} = n_{ion}\overline{v}_e\left(\pi r_0^2\right) \tag{3.13}$$

where n_{ion} is the ion number density and $\overline{v}_e = \sqrt{\frac{8k_bT_e}{\pi m_e}}$ is the average electron speed in the plasma.

The electron-ion recombination will lead to a decrease in the number of free electrons in the plasma. The change in the electron density n_e per unit time in the plasma is:

$$\frac{\mathrm{d}n_e}{\mathrm{d}t} = -n_e\overline{\nu_{ei}}s_1 = -\alpha_{ei}n_en_{ion} \tag{3.14}$$

in which s_1 is the probability that the incoming electron will make a thermalizing collision with a second electron and α_{ei} is the so-called recombination coefficient which follows from equation (3.13):

$$\alpha_{ei} = \overline{v}_e\pi r_0^2 s_1 \tag{3.15}$$

in which s_1 is the probability that the incoming electron will make a thermalizing collision with a second electron.

The probability s_1 that an electron makes an thermalizing collision is proportional to the probability of finding another electron in the Thomson sphere. The average number of electrons in the Thomson sphere is approximately equal to to $s_1 \sim n_e\frac{4}{3}\pi r_0^3$. So the recombination coefficient becomes:

$$\begin{aligned}\alpha_{ei} = \overline{v}_e\pi r_0^2 s_1 &\sim \overline{v}_e\pi r_0^2 n_e\frac{4}{3}\pi r_0^3 \\ &\sim \sqrt{\frac{8k_bT_e}{\pi m_e}}\pi^2 n_e r_0^5\end{aligned} \tag{3.16}$$

where the expression for the average thermal velocity was substituted $\overline{v}_e = \sqrt{\frac{8k_bT_e}{\pi m_e}}$. Substitution of equation (3.12) for r_0 results in:

$$\alpha_{ei} \sim C\frac{n_e}{T_e^{9/2}} \tag{3.17}$$

where the constant $C = \frac{4}{3}\pi^2\sqrt{8k_b/\pi m_e}\left(\frac{e^2}{4\pi\epsilon_0 k_b}\right)^5 \approx 1\cdot 10^{-19}$. Not every electron-electron encounter in the Thomson sphere will cause a three-body recombination to occur, so the value of the constant C has to be modified. The result from the traditional Thomson theory α_{Th} is given in appendix A.1 which results in a similar expression to equation (3.17) but with a pre-factor $C_{th} = 1.09\cdot 10^{-20}$.

Below the derived recombination coefficient of a more rigorous derivation by Hinnov et al. will be used [24, 25]. The Hinnov derivation also takes into account the occurrence

of re-ionizations; the collision of an electron with another bound electron-ion pair that ionizes the bound electron. The recombination coefficient becomes:

$$\alpha_{ei} = 1.09 \cdot 10^{-20} \frac{n_e}{T_e^{9/2}} \tag{3.18}$$

It is important to note that the theory by Hinnov et al. assumes the existence of a shielding Debye length as well, implying $\Gamma_e^{-1} > 1$; a concept for which the validity is questionable for ultracold plasmas. In section 3.1 it was revealed that after a time $\omega_m t \cong 1$ the inverse coupling parameter increased to a value $\Gamma_e^{-1} > 1$, due to the presence of disorder-induced heating. This could make the Thomson/Hinnov theory applicable for $\omega_m t > 1$.

Using the coefficient from equation (3.18) and equation (3.14), the total change in kinetic energy is:

$$\frac{\mathrm{d}U_{kin}}{\mathrm{d}t} = \frac{3}{2} k_b T_e \frac{\mathrm{d}n_e}{\mathrm{d}t} V = 1.09 \cdot 10^{-20} \frac{n_i n_e^2}{(k_b T_e)^{9/2}} \frac{N_i}{n_i} \frac{3}{2} k_b T_e \tag{3.19}$$

where $V = N_i/n_i$ is the volume in which the ions reside, which is equal to the initial volume of the plasma.

This equation can be also be written in a dimensionless form as the evolution of the inverse coupling parameter Γ_e^{-1}:

$$\frac{\mathrm{d}\Gamma_e^{-1}}{\mathrm{d}\tau} \cong 0.04 \cdot \frac{1}{\left(\Gamma_e^{-1}(\tau)\right)^{7/2}} \tag{3.20}$$

where $\tau = \omega_m t$.

It is also possible to calculate the amount of recombined electrons from the Thomson/Hinnov theory. Equation (3.14) can be written with the aid of equation (3.18) as:

$$\frac{\mathrm{d}N_e}{\mathrm{d}\tau} \cong -\frac{0.04}{\left(\Gamma_e^{-1}(\tau)\right)^{9/2}} N_e \tag{3.21}$$

where N_e is the number of electrons that have not yet recombined, the so-called free electrons.

3.2.2 Simulation results three-body recombination

First, it is necessary to ascertain that three-body recombinations actually occur in the GPT simulations. Therefore the binding energy U_b of electron-ion pairs was calculated. The binding of a certain electron is defined as the kinetic energy of the electron plus the potential energy of the electron in the field of the nearest ion:

$$U_b = \frac{1}{2} m_e v_e^2 - \frac{e^2}{4\pi\varepsilon_0 \min\left(|\vec{r}_i - \vec{r}_e|\right)} \tag{3.22}$$

In the simulations the distances between one electron and all the other ions are calculated after which the minimal distance is selected. In principle, a bound state is defined as $U_b < 0$. However, many particles are interacting in the plasma, such that the binding energy U_b can fluctuate around zero. In practice, an electron is assumed to be in a bound state if its energy $U_b < 0$ for some time.

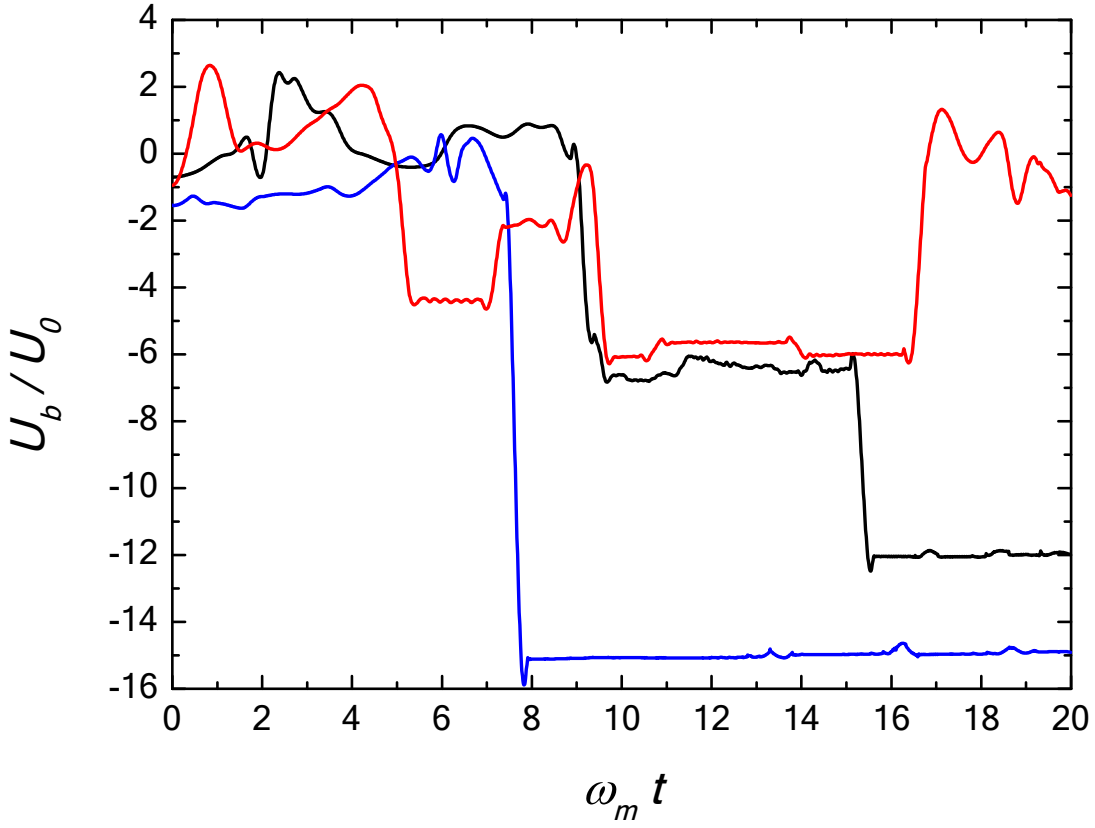

Figure 3.7: *Binding energy of three different electron-ion pairs in the plasma.*

In figure 3.7 the binding energy of three different electrons is shown as a function of time. The plateaus in the figure are the bound states, which arise immediately after a sudden drop in the binding energy between the electron and its nearest ion corresponding to the release of energy to a second electron.

The black line shows successive three-body recombinations into deeper bound states. In principle each electron could successively recombine into the deepest possible bound state which results from the definition of a Coulomb cut-off parameter $\epsilon = 1/100$ defined in chapter 2. This value of ϵ gives a well deepness of $U_b/U_0 = -100$, which directly followed from equation (2.3). The most tightly bound electrons in the simulations had a binding energy of $U_b/U_0 \approx -30$, so ϵ was sufficiently small to capture the dynamics of the most tightly bound electrons in the simulations.

The red line shows that it is also possible that an electron gets re-ionized. The

probability to re-ionize appeared to be related to deepness of the bound state. Tightly bound electrons were much less likely to be excited than electrons in higher levels. This is illustrated in the bar diagram in figure 3.8, which shows the fraction of re-ionized electrons as a function of binding energy U_b. Each bar contains the electrons with binding energies in the interval $\left(U_b/U_0 \pm \frac{1}{2}\right)$.

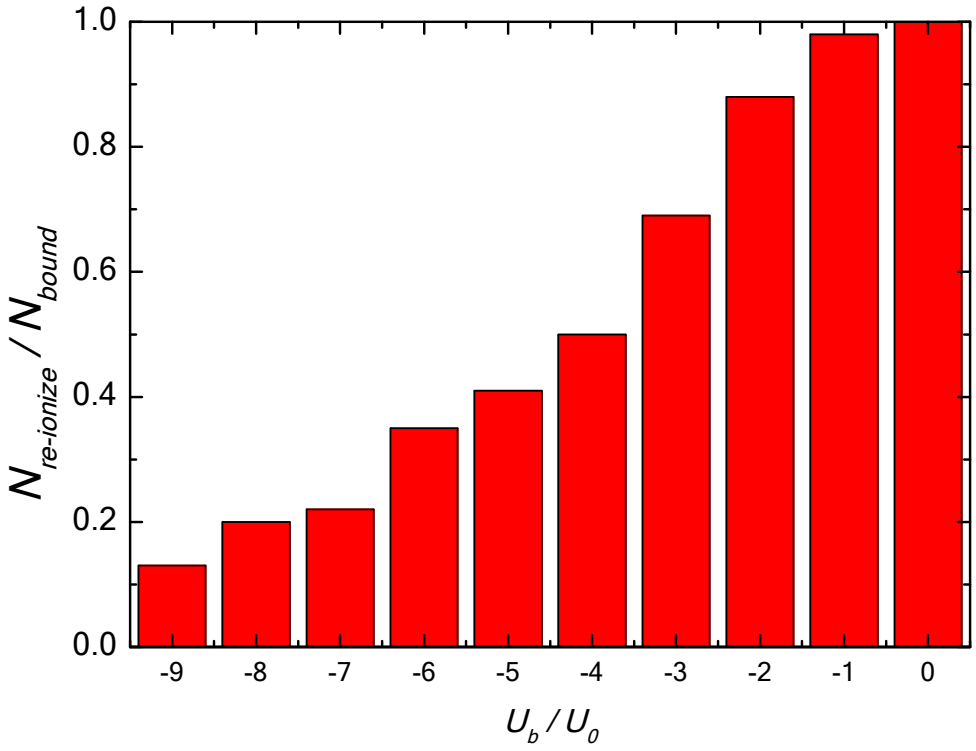

Figure 3.8: *Fraction of re-ionized electrons as a function of the binding energy.*

Mansbach and Keck defined the existence of a certain kinetic bottleneck level from results of Monte-Carlo calculations [26]. Electrons with a binding energy more negative than the kinetic bottleneck would cascade into deeper bound states while electrons occupying a level above the kinetic bottleneck would re-ionize. From figure 3.8 the kinetic bottleneck is assumed to be $U_b/U_0 \approx -4$, since more than half of the electrons occupying energy levels lower than this bottleneck will not re-ionize. This bottleneck is close to a previously determined value of the bottleneck of $U_b/U_0 = -3.8$ by molecular dynamics [27].

The amount of electrons with a binding energy below the kinetic bottleneck should increase to result in heating. Electrons in a level above the bottleneck will eventually re-ionize and therefore do not contribute to the heating by TBR on longer time scales. In figure 3.9 the fraction of electrons with an energy below the bottleneck is shown as a function of time. The slope in the graph is equal to $3.3 \cdot 10^{-3}$ indicating that each time step ω_m^{-1} the amount of electrons below the bottleneck increases with 0.33 % of the total number of electrons.

At the end of the simulation about 10 % of the electrons have a binding energy below the kinetic bottleneck and thus can be considered to be recombined.

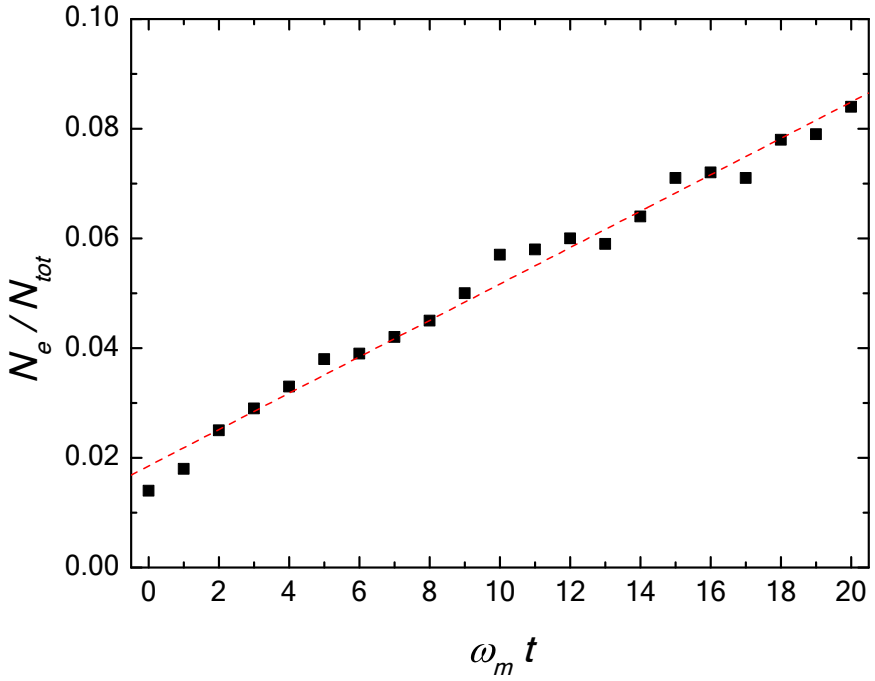

Figure 3.9: *Number of electrons N_e with a binding energy below the kinetic bottleneck.*

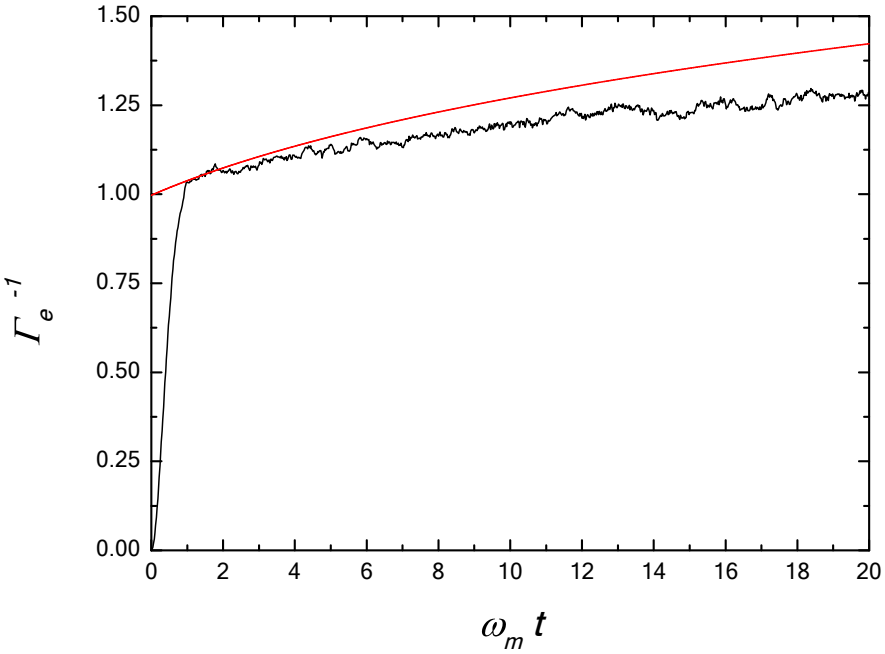

Figure 3.10: *Inverse coupling parameter for the electrons (black) and the analytical result for heating by three-body recombination (red).*

In figure 3.10 the analytically calculated TBR heating is shown as well as the simulated result.

The analytic result follows from equation (3.20). This equation requires one boundary condition to obtain a solution and this boundary condition is picked from the simulation results in figure 3.10: $\Gamma_e^{-1}(1) = 1.04$. It might seem obvious to chose the boundary value $\Gamma_e^{-1}(0) = 0$, but in the region $\Gamma_e^{-1} < 1$ the three-body theory is unreliable and therefore an initial point is chosen at which $\Gamma_e^{-1} \gtrapprox 1$.

The solution is:

$$\Gamma_e^{-1}(\tau) \cong 0.18 \cdot (2218 + 433\tau)^{2/9} \tag{3.23}$$

with the dimensionless parameter $\tau = \omega_m t$.

The analytical result clearly overestimates the amount of heating by three-body recombination. The average slope of the analytical function is $(1.90 \pm 0.03) \cdot 10^{-2}$ and the average slope of the plot for $1.5 < \omega_m t < 20$ equals $(1.20 \pm 0.04) \cdot 10^{-2}$.

The fraction of electrons that do not recombine in the interval $1 < \omega_m t < 20$ can be calculated by substituting the obtained expression for $\Gamma_e^{-1}(\tau)$ in equation (3.23) into equation (3.20) and integrating over the time $1 < \tau < 20$:

$$\frac{N_e(\tau = 20)}{N_e(\tau = 1)} = \exp\left[-\int_1^{20} \frac{0.04}{\left(\Gamma_e^{-1}(\tau)\right)^{9/2}} \mathrm{d}\tau\right] \approx 0.73 \tag{3.24}$$

This means that 73 % of the electrons which were not recombined at $\omega_m t = 1$ were

still free electrons at $\omega_m t = 20$. Simulations results indicated that just 1.8 % of the electrons had a binding energy below the kinetic bottleneck at $\omega_m t = 1$. Compensating for this initial point, the analytical theory predicts that 26 % of all the electrons should be recombined at $\omega_m t = 20$, in contrast to the 10 % that was obtained in the simulations.

3.3 Conclusions

In this chapter the heating of the electrons in a plasma without any external fields was studied. Two different forms of electron heating mechanisms were identified: disorder-induced heating and three-body recombination.

The first of these mechanisms is directly the result of the uncorrelated way in which the particles are created by photo-ionization. The excess of potential energy in the initial disordered state is rapidly converted into thermal energy on a time scale of the inverse electron plasma frequency ω_m^{-1}, confirming theoretical expectations as well as earlier computational work [22]. Furthermore the inverse coupling parameter increased to the value $\Gamma_e^{-1} = 1$ at the end of the disorder-induced heating phase and the electron distribution evolved in a Maxwell-Boltzmann distribution implying local thermodynamic equilibrium. This might not be evident since the electrons are also interacting with the ions, which are still in a randomly ordered state.

In the computation model it was assumed that all the electrons and ions were created simultaneously at $t = 0$ with a temperature $T = 0$. In experimental situations the charged particles are created in a small range of time, which would result in a somewhat longer timescale for the disorder-induced phase.

However, the most important conclusion is that disorder-induced heating prevents the development of strong coupling between the electrons in an ultracold plasma contrary to earlier speculations [3].

The second and more slowly heating mechanism is three-body recombination, in which an electron recombines with an ion in the presence of a second electron that takes up the excess of potential energy. The occurrence of a three-body recombination could be identified in the GPT simulations by a calculation of the interaction energy of an electron with its nearest ion. Both successive three-body combination into deeply bound states and re-ionization processes were observed. The probability of re-ionization depended strongly on the occupied level of the electron and a certain kinetic bottleneck could be identified which distinguishes recombined pairs from 'free' electrons. The kinetic bottleneck was estimated to be $U_b/U_0 \approx -4$, in correspondence to the value $U_b/U_0 = -3.8$ in previous work [27].

The amount of heating was calculated using the classical Thomson and Hinnov theories, although these theories are formally derived for plasma's with $\Gamma_e^{-1} \gg 1$. The calculated heating rate in the regime for which $\Gamma_e^{-1} \gtrsim 1$ was equal to the simulated heating rate within just a factor of 1.3.
It has been suggested that the phenomenon of three-body recombination could be used to

increase the electron coupling strength in the plasma after the disorder-induced phase. The idea is to deliberately add Rydberg atoms to the ultracold plasma, which could be re-ionized by the free electrons in the plasma. In the process of re-ionization the binding energy of the electron-ion pair increases and as a result the energy of the free electron would decrease. Numerical simulations confirmed the occurrence of a small but significant cooling of the electron temperature [28].

Collisionless absorption

In this chapter the influence of an external rf field $\vec{E} = E_0 \cos(\omega_d t + \phi_0)\vec{e_x}$ on the electron heating will be studied. The electron heating mechanisms in the previous chapter relied completely on the collisions between electrons an ions. In this chapter it will be shown that electrons can absorb energy from an applied rf field, even without the presence of individual electron and ion collisions. This heating mechanism is called collisionless absorption.

Besides the pair-interactions every electrons interacts with the potential of the plasma as a whole. The reason is that the plasma does not remain electrostatically neutral on a macroscopic scale, even not on the small timescales that are simulated. Due to their large kinetic energy and low inertia compared to the ions, electrons will escape from the plasma leading to positive charge build-up in the plasma. More electrons will continue to leave the plasma until the strength of the plasma's field becomes strong enough to bind the remaining electrons to the plasma. A quasi-equilibrium is formed between trapped electrons and the so-called self-consistent electrostatic plasma potential.

This is illustrated in figure 4.1, in which a cross section of the plasma potential is shown at 5 different times. This simulated result was obtained by initializing a uniform plasma with radius R_b and an initial electron temperature of $T_e = 70$ K and ion temperature $T_i = 0$ K. At $\omega_m t = 0$ the plasma is on average electrically neutral, but in the initial range $0 < \omega_m t < 2$ a quick charge build-up is visible. In the range $10 < \omega_m t < 20$ the plasma potential evolves very slowly compared to the initial range and the plasma potential can be considered in quasi-equilibrium.

In the absence of pair-interactions every electron will follow a bounded (if electron energy $E_e < |U_{pot}(r = 0)|$) or unbounded trajectory (if $E_e > |U_{pot}(r = 0)|$) in the potential well of figure 4.1. The origin of the collisionless absorption is the disturbance of an oscillating rf field on the 'plasma trajectory' of the electrons. The oscillating external rf field $E_0 \cos(\omega_d t + \phi_0)$ induces an internal polarization field in the plasma which disturbs the plasma trajectories.

The effect of collisionless absorption has been measured in experiments and computer simulations in the context of high-power-laser interaction with atomic an metallic clusters and many theoretical papers have been written about it [29, 30, 31, 32]. Various effects have been made responsible for the collisionless heating: $\vec{j} \times B$ heating (an overview can be found in [33]). This lead D. Bauer and P. Mulser to the conclusion that "(Too) many collisionless absorption mechanisms have been proposed which are not well separated from each other "[33] and that "collisionless absorption is well confirmed by experiments and simulations but not well understood " [30].

In this chapter collisionless absorption is defined as the absorbed energy due to an externally applied electric field. This will lead to energy gain or loss of the electrons. The

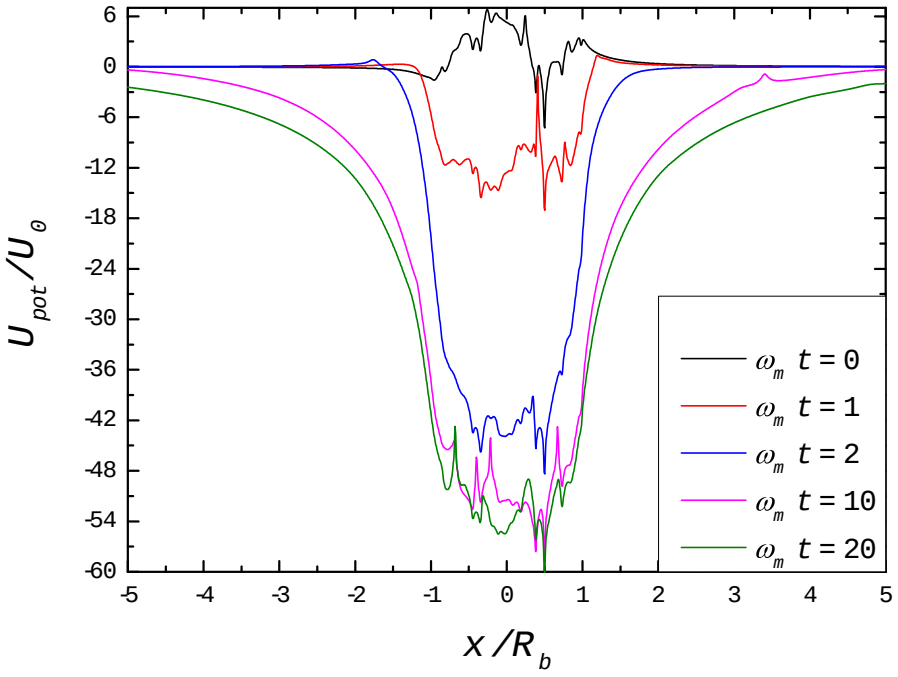

Figure 4.1: *Cross-section of the plasma potential at 5 different times, in which R_b is the initial plasma radius.*

goal is to elucidate the principles of collisionless absorption, by classical and quantum-mechanical theory as well as simulations.

In section 4.1 the internal electric field induced by the oscillating rf field will be calculated; the internal field that is responsible for the disturbance of the plasma trajectories.

As a first step, in section 4.2, the energy absorption of just one electron will be calculated in the conceptually most simple potential: the one-dimensional harmonic potential. The harmonic potential has only one resonant frequency and likewise the 'plasma trajectories'. A comparison will be made between a classical and quantum-mechanical derivation of the energy absorption.

The collisionless energy absorption will be simulated for a more realistic potential in section 4.3: the three-dimensional error-potential which has the largest resemblance to the plasma potential in figure 4.1.

4.1 The internal electric field

The first step to calculate the amount of collisionless absorption is to find the electric field inside the plasma.

A so-called jellium model will be used which describes the ultracold plasma by two charged rigid spheres with uniform charge density which interact with each other: a spherical electron cloud and an ion cloud. Consider a average shift $\zeta(t)$ of the electron cloud in the x-direction: $x \to x' - \zeta$. If the displacement ζ is on the order of the radius of the plasma R_b a large part of the electron cloud will be bulging out of the original plasma sphere and the repulsive electron-electron interactions becomes important. This would lead to a space-charge explosion of the electron cloud and the assumption of rigid electron and ion clouds would not be justified anymore. Therefore, the shift ζ considered is small enough such that the generated electric field will not alter the dynamics of the much heavier ions ($\zeta \ll R_b$)

The total potential V_{tot} can be expressed as the sum of two independent uniformly charged spheres; an electron sphere and an ion sphere with radius R_b. The potentials inside the uniformly charged spheres follow from Gauss's law:

$$V_e = -\frac{n_e e}{6\varepsilon_0}[3R_b^2 - ((x-\zeta)^2 + y^2 + z^2)] \tag{4.1a}$$

$$V_{ion} = \frac{n_i e}{6\varepsilon_0}[3R_b^2 - (x^2 + y^2 + z^2)] \tag{4.1b}$$

The restoring field inside the original plasma becomes:

$$\vec{E} = -\nabla\left(V_e + V_{ion}\right) = -\nabla\left(\zeta[\zeta - 2x]\right) = \frac{n_e e}{3\varepsilon_0}\zeta\vec{e_x} \tag{4.2}$$

where the assumption was made that $n_e \approx n_i$. A simple linear restoring force $\vec{F_e}$ results from a small deviation of the center of mass of the electron cloud:

$$\vec{F_e}(\zeta) = -\frac{e^2 n_e}{3\varepsilon_0}\zeta = -m_e\omega_m^2\zeta\vec{e_x}$$

with the definition of the Mie frequency:

$$\omega_m \equiv \frac{n_e e^2}{3m_e\varepsilon_0} \tag{4.3}$$

In more sophisticated models the restoring force becomes non-linear, and can be written as $-m_e\omega_m^2 G(\zeta)$ with the following expansion for $G(\zeta)$ [34]:

$$G(\zeta) = \zeta\left[1 + \sum_{k=1}^{\infty} b_k\left(\frac{\zeta}{R_b}\right)^{2k}\right] \tag{4.4}$$

where the linear restoring force is regained in the limit for small displacements $\zeta \ll R_b$.

In general, there will be some damping of the oscillation. This can be due to collisionless absorption, but also through collisions. This damping is interpreted as the conversion of energy from the motion of the electron cloud as a whole to the thermal energy of the individual particles in the cloud. Therefore, a general damping rate Γ is

introduced, just to see the effect on the internal electric field. This damping constant Γ includes the contribution from all absorption mechanisms.

Using the limit $\zeta << R_b$ the kinetics of $\zeta(t)$ in an rf field $E_0 \exp[i(\omega_d t + \phi_0)]\vec{e_x}$ follows from Newton's equations:

$$\frac{\mathrm{d}^2\zeta}{\mathrm{d}t^2} + 2\Gamma\frac{\mathrm{d}\zeta}{\mathrm{d}t} + \omega_m^2\zeta = -\frac{eE_0}{m_e}\cos(\omega_d t + \phi_0) \tag{4.5}$$

The particular solution of this equation is:

$$\zeta(t) = \mathrm{Re}\left\{\frac{eE_0}{m_e\left(\omega_d^2 - \omega_m^2 - 2i\Gamma\right)}\exp\left[-i(\omega_d t + \phi_0)\right]\right\} \tag{4.6}$$

The total electric field in the plasma $\vec{E}_{int}$ is the sum of the external rf field and the polarization field caused by the displacement of the electron cloud described in equation (4.2):

$$\vec{E}_{int}(t) = \frac{en_e}{3\epsilon_0}\zeta(t)\vec{e_x} + E_0\cos(\omega_d t + \phi_0)\vec{e_x} \equiv \mathrm{Re}\left\{\mathcal{E}_0\exp\left[-i(\omega_d t + \phi_0)\right]\right\}\vec{e_x} \tag{4.7}$$

where $\mathcal{E}_0$ is the complex Fourier component of the electric field inside the plasma.

The relation between the complex amplitude $\mathcal{E}_0$ and the external field amplitude E_0 can be found by substitution of ζ from equation (4.6) and the Mie-frequency ω_m:

$$\mathcal{E}_0 = \left(1 + \frac{\omega_m^2}{\omega^2 - \omega_m^2 - 2i\Gamma\omega}\right)E_0 \tag{4.8}$$

This equation can be written in terms of the dielectric constant for a spherical dielectric with an internal field given by [14, 13]:

$$\begin{aligned} &\mathcal{E}_0 = \frac{3}{2+\epsilon}E_0 \\ \text{with,}\quad &\\ &\epsilon = \epsilon' + i\epsilon'' \end{aligned} \tag{4.9}$$

Using equation (4.8) the dielectric constant can be written in terms of the Mie-frequency and the damping constant Γ:

$$\begin{aligned} \epsilon' &= 1 - \frac{3\omega_m^2}{\omega_d^2 + 4\Gamma^2} \\ \epsilon'' &= \frac{6\Gamma\omega_m^2}{\omega_d\left(\omega_d^2 + 4\Gamma^2\right)} \end{aligned} \tag{4.10}$$

Or in terms of the plasma frequency $\omega_p = \sqrt{3}\omega_m$:

$$\epsilon' = 1 - \frac{\omega_p^2}{\omega_d^2 + 4\Gamma^2}$$
$$\epsilon'' = \frac{2\Gamma\omega_p^2}{\omega_d\left(\omega_d^2 + 4\Gamma^2\right)} \tag{4.11}$$

In the absence of damping $\Gamma = 0$ this equation reduces to the familiar result $\epsilon = 1 - \frac{\omega_p^2}{\omega_d^2}$.

The main result of this section is equation (4.7); the internal field inside the plasma as a function of applied field frequency. In the next section the motion of an electron in the electron cloud will be studied.

4.2 Absorption in the harmonic potential

In the introduction it was shown that part of the electrons evaporate off the plasma, resulting in net plasma potential. The electron cloud is assumed to be still homogeneously charged, but with a density slightly lower than the ion density. As a consequence, the plasma potential is a simple harmonic potential $U_{plasma}(r) = U_{har}(r) = \frac{1}{2}m_e\omega_0^2 r^2$ with ω_0 the resonance frequency. This electron cloud moves as a whole, but this effect was already taken into account in the previous section and resulted in a correction on the applied rf field. It can be expected that this assumed U_{plasma} will be distorted by the movement of the electron cloud as whole near the edges of the spherical plasma. Therefore the assumption of the harmonic potential $U_{har}(r)$ is only valid far enough away from the edges of the plasma.

The assumption made in the previous section, $n_e \approx n_i$, is still valid. The electron density is only slightly lower. The plasma potential is related to the missing fraction of the electrons, Δn_e by:

$$U_{plasma}(r) = \frac{1}{2}\frac{e^2\Delta n_e}{3\varepsilon_0}r^2 = \frac{1}{2}m_e\omega_0^2 r^2 \equiv U_{har}(r)$$
with, (4.12)
$$\omega_0^2 = \frac{e^2\Delta n_e}{3m_e\varepsilon_0} = \frac{\Delta n_e}{n_e}\omega_m^2$$

from which it is clear that the resonance frequency ω_0 is by definition lower than the Mie frequency ω_m, the resonance frequency of the electron cloud as a whole.

The amount of collisionless absorption can be calculated with classical models [29, 32], but some authors prefer a quantum-mechanical calculation [8, 31, 35] for potentials that are more complicated than the harmonic oscillator. In the quantum-mechanical method knowledge of the *unperturbed* trajectories is sufficient to calculate the absorption. It is not necessary to know the trajectories in the rf-driven potential in contrast to the classical calculations.

However, for the harmonic potential solutions can be found from both the classical method as well as the quantum-mechanical method. Therefore in the following two

subsections a comparison will be made between the classical derivation and the quantum-mechanical derivation of energy absorption of one electron.

4.2.1 Classical derivation

Effective absorption in rf-driven plasmas occurs only in the presence of dissipation or at resonances. Dissipation mechanisms are due to the collisions between the particles and will be treated in chapter 5. In this section dissipation mechanisms will be neglected. If the electrons would move freely and not in a certain plasma potential, then energy would be exchanged reversibly between the electrons and the external rf field. However in the presence of a plasma potential, that can have multiple resonance frequencies, irreversible absorption of rf field energy occurs at the resonances of the potential [31, 29, 30].

The harmonic potential has only one resonance frequency ω_0 and therefore irreversible energy absorption is expected at just one applied rf field frequency: $\omega_d = \omega_0$.

The equation of motion for an electron in the x-direction of the potential is:

$$\frac{\mathrm{d}^2x(t)}{\mathrm{d}t^2} + \omega_0^2 x(t) = -\frac{e}{m_e} E_{int} \cos\left(\omega_d t + \phi_0\right) \tag{4.13}$$

where E_{int} is the internal field amplitude from equation (4.8). A damping term $\sim \frac{\mathrm{d}x}{\mathrm{d}t}$ is not included since the focus in this chapter is on resonant absorption and not on dissipation mechanisms.

The general solution for an electron with initial position $x(0) = x_0$ and $\frac{\mathrm{d}x}{\mathrm{d}t}|_{t=0} = v_0$ is:

$$\begin{aligned} x(t) =& \frac{v_0}{\omega_0} \sin\left(\omega_0 t\right) + x_0 \cos\left(\omega_0 t\right) - \frac{eE_{int}}{m_e \omega_0 (\omega_0^2 - \omega_d^2)} \Big[\omega_d \sin\left(\phi_0\right) \sin\left(\omega_0 t\right) \\ &+ \omega_0 \Big(\cos\left(\omega_d t + \phi_0\right) - \cos\left(\phi_0\right) \cos\left(\omega_0 t\right) \Big) \Big] \end{aligned} \tag{4.14}$$

where the first two terms correspond to the homogeneous solution of the equation.

The total energy of the electron in the plasma potential at a certain time, $U(t)$, is

given by:

$$
\begin{aligned}
U(t) &= U_{kin}(t) + U_{pot}(t) = \frac{1}{2} m_e \left(x'(t)\right)^2 + \frac{1}{2} m_e \omega_0^2 \left(x(t)\right)^2 \\
&= \frac{1}{2m_e \left(\omega^2 - \omega_0^2\right)^2} \Bigg(\left(\omega^2 - \omega_0^2\right) m_e \big[v_0 \sin\left(t\omega_0\right) + x_0 \omega_0 \cos\left(t\omega_0\right) \big] \\
&+ eE_{\text{int}} \Big[\omega \sin\left(\phi_0\right) \sin\left(t\omega_0\right) + \omega_0 \Big(\cos\left(t\omega + \phi_0\right) - \cos\left(\phi_0\right) \cos\left(t\omega_0\right) \Big) \Big] \Bigg)^2 \qquad (4.15) \\
&+ \Bigg(\left(\omega_d^2 - \omega_0^2\right) m_e \left(v_0 \cos\left(t\omega_0\right) - x_0 \omega_0 \sin\left(t\omega_0\right)\right) + eE_{\text{int}} \Big[- \omega \sin\left(t\omega + \phi_0\right) \\
&+ \omega \sin\left(\phi_0\right) \cos\left(t\omega_0\right) + \omega_0 \cos\left(\phi_0\right) \sin\left(t\omega_0\right) \Big] \Bigg)^2
\end{aligned}
$$

The significance of the initial phase ϕ_0 on the trajectory and the energy will be discussed later on, in the context of resonant absorption and in comparison with quantum-mechanical expressions. The *phase-averaged* energy is given by:

$$
U(t) = \frac{e^2 E_{int}^2}{2m_e \left(\omega_d^2 - \omega_0^2\right)^2} \left[\omega_d^2 + \omega_0^2 - \left(\omega_d^2 + \omega_0^2\right) \cos(\omega_d t) \cos\left(\omega_0 t\right) - 2\omega_0 \omega_d \sin(\omega_d t) \sin\left(\omega_0 t\right) \right] \qquad (4.16)
$$

In figure 4.2 the energy $U(t)$ is given as a function of time, scaled with the so-called ponderomotive energy U_p. The definition of U_p is:

$$
U_p = \frac{e^2 E_{int}^2}{4m_e \omega_d^2} \qquad (4.17)
$$

It is the time-averaged energy of a free electron oscillating in an rf field [36], and will also be used in chapter 5 as a convenient scaling parameter.

From this figure it becomes apparent that the energy of the rf field and the electron are exchanged reversibly. The amplitudes of the oscillation grow as ω_d approaches the resonance frequency. However after some time, when $|\omega_d - \omega_0|$ is exactly 2π, the gain goes to zero.

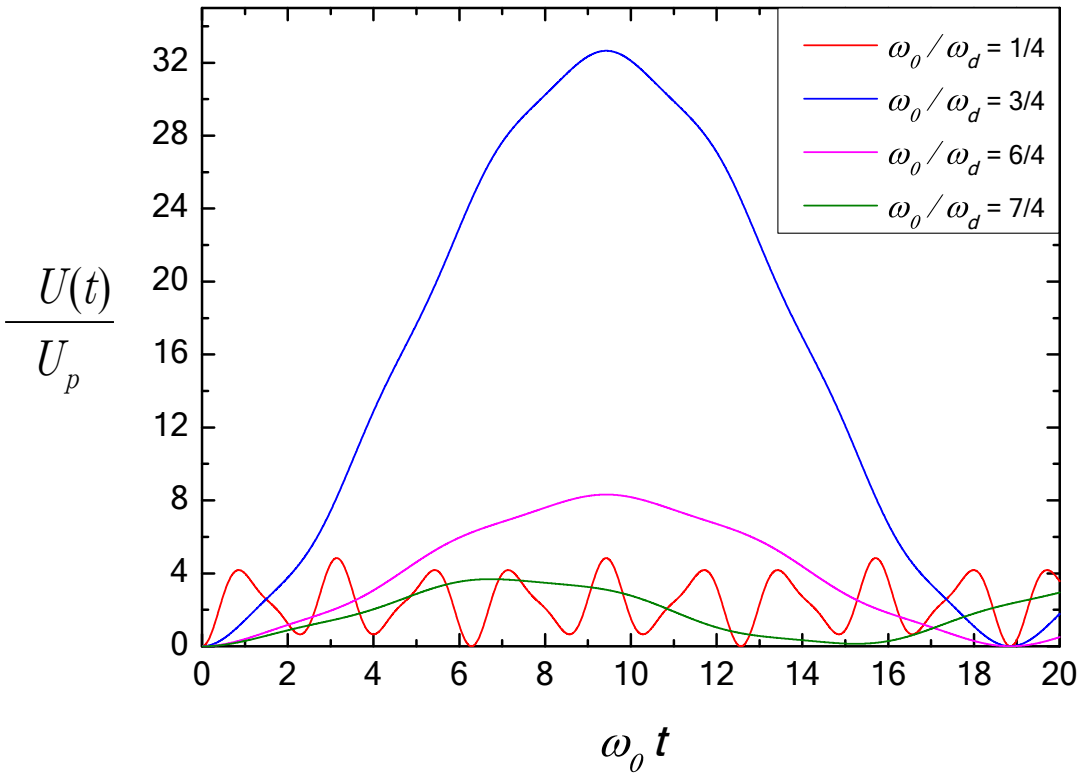

Figure 4.2: *Energy of the electron as a function of time for differen rf field frequencies* ω_d.

Only one driving field frequency is expected to lead to an *irreversible* energy absorption, that is exactly at the resonance frequency $\omega_d = \omega_0$. Therefore, first the trajectories exactly at resonance are calculated. The trajectory can be obtained from equation (4.14) by taking the limit $\omega_d \to \omega_0$. For particle with initial position $x(0) = 0$ this results in:

$$x(t) = \frac{v_0}{\omega_0} \sin(\omega_0 t) + \frac{eE_{int}}{2m_e\omega_0^2} \left[\sin(\phi_0) \sin(\omega_0 t) - \omega_0 t \sin(\omega_0 t + \phi_0)\right] \tag{4.18}$$

The trajectories are plotted for a particle with a small perturbing rf field ($eE_{int}/(m_e\omega_d^2) = 0.1v_0/\omega_0$) for the phases $\phi_0 = 0$ and $\phi_0 = \pi$ in figure 4.3. At resonance the amplitudes of the trajectory are increasing linearly from the point indicated by the blue arrow. This starting point for resonant absorption depends on the initial phase of the rf field. For the phase $\phi_0 = 0$ this resonant starts at $50\omega_0 t$, while for the phase $\phi_0 = \pi$ the resonant absorption has already begun at $t = 0$. The starting point would be at the non-physical negative time $-50\omega_0 t$.

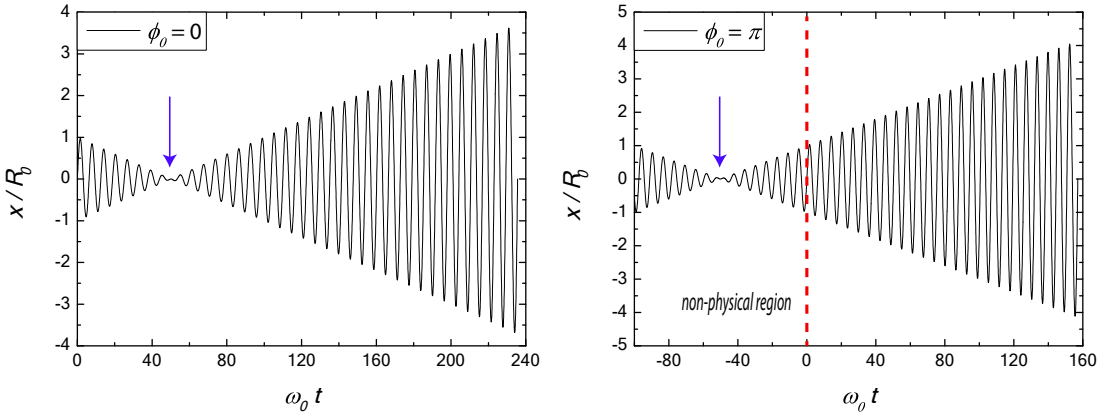

Figure 4.3: *Left: particle trajectory at resonance for* $\phi_0 = 0$.
Right: particle trajectory at resonance for $\phi_0 = \pi$.

The influence of the initial phase is also clearly visible in the energy of the particle. The energy of the particle, as calculated from equation (4.15) by taking the limit $\omega_d \to \omega_0$, is plotted for two different phases at the resonance frequency $\omega_d = \omega_0$ in figure 4.4. In the right image it is clear that the total energy of the particle decreases first for a phase $\phi_0 = 0$ while it increases immediately for a phase $\phi_0 = \pi$.

The black line corresponds to the energy averaged over all the possible initial phases ϕ_0. It can be found immediately from equation (4.15), by averaging over the initial phases and after that taking the limit $\omega_d \to \omega_0$. The result is:

$$U(t) = \frac{e^2 E_{int}^2}{8m_e}\left(t^2 + \frac{\sin^2(\omega_0 t)}{\omega_0^2}\right) + \frac{1}{2}m_e v_0^2 + \frac{1}{2}m_e\omega_0^2 x_0^2$$

or,

$$\Delta U(t) = U - U(0) = \frac{e^2 E_{int}^2}{8m_e}\left(t^2 + \frac{\sin^2(\omega_0 t)}{\omega_0^2}\right) = \frac{e^2 E_{int}^2}{8m_e}\left[1 + \mathrm{sinc}^2(\omega_0 t)\right] t^2 \tag{4.19}$$

where it follows from the limit $\mathrm{sinc}^2(x) \to 0$ for $x \gg 1$ that the energy increases quadratic in time for $\omega_0 t \gg 1$. The function $\mathrm{sinc}^2(\omega_0 t)$ is an oscillating function and can be regarded as the coherent part of the energy absorption at resonance, since that sinc^2 function oscillates at a frequency $2\omega_0$ between 0 and an amplitude that decreases with $1/t^2$.

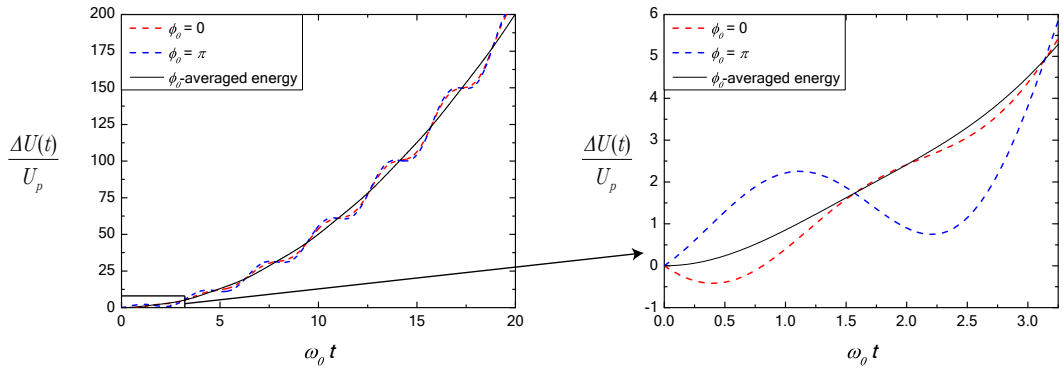

Figure 4.4: *Left: Energy gain ΔU of the particle for two different initial phases and the phase-average result.*
Right: Zoom-in of the left image.

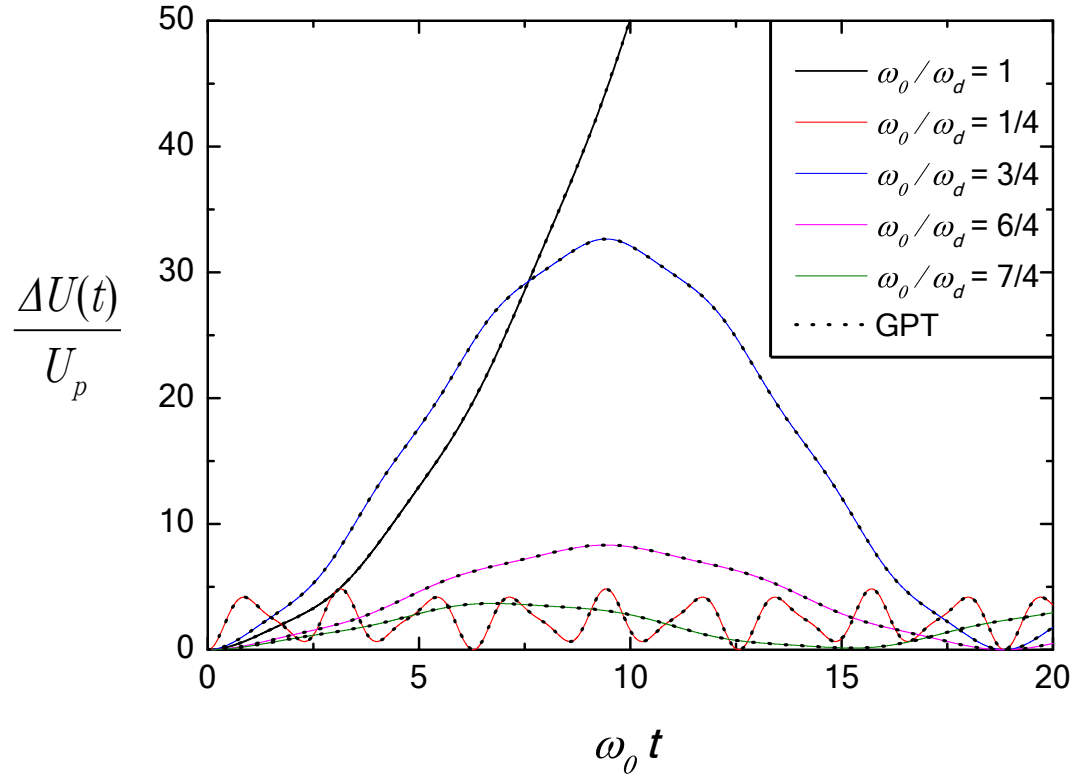

Figure 4.5: *Phase-averaged energy gain, simulations and theoretical curves, for different field amplitudes.*

The phase-averaged energy is plotted for different frequencies, including the resonance frequency, in figure 4.5. The dots are the simulations in the GPT software which are in agreement with the analytical curves. As expected, the GPT software is able to reproduce the classical physics of the electron in the harmonic potential.

4.2.2 Quantum-mechanical derivation

In this subsection a quantum-mechanical derivation is shown of equation (4.19). The well-known (first-order) perturbation theory will be used. Quantum mechanics can be more convenient to calculate the energy absorption in plasma potentials that are more complex than the harmonic potential.

First, the essential principles of first-order time-dependent perturbation theory will be explained briefly, following the treatment in quantum mechanics texts such as Sakurai and Shankar [37, 38]. The total Hamiltonian operator is $H = H^0 + H'(t)$, where $H'(t)$ is a small time-dependent perturbation and H^0 is the unperturbed Hamiltonian that does not explicitly depend on time. For the case of electron in an harmonic potential perturbed by an rf field, $H^0 = \frac{\vec{p}^2}{2m_e} + \frac{1}{2}m_e\omega_0^2 x^2$ and $H'(t) = -eE_{int}\cos(\omega_d t + \phi_0)\cdot x$; the perturbation of the rf field.

The first-order perturbation theory used in this section is essentially a semi-classical theory, since the operator $H'(t)$ consist of a classical electric field $E_{int}\cos(\omega_d t + \phi_0)$. A full quantum-mechanical treatment would require a quantized electric field consisting a discrete particles; photons.

However it appears sufficient to use a classical electric field. The transitions of the electrons that will be derived in this section occur in discrete steps of $\hbar\omega_d$, precisely the energy of a photon.

Initially, at $t = 0$, the electron is in one of the eigenstates $|i^0\rangle$ of the Hamiltonian H^0. The goal of first-order perturbation theory is to find the probability that at time t the electron is in (another) eigenstate $|k^0\rangle \neq |i^0\rangle$.

The eigenkets $|n^0\rangle$ of the Hamiltonian H^0 form a complete basis such that the state of the system $|\Psi(t)\rangle$ can be expanded as:

$$|\Psi(t)\rangle = \sum_n a_n(t)|n^0\rangle \tag{4.20}$$

The amplitudes $a_n(t)$ change with time because of H^0 and $H'(t)$. If the perturbation $H'(t)$ would be absent the amplitudes would be given by $a_n(t) = a_n(0)\exp\left(-iU_n^0 t/\hbar\right)$, where U_n^0 is the energy of the eigenstate n in the unperturbed Hamiltonian H^0. Motivated by this result the following ansatz is given for the state $|\Psi(t)\rangle$:

$$|\Psi(t)\rangle = \sum_n b_n(t)\exp\left(-iU_n^0 t/\hbar\right)|n^0\rangle \tag{4.21}$$

where the time dependence of $b_n(t)$ is solely due to the presence of $H'(t)$ since the

exponential absorbs any time dependence of the amplitudes due to H^0. Using the time-dependent Schrodinger equation $\left(i\hbar\frac{\partial}{\partial t} - \left[H^0 + H'(t)\right]\right)|\Psi(t)\rangle = 0$:

$$\sum_n \left[i\hbar\frac{\mathrm{d}b_n}{\mathrm{d}t} - H'(t)b_n(t)\right]\exp\left(-iU_n^0 t/\hbar\right)|n^0\rangle = 0 \tag{4.22}$$

Taking the inner-product with $\langle f^0|\exp\left(-iU_n^0 t/\hbar\right)$ and rearranging gives:

$$\frac{\mathrm{d}b_n(t)}{\mathrm{d}t} = -\frac{i}{\hbar}\sum_n \langle f^0|H'(t)|n^0\rangle\exp\left(i\omega_{fn}t\right)b_n(t) \tag{4.23}$$

where the frequency $\omega_{fn} = (U_f^0 - U_n^0)/\hbar$.

Consider the case that the system is in a state $|i^0\rangle$ at $t = 0$, thus $b_n(0) = \delta_{n,i}$ and the goal is to find $b_n(t)$. In the zeroth order $H'(t) = 0$ and the result is $\frac{\mathrm{d}b_n}{\mathrm{d}t} = 0$: no transitions occur. In the first-order approximation the zeroth order of $b_n(t)$ is used ($b_n = \delta_{n,i}$), since the perturbation $H'(t)$ is itself of first order. This gives the first-order equation:

$$\frac{\mathrm{d}b_f(t)}{\mathrm{d}t} = -\frac{i}{\hbar}\langle f^0|H'(t)|i^0\rangle\exp\left(i\omega_{fi}t\right) \tag{4.24}$$

Higher order perturbations can be found by making use of the Dyson series as explained in detail by Sakurai [37].

The probability to find the system at the state f at the time t is $P_{i\to f} = |b_f(t)|^2$. Since $b_f(0) = \delta_{i,f} = 0$ the equation for $b_f(t)$ becomes:

$$b_f(t) = -\frac{i}{\hbar}\int_0^t \langle f^0|H'(t')|i^0\rangle\exp\left(i\omega_{fi}t'\right)\mathrm{d}t' \tag{4.25}$$

Equation (4.25) will be applied to the rf driven electron in a one-dimensional harmonic potential. The unperturbed Hamiltonian is $H^0 = \frac{\vec{p}^2}{2m_e} + \frac{1}{2}m_e\omega_0^2 x^2$ and the perturbation is given by $H'(t) = -eE_{int}\cos\left(\omega_d t + \phi_0\right)\cdot x$ with E_{int} the internal field amplitude from equation (4.8). Substitution of $H'(t)$ results in:

$$\begin{aligned}
b_f(t) &= \frac{ieE_{int}}{\hbar}\langle f^0|x|i^0\rangle\int_0^t \mathrm{d}t'\cos\left(\omega_d t + \phi_0\right)\exp\left(i\omega_{fi}t\right) \\
&= \frac{ieE_{int}\langle f^0|x|i^0\rangle}{2\hbar}\int_0^t \left[\exp\left(i[\omega_{fi}+\omega_d]t' + i\phi_0\right) + \exp\left(i[\omega_{fi}-\omega_d]t' - i\phi_0\right)\right]\mathrm{d}t' \\
&= \frac{eE_{int}\langle f^0|x|i^0\rangle}{2\hbar}\left[\exp\left(i\phi_0\right)\frac{\left\{\exp\left(i[\omega_0+\omega_d]t\right)-1\right\}}{\omega_0+\omega_d} + \exp\left(-i\phi_0\right)\frac{\left\{\exp\left(i[\omega_0-\omega_d]t\right)-1\right\}}{\omega_0-\omega_d}\right]
\end{aligned} \tag{4.26}$$

where $\langle f^0|x|i^0\rangle$ is the expectation value of x in the harmonic potential, which is time-independent.

The focus will be on transitions close to the resonance frequency, $|\omega_0 - \omega_d| \ll 1$, since irreversible energy absorption is expected at the resonance frequency ω_0. Therefore the second term in the last equation of (4.26) will dominate. Dropping the first term gives:

$$\begin{aligned} b_f(t) &= \frac{eE_{int}\langle f^0|x|i^0\rangle}{2\hbar}\left[\frac{\exp\left(i[\omega_0-\omega_d]t\right)-1}{\omega_0-\omega_d}\right]\exp\left(-i\phi_0\right) \\ &= \frac{eE_{int}\langle f^0|x|i^0\rangle}{2\hbar}\frac{\exp\left(i[\omega_0-\omega_d]t/2\right)}{\omega_0-\omega_d}\left[\exp\left(i[\omega_0-\omega_d)t/2\right)-\exp\left(-i[\omega_0-\omega_d]t/2\right)\right]\exp\left(-i\phi_0\right) \\ &= \frac{eE_{int}\langle f^0|x|i^0\rangle}{\hbar}\frac{\sin\left([\omega_0-\omega_d]t/2\right)}{\omega_0-\omega_d}\exp\left(i[\omega_0-\omega_d]t/2\right)\cdot\exp\left(-i\phi_0\right) \end{aligned} \tag{4.27}$$

The transition probability $P_{i\to f} = |b_f(t)|^2$ then becomes:

$$\begin{aligned} P_{i\to f} = |b_f(t)|^2 &= \frac{e^2E_{int}^2}{\hbar^2}|\langle f^0|x|i^0\rangle|^2\frac{\sin^2\left([\omega_0-\omega_d]t/2\right)}{(\omega_0-\omega_d)^2} \\ &= \frac{e^2E_{int}^2}{4\hbar^2}|\langle f^0|x|i^0\rangle|^2\mathrm{sinc}^2([\omega_0-\omega_d]t/2)\cdot t^2 \end{aligned} \tag{4.28}$$

The dependence on the initial phase drops out automatically since the $\exp\left(-i\phi_0\right)$ term is multiplied with its conjugate and no averaging procedure is required. This is not an unexpected result. In a full quantum-mechanical treatment, the rf field is quantized too consisting of photons. Then the transitions $i \to f$ are interpreted as the absorption or emission of just one photon by the electron. A photon has no definite phase in quantum mechanics [39], but is an arbitrary number between 0 and 2π, so the initial phase of the rf field would be a questionable concept. Apparently, even in the semi-classical derivation the initial phase-dependence in the transitions disappears, in contrast to the classical derivation in subsection 4.2.1.

In the limit of resonance, $\omega_d \to \omega_0$, the sinc-function approaches $\mathrm{sinc}(0) \to 1$ and the transition probability becomes:

$$P_{i\to f} = \frac{e^2E_{int}^2|\langle f^0|x|i^0\rangle|^2}{4\hbar^2}t^2 \tag{4.29}$$

The matrix element $|\langle f^0|x|i^0\rangle|^2$ can be calculated if the states $|i^0\rangle$ are known explicitly. For an electron in an harmonic oscillator the different eigenstates $\Psi_n(x)$ are proportional to the Hermite polynomials $H_n(\xi)$ [38]:

$$\Psi_n(x) = \left(\frac{m_e\omega_0}{\pi\hbar 2^{2n}(n!)^2}\right)^{1/4}\exp\left(-\frac{m_e\omega_0}{2\hbar}x^2\right)H_n\left[\sqrt{\frac{m_e\omega_0}{\hbar}}x\right] \tag{4.30}$$

The Hermite polynomials preserve the orthogonality for the different eigenstates of the harmonic Hamiltonian. The following recursion relations apply to the Hermite polyno-

mials [38]:

$$\begin{aligned} 2yH_n(y) - 2nH_{n-1}(y) &= H_{n+1}(y) \\ \int_{-\infty}^{\infty} H_n(y)H_n'(y)\exp\left(-y^2\right)\mathrm{d}y &= \sqrt{\pi}2^n n!\delta_{n,n'} \end{aligned} \tag{4.31}$$

Considering an initial state $\Psi_n(x) \equiv |i^0\rangle$ and a final state $\Psi_{n'}(x) \equiv |f^0\rangle$ the matrix element $|\langle f^0|x|i^0\rangle|^2$ can be calculated. The details can be found in appendix A.2. The result is:

$$\langle f^0|x|i^0\rangle = \sqrt{\frac{\hbar}{2m_e\omega_0}}\left(\sqrt{i}\delta_{f,i-1} + \sqrt{i+1}\delta_{f,i+1}\right) \tag{4.32}$$

where the i's on the right-hand side correspond to the eigenvalue of the state $|i^0\rangle$. Equation (4.32) indicates that there are only two possible states to which the electron, initially in $|i^0\rangle$, can make a transition: the states $|i^0+1\rangle$ and $|i^0-1\rangle$. A transition to the state $|i^0+1\rangle$ corresponds to the absorption of a photon while the transition to $|i^0-1\rangle$ corresponds to stimulated emission.

Taking into account both the processes of absorption and emission of a photon with energy $\hbar\omega_d$, the change in energy of an electron is:

$$\begin{aligned} \Delta U(t) &= \hbar\omega_d\left[P_{i\to i+1} - P_{i\to i-1}\right] = \hbar\omega_d\frac{e^2E_{int}^2}{4\hbar^2}t^2\left(|\langle i^0+1|x|i^0\rangle|^2 - |\langle i^0-1|x|i^0\rangle|^2\right) \\ &= \hbar\omega_d\frac{e^2E_{int}^2}{4\hbar^2}t^2\left(\frac{\hbar}{2m_e\omega_0}[i+1] - \frac{\hbar}{2m_e\omega_0}i\right) \\ &= \frac{e^2E_{int}^2}{8m_e}t^2\frac{\omega_d}{\omega_0} \end{aligned} \tag{4.33}$$

At resonance, $\omega_0 = \omega_d$, this equation simply becomes:

$$\Delta U(t) = \frac{e^2E_{int}^2}{8m_e}t^2 \tag{4.34}$$

which corresponds to the classical result in equation (4.19) for $\omega_0 t \gg 1$. The only difference is that the coherent sinc^2 term from equation (4.19) is absent in the quantum-mechanical result.

The resonance results for both the quantum-mechanical equation (4.34) as well as the classical result from equation (4.19) are plotted in figure 4.6.

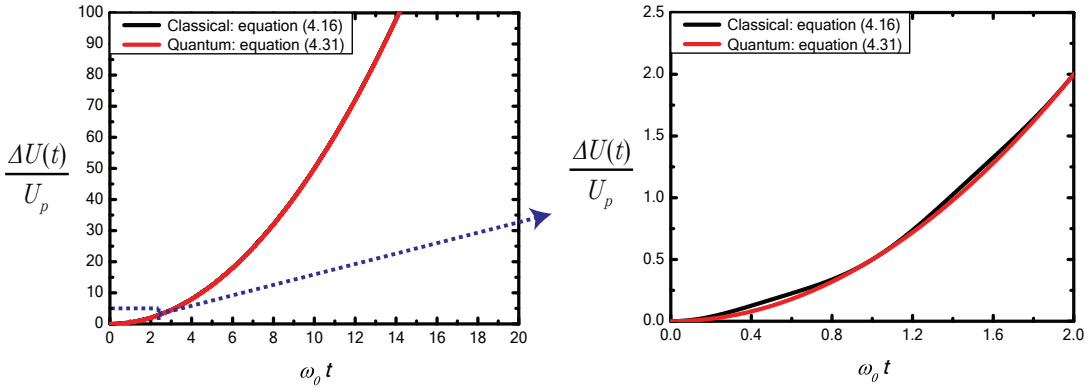

Figure 4.6: *Classical and quantum-mechanical result for the energy of an electron in an rf-driven harmonic potential.*

4.3 Collisionless absorption in plasma potential

In section 4.2 the energy absorption was calculated for a single particle in the one-dimensional harmonic potential, which has only one resonance frequency. Real plasma potentials on the other hand, will have multiple resonances, in other words can be written as a Fourier expansion with multiple harmonics with different frequencies. An example of a realistic plasma potential was shown in the introduction in figure 4.1. In the center $x < R_b$ the potential more a less resembles a harmonic potential, but in the region $x > 5R_b$ the potential is clearly anharmonic.

It is generally very difficult to find analytic solutions for the collisionless absorption in anharmonic potentials. Only a few specific plasma potentials allow exact solution in quantum-mechanical derivations; the classical derivations are even more complicated. Solvable potentials include the infinite well in 1D and 3D, the potential of a charged plane [40] and the 1D Duffing potential [8].

In this section a potential will be used that is often encountered in experimental situations: the 3-dimensional error potential. Closed analytical expression for the trajectories are unknown for this potential and therefore we have to rely on the GPT simulations. In this section first the trajectories of just one particle will be investigated in the 3D error potential, but after that also the energy increase in the (Maxwell-Boltzmann distributed) electron cloud as a whole will be studied.

The expression for the 3-dimensional error potential is [2]:

$$U(r) = U_{depth}\left[1 - \frac{\sqrt{\pi}\sigma}{2r}\mathrm{erf}\left(\frac{r}{\sigma}\right)\right] \tag{4.35}$$

where r is the distance to the center of the plasma, U_{depth} is the depth of the potential, σ is the rms-size of the ion cloud in which the electrons move and $\mathrm{erf}(x)$ denotes the

error function given by the equation:

$$\mathrm{erf}(x) \equiv \frac{2}{\sqrt{\pi}} \int_0^x e^{-t^2} \mathrm{d}t \tag{4.36}$$

For $r/\sigma \ll 1$ a Taylor expansion can be applied to equation (4.35) that results in:

$$U(r) = \frac{U_{depth}}{3\sigma^2} r^2 + O(r^4) \approx \frac{U_{depth}}{3\sigma^2} r^2 \tag{4.37}$$

If r/σ is sufficiently small, the fourth order and higher terms represented by $O(r^4)$ in the expansion can be neglected and a simple harmonic potential is the result with frequency:

$$\omega_0 = \sqrt{\frac{2U_{depth}}{3m_e\sigma^2}} \approx \sqrt{\frac{2k_bT_e}{3m_e\sigma^2}} \tag{4.38}$$

since U_{depth} is usually approximately equal to the thermal energy of the electrons [2]. Both the error potential (black solid line) and its limit $r/\sigma \ll 1$ (red dashed line) are illustrated in figure 4.7.

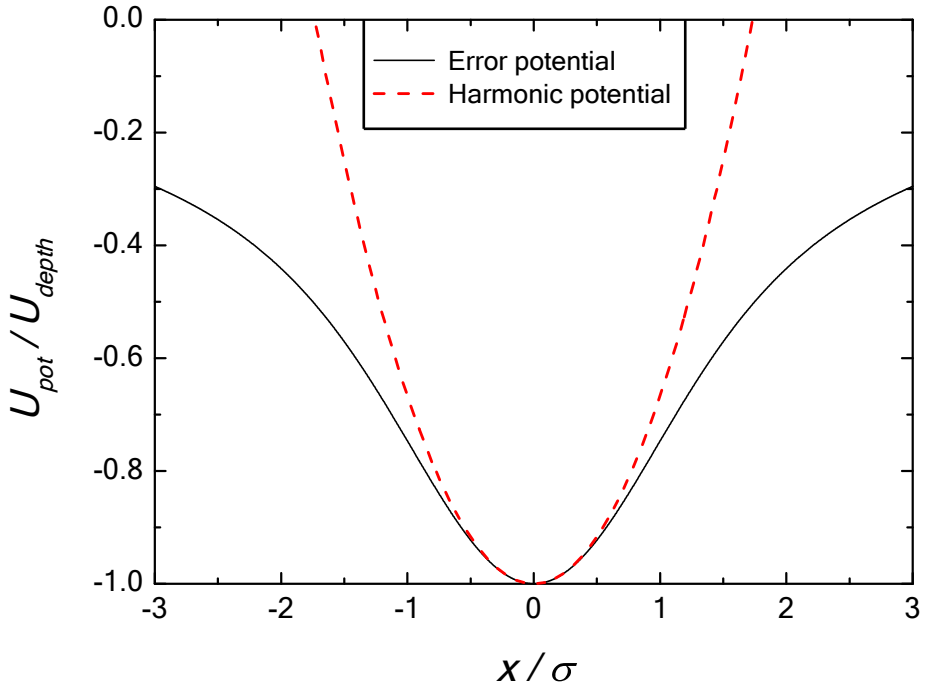

Figure 4.7: *Cross-section of the error potential in equation (4.35) and the harmonic potential of equation (4.38).*

The difference in the dynamics of an electron in the error potential arise due to the anharmonicity of the potential for $r/\sigma \gtrapprox 1/2$. This is illustrated in figure 4.8, where the trajectories of three particles with a different initial velocity v_0 but the same initial position $x_0 = 0$ are plotted as a function of time. The corresponding fourier spectra of the trajectories $x(t)$ can be found in figure 4.9, where the $|Y_k|$ is the absolute value of the Fourier amplitude from the Fourier expansion $x(t) = \sum_k Y_k \exp(i\omega_k t)$ [41]. The value of $|Y_k|$ on the vertical axis shows the contribution of a certain harmonic oscillation at frequency ω (scaled with ω_0 from equation (4.38)) to the trajectory in figure 4.8.

The trajectory of an electron initially at $x(0) = 0$ is plotted as a function of time for different values of the initial velocity v_0. For the initial velocity $v_0 = \sqrt{k_b T_e/5m_e}$ (blue line) the electron starts an oscillation with an amplitude of about $x/\sigma \approx 0.20$, so the electron is approximately moving in the harmonic region of the potential as can be checked in figure 4.7. The oscillation frequency Ω of this electron is approximately equal to the harmonic oscillator frequency of equation (4.38), as can be seen directly from the Fourier spectrum (blue line) in figure 4.9.

For an initial velocity $v_0 = \sqrt{9k_b T_e/m_e}$ (black line) the particles starts to oscillate with an amplitude $x/\sigma \approx 2.3$ and enters the anharmonic region of the error potential. The oscillation clearly differs from the harmonic oscillation of the black line. The shape of the red curve clearly differs from a simple sine function, especially around the top where the particle is at its turning point in the error potential. This could be expected, since the turning points are in the anharmonic region of the error potential ($x/\sigma \approx 2.3$). The trajectory can be represented by the sum of different harmonics, since the Fourier spectrum in figure 4.9 consists of more than one peak. The dominant oscillation frequency is the first harmonic at $\omega \approx 0.4\omega_0$, corresponding with the largest peak in the spectrum. Other harmonic contribution are at the oscillation frequencies $\omega \approx 1.25\omega_0$ and $\omega \approx 2.1\omega_0$.

The most important result from figure 4.8 is that the oscillation frequency of the electron in the error potential $\Omega(U)$ strongly depends on the trajectory of the particle and likewise on the total energy of the particle $\Omega \equiv \Omega(U)$, in this case $U = m_e v_0^2/2$.

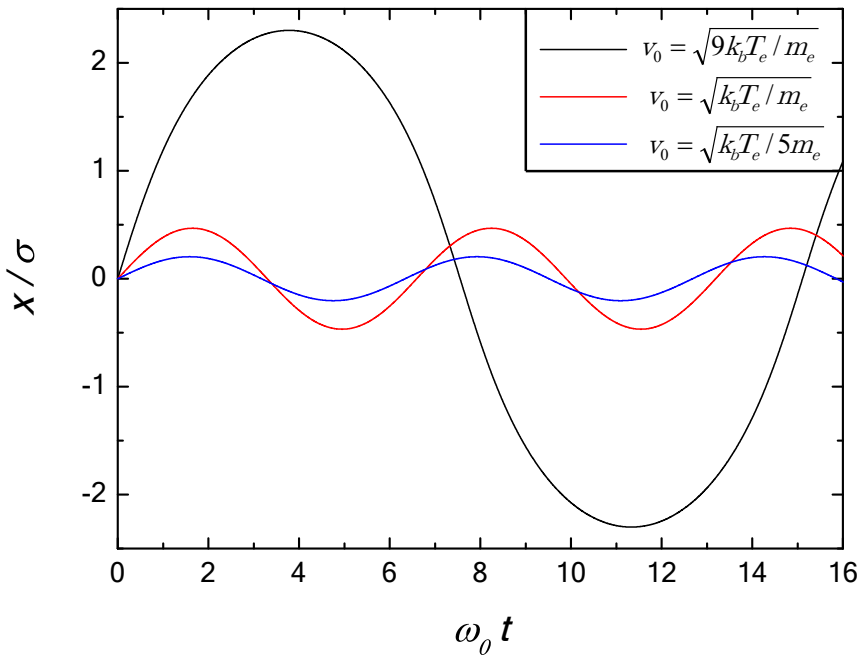

Figure 4.8: *Particle trajectory for an electron starting at* $x(0) = 0$ *for three different initial velocities* v_0.

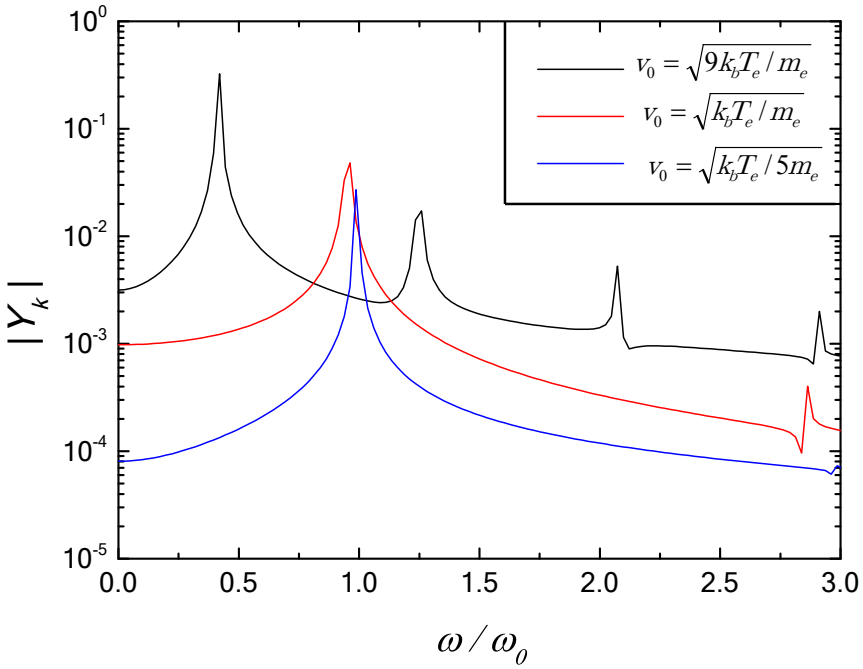

Figure 4.9: *Fourier spectra of the particle trajectories of figure 4.8.*

The dependence of the oscillation frequency on the energy $\Omega(U)$ has two important consequences, when introducing a disturbing rf field $E_{int}\cos(\omega_d t + \phi_0)$.

In the harmonic potential there is only one resonance frequency and irreversible energy absorption only occurs if the rf field frequency is exactly equal to the resonance frequency of the potential ($\omega_d = \omega_0$). If an rf field with frequency $\omega_d = 0.4\omega_0$ would be applied, then energy would be reversibly exchanged between the external field and the electrons. However, in an error potential some of the electrons in the electron cloud are oscillating at another oscillation frequency. A particle with $v_0 = \sqrt{9k_bT_e/m_e}$ for example is oscillating at a dominat frequency $\Omega(U) = 0.4\omega_0$, as shown by the black line in figure 4.8. This particle would be in resonance with an external rf field with frequency $\omega_d = 0.4\omega_0$.

The electron cloud in the plasma generally has a certain energy distribution, which could be a Boltzmann energy distribution. Therefore, there is also a distribution of different oscillation frequencies in the cloud and generally there are always electrons in the cloud that are resonantly excited by the rf field, even if $\omega_d \neq \omega_0$.

A second consequence of the energy dependence on the oscillation frequencies $\Omega(U)$ is that particles which are initially at resonance are automatically drifted away from resonance after a certain time when an external field $E_{int}\cos(\omega_d t + \phi_0)\vec{e_x}$ is applied. This principle is shown in figure 4.10. One particle was simulated with an initial velocity of $\vec{v_0} = \sqrt{k_bT_e/5,_e}\vec{e_x}$, resulting in an initial trajectory approximately harmonic as indicated by the blue line in figure 4.8. The rf field frequency was chosen equal to the harmonic frequency $\omega_d = \omega_0$, such that the electron was initially at resonance and the initial phase was chosen $\phi_0 = 0$.

The trajectory of the electron is shown in the right image of figure 4.10. It has only an x-component since the initial velocity of the electron was chosen in the polarization direction of the rf field. The red dashed line corresponds with the trajectory of an electron in an resonantly driven harmonic potential, previously illustrated in figure 4.3. Initially, the trajectories in the harmonic potential and the error potential are approximately the same, until the oscillation amplitude exceeds the value $x/\sigma \approx 0.4$ which is accomplished at $\omega_0 t \approx 36$. For $\omega_0 t > 36$ a phase difference develops indicating that the electron in the error potential is oscillating at a frequency slightly different from ω_0. The electron is not in resonance anymore and as a consequence the amplitude of the oscillation will start to decrease back to zero in the range $50 < \omega_0 t < 90$.

The drift out of resonance can also be seen in the right image of figure 4.10, where the energy of the electron is plotted as a function of time. During the time $\omega_0 t \lessapprox 36$ the energy increases quadratic in time as shown in the right image of figure 4.10, just as a particle in the harmonic potential shown by the red-dashed line. However for $\omega_0 t > 36$ the electron enters the non-harmonic parts of the error potential. As a consequence the particle is not on resonance anymore and the energy of the electron start to deviate from the energy in the harmonic potential. The electron is not in resonance anymore and therefore the energy will be exchanged reversible between and the particle and the field.

In figure 4.11 the trajectory and energy of an electron with initial velocity $\vec{v_0} = \sqrt{k_b T_e / m_e}\vec{e_x}$ are shown. The electron has a larger initial energy and therefore the electron moves into the anharmonic region $x/\sigma \approx 0.4$ of the potential during its first oscillation. A significant difference between the harmonic potential and error potential develops almost from the start of the oscillation.

Another difference with figure 4.10 is in the phase of the energy oscillations, despite the fact that the initial rf field phases are both zero.

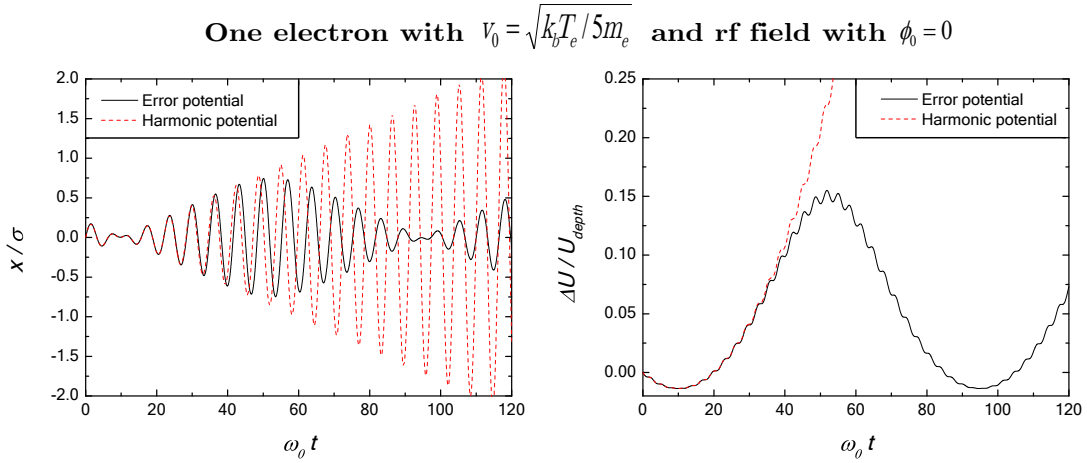

Figure 4.10: *Left: Trajectory in the x-direction, $|x(t)|/\sigma$, in two different potentials. Right: Energy gain, ΔU, of resonantly driven electron in two different potentials.*

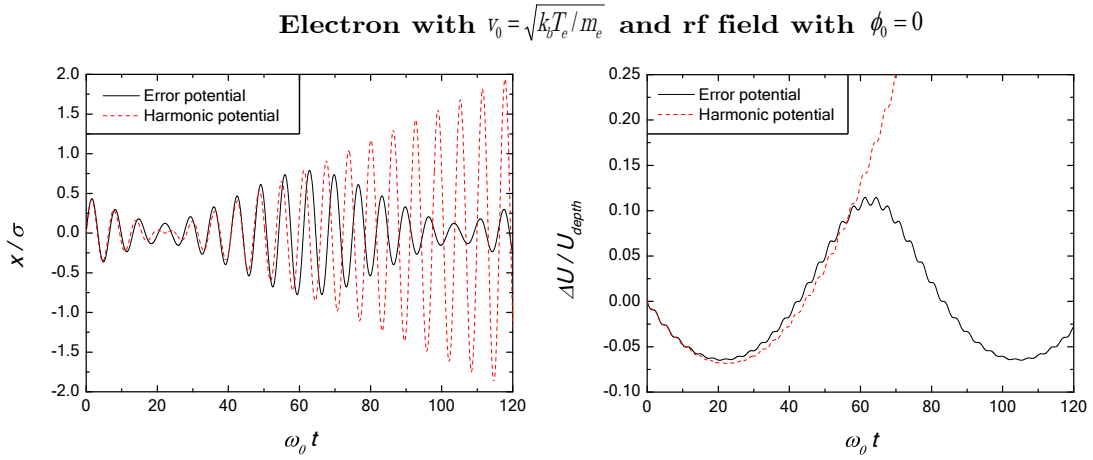

Figure 4.11: *Left: Trajectory in the x-direction, $|x(t)|/\sigma$, in two different potentials. Right: Energy gain ,ΔU of resonantly driven electron in two different potentials.*

The previous results of the energy absorption and trajectories were all just of an electron moving in a 3D error potential. Furthermore, the initial velocity was chosen in the polarization direction of the rf field resulting in an essentially 1D motion.

Now the energy absorption will be simulated for an electron cloud with Boltzmann energy distribution. All the particles are initialized at $\vec{r} = 0$ and a Maxwell-Boltzmann velocity distribution in all three directions is used, the space-charge forces between the electrons were turned-off since the focus is still on collisionless absorption. GPT is a classical simulation tool so simulations were performed for different initial rf field phases ϕ_0 as a way to average over the initial phase. The total energy of all the electrons in the plasma was calculated for different driving field frequencies.

A few results are shown in figure 4.12 where the total energy of the electron distribution is plotted as a function of time. Three different driving field frequencies were chosen, which are all close to the harmonic resonant frequency ω_0.

The largest amount of energy absorption could still be expected at the harmonic resonant frequency, because in the MB-function 68% of the electrons have a velocity smaller than the rms-size $\sqrt{k_b T_e / m_e}$. An initial velocity of $v_0 < \sqrt{k_b T_e / m_e}$ results in trajectories in the x-direction that initially almost harmonic motion as was shown in figure 4.8.

The dominant absorption at $\omega_d \approx \omega_0$ is confirmed by the simulations and shown in figure 4.12. Initially the energy of the red line increases until a time $\omega_0 t \approx 50$. At that time the oscillation amplitude of the center-of-mass of the electron cloud is about $x_{cm}(t)/\sigma \approx 0.5$. In the right image of figure 4.10 it was clear that for one electron an amplitude of $x(t)/\sigma \approx 0.4$ was already large enough to drive the particle out of resonance. Analogously, the majority of the particles in the electron cloud is expected to be driven out of resonance. This behavior is also found for $\omega_0 t > 50$ in figure 4.12, but this time the energy does not decrease back to zero, as was found for one electron

in figure 4.10. Every electron in the Boltzmann distributed cloud exchanges its energy reversibly with the external field, but the time at which all the energy gain is zero again strongly depends on the initial velocity of the electron. The individual electron energy oscillations are at slightly different phases and the average result is a net absorption.

A second important result from figure 4.12 is that there is also a significant net energy absorption for driving frequencies that differ significantly from the harmonic frequency ω_0. This is also due to the presence of a Boltzmann energy distribution, such that different electrons can have a different oscillation frequency $\Omega(U)$.

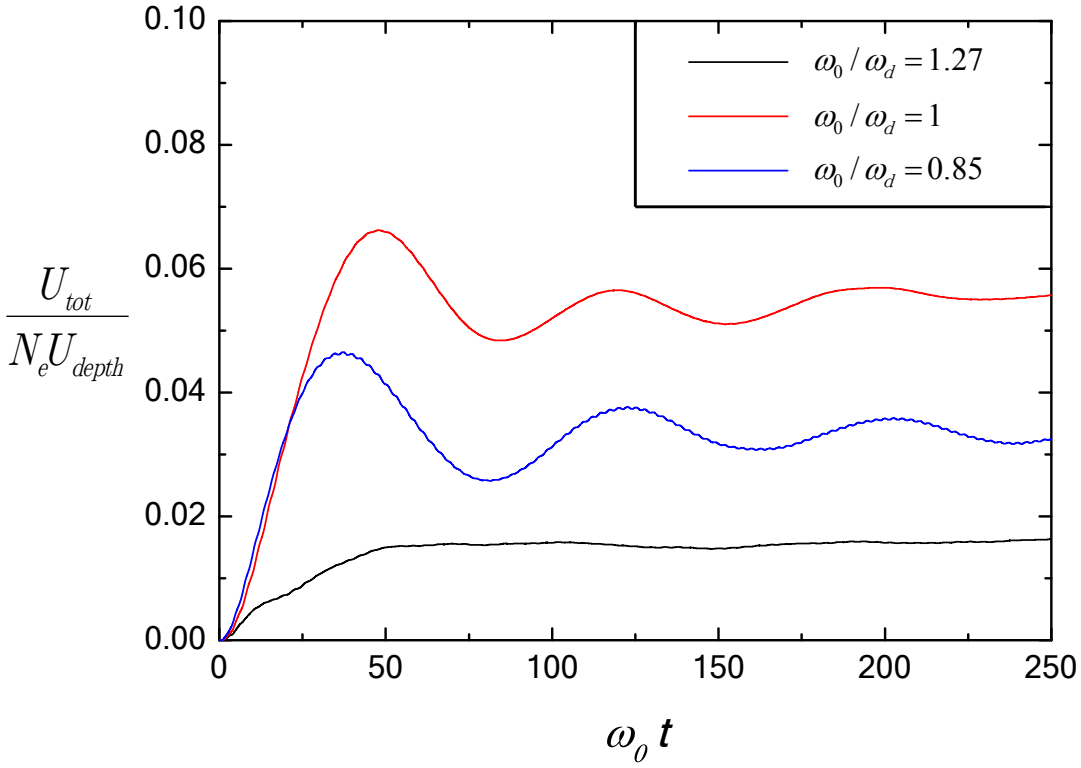

Figure 4.12: *Energy of the electron cloud with a MB-distribution for three different driving frequencies.*

For driving frequencies far from ω_0 the energy absorption is negligible. To illustrate this the final energy gain $\Delta U_{tot,f}$ of the electron cloud (the energy gain at the end of the simulation) was compared for different driving field frequencies. The result is shown in figure 4.13.

Figure 4.13 shows that net energy absorption is most significant for a Boltzmann-distributed electron cloud driven at the harmonic frequency ω_0. In the region $1.0 < \omega_0/\omega_0 < 1.5$ there is still a significant amount of absorption, but for $\omega_0/\omega_d < 1$ the amount of absorbed energy falls off dramatically as a function of increasing field fre-

quency. This behavior was also found for the infinite well potential [35, 40] as well as the 1D Duffing potential [8].

If one wants to prevent collisionless absorption it is therefore best to use a field frequency ω_d significantly larger than the harmonic frequency ω_0.

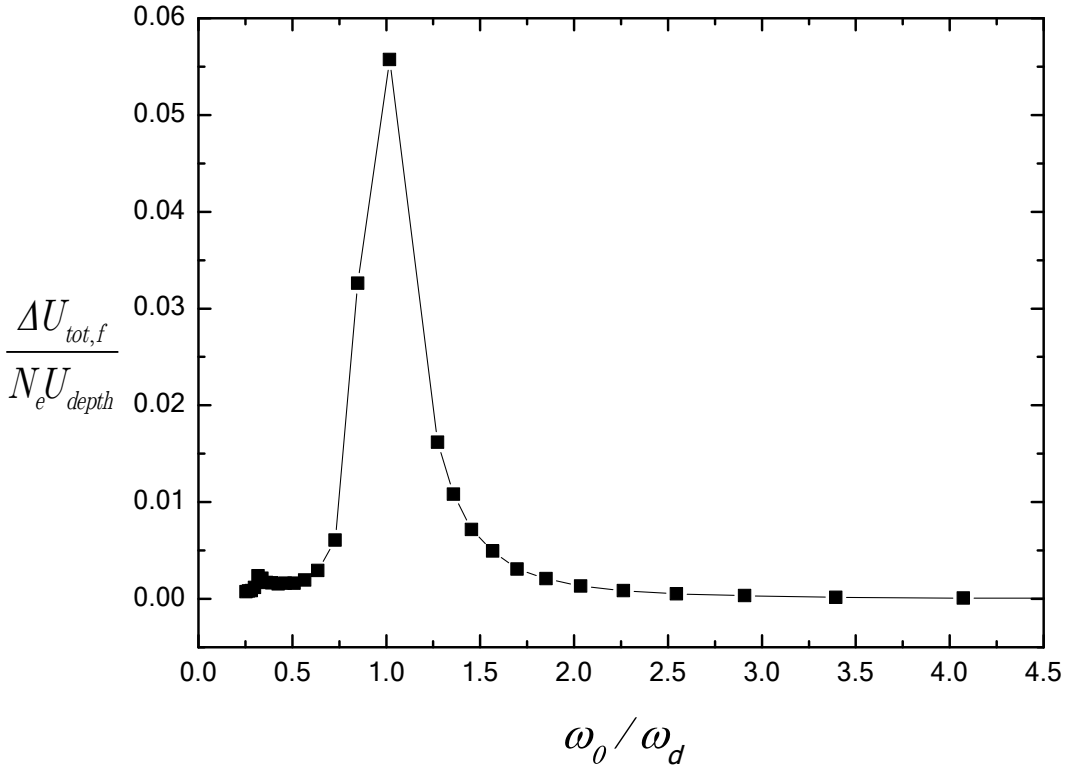

Figure 4.13: *Final Energy increase $\Delta U_{tot,f}$ for different rf field frequencies ω_d.*

4.4 Conclusions

In this chapter an external field $E_0 \cos(\omega_d t + \phi_0)$ was introduced to study the accompanying collisionless absorption. Ultracold plasma do not remain neutral and as a result every electron interacts not only pair-wise with the other particles, but also with the so-called self-consistent electrostatic plasma potential. The origin of the collisionless absorption is the disturbance by the external rf field on the trajectories of the electrons inside the plasma potential. The external rf field induces a polarization field inside the plasma that oscillates at the same frequency, but has a different amplitude E_{int}. This internal rf field exerts work per unit time on the electrons in the plasma, which is the rate of collisionless absorption.

The harmonic 1D potential was chosen as a model potential, because it is possible

to find exact solutions for the amount of energy absorption with quantum mechanics as well as classical mechanics. It was found that irreversible energy absorption occurs only if the driving field frequency is exactly equal to the harmonic potential frequency, as confirmed by classical and quantum-mechanical calculations and by GPT simulations.

The collisionless absorption rate was also calculated in a more realistic three-dimensional plasma potential: the error potential. The error potential resembles a harmonic potential near its center, but has clear anharmonicity when moving away from the center of the potential. As a consequence the oscillation frequency depends on the energy of the electron since the energy determines how far the electron moves into the anharmonic region of the potential. Closed analytical expression for the trajectories in the error potential are unknown and the absorbed energy could only be obtained by the numerical GPT simulations. A electron cloud was simulated with a Maxwell-Boltzmann distribution, such that the electrons had different oscillation frequencies $\Omega(U)$ already at the start of the simulation. The dominant absorption was found at the harmonic resonanance frequency, this was expected since a large amount of the electrons in the cloud is oscillating with a small amplitude around the center of the the cloud. A significant amount of irreversible energy absorption was found for driving frequencies different from the harmonic frequency ω_0, caused by the anharmonicity of the error potential

In ultracold plasmas it is often desired to suppress the amount of rf energy absorption and therefore it would be necessary to choose a driving field frequency significantly far away from the harmonic resonance frequency. Figure 4.13 showed that a field frequency of about $\omega_d > 2\omega_0$ already leads to strong suppression of collisionless energy absorption.

Collisional absorption

In the previous chapter it was found that the amount of energy absorption from an rf field strongly depended on the ratio of the applied frequency and the natural frequency of the plasma potential. The studied collisionless absorption was independent of the individual pair-particle interactions.

In this chapter an absorption mechanism will be studied which completely relies on the individual electron-ion collisions: collisional absorption, sometimes called inverse bremstrahlung. The physical principle of the mechanism is that the oscillating motion of the electrons in the internal rf field $E_{int}\cos(\omega_d t)$ is scrambled due to the Coulomb field of the randomly distributed ions. As a result, energy of the driving rf field is converted into random thermal motion of the electrons.

In section 5.1 the underlying physical principles of collisional absorption will be illustrated. In the subsequent section 5.2 it will be explained how the electron-ion collision frequency changes due to the presence of the rf field. The different physical principles as well as analytical formulas of the first two sections will be tested with simulations in section 5.3.

5.1 Mulser-Bauer theory

A hard-sphere model is considered in figure 5.1, where an electron with relative velocity $\vec{v}_0$ and incident angle θ_i collides with an atom or ion at time t_0. After the collision, the velocity equals $\vec{v}_0'$ with reflecting angle θ_f. Without the rf field $\vec{E}'\cos(\omega_d t)$, the problem reduces to the well-known elastic hard-sphere scattering of an electron with an atom or ion such that $|\vec{v}_0| = \left|\vec{v}_0'\right|$ and $\theta_i = \theta_f$ [42].

In the presence of an rf field the velocity of the incoming electron becomes, if all other forces on the electron are neglected:

$$\vec{v}(t) = \vec{v}_0 - \frac{eE_{int}}{m_e\omega_d}\sin(\omega_d t)\vec{e_x} = v_0\vec{e_i} - \sin(\omega_d t)\vec{v}_{osc} \tag{5.1}$$

with,

$$\vec{v}_{osc} = \frac{eE_{int}}{m_e\omega_d}\vec{e_x} \equiv v_{osc}\vec{e_x}$$

where $\vec{e_i}$ is unit vector pointing in the initial direction of the electron and v_{osc} is the so-called quiver velocity.

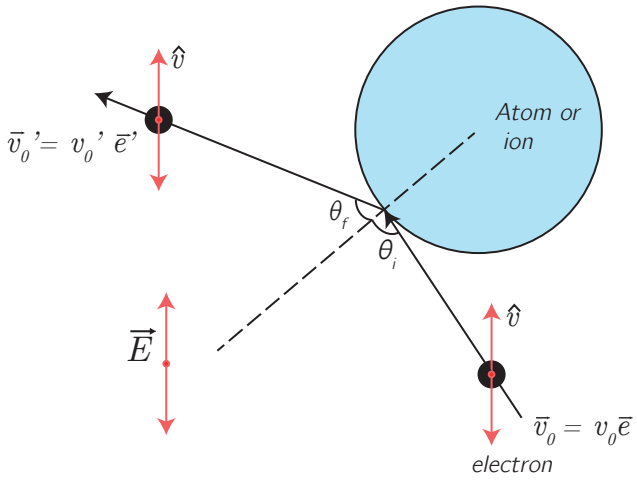

Figure 5.1: *Collision of an electron with an ion while experiencing an external rf field.*

At $t = t_0$ the electron experiences a collision with the ion and is re-directed in the direction $\vec{e_f}$. The velocity at $t = t_0$ becomes $\vec{v}(t_0) = |v_0\vec{e_i} - \sin(\omega_d t_0)\vec{v}_{osc}|\,\vec{e_f}$ as follows from equation (5.1).

For times $t' > t_0$ the velocity can be written as:

$$\begin{aligned}\vec{v}\left(t'\right) &= \vec{v}(t_0) - \vec{e_x}\frac{eE_{int}}{m_e}\int_{t_0}^{t'}\cos(\omega_d t)\mathrm{d}t = \vec{v}(t_0) - \vec{v}_{osc}\left[\sin(\omega_d t') - \sin(\omega t_0)\right] \\ &= |v_0\vec{e_i} - \sin(\omega_d t_0)\vec{v}_{osc}|\,\vec{e_f} - \vec{v}_{osc}\left[\sin(\omega_d t') - \sin(\omega_d t_0)\right]\end{aligned} \tag{5.2}$$

where the expression for $\vec{v}(t_0)$ was substituted in the second line.

The change in kinetic energy induced by the collision $\frac{1}{2}m_e(v^2(t') - v^2(t)$ is calculated under two assumptions. The first assumption is that the time of the collision t_0 can be chosen arbitrarily and as a result the direction after the collision $\vec{v}(t_0) \sim \sin(\omega_d t)$ is also arbitrary. Furthermore, in the hard-sphere model the electrons do not feel any potential force from the ion or atom before or after the collision. As a consequence the time t before the collision can be arbitrarily close to t_0.

Therefore the limit $t \to t_0$ is used and the change in kinetic energy is averaged over one rf cycle $2\pi/\omega$. The details of the derivation can be found in appendix A.3.

The gain in kinetic energy becomes:

$$\frac{1}{2}m_e\overline{\Delta\vec{v}^2} = \frac{1}{2}m_e\vec{v}_{osc}^2 = \frac{(eE_{int})^2}{2m_e\omega_d^2} = 2U_p \tag{5.3}$$

where $U_p = (eE_0)^2/(4m_e\omega_d^2)$ is the ponderomotive potential that was briefly mentioned in section 4.2.

The average energy gain per unit time, per electron, can be estimated as:

$$\frac{\mathrm{d}\langle U\rangle}{\mathrm{d}t} = 2\nu_{ei}U_p \tag{5.4}$$

where ν_{ei} is the average number of electron-ion collisions per second. The derivation of ν_{ei} will be the topic of the next section.

The collisional absorption causes the total energy U_{tot} of the ultracold plasma to increase, which simply follows from equation (5.4): $\frac{\mathrm{d}U_{tot}}{\mathrm{d}t} = N_e \cdot \frac{\mathrm{d}\langle U\rangle}{\mathrm{d}t}$, with N_e the number of electrons in the plasma.

5.2 Collision frequency in rf driven plasma

At first instance one might use the well-known Spitzer frequency ν_s, derived for the rate of electron-ion collisions in conventional plasmas without rf field [1, 43]:

$$\nu_s = \sqrt{\frac{2}{3\pi}}\omega_p\Gamma_e^{3/2}\ln(\Lambda_e) \tag{5.5}$$

where Γ_e is the coupling parameter from equation (1.1) and $\ln(\Lambda_e) = \ln\left(\Gamma_e^{2/3}\right)$ is the Coulomb logarithm. In the derivation of ν_s it is assumed that an electron approaches an ion with a thermal velocity $v_{th} = \sqrt{k_b T_e/m_e}$, but in an rf field there is also a quiver velocity v_{osc} present.

The Coulomb logarithm needs to modified and an additional pre-factor is required in equation (5.5) to obtain the collision frequency in the presence of an rf field.

A model which takes into account both the thermal velocity and the quiver velocity, results in the following pre-factor for the effective collision frequency [8, 44]:

$$\nu_{ei} = {}_2\mathrm{F}_2\left(\frac{3}{2},\frac{3}{2};2,\frac{5}{2};-\frac{v_{osc}^2}{2v_{th}^2}\right)\cdot\nu_s \tag{5.6}$$

where ${}_2\mathrm{F}_2$ is the hypergeometric function of second order which has the following limiting forms:

$$\begin{aligned} &{}_2\mathrm{F}_2(...) \approx 1 && \text{if } v_{osc} \ll v_{th} \\ &{}_2\mathrm{F}_2(...) \approx 6\sqrt{\frac{2}{\pi}}\left(\frac{v_{th}}{v_{osc}}\right)^3\left[\ln\left(\frac{v_{osc}}{v_{th}}\right)+1\right] && \text{if } v_{osc} \gg v_{th} \end{aligned} \tag{5.7}$$

and it follows that in the weak-field limit $v_{osc} \ll v_{th}$ the Spitzer frequency is recovered in equation (5.6).

In the limit for very strong fields on the other hand, $v_{osc} \gg v_{th}$, ${}_2\mathrm{F}_2(...) \sim (v_{th}/v_{osc})^3\ln(v_{osc}/2v_{th})$ while the Spitzer frequency from equation (5.5) is proportional to $\Gamma_e^{\frac{3}{2}} \sim v_{th}^{-3}$.

In that case the collisional absorption per unit time from equation (5.4) becomes proportional to:

$$\frac{\mathrm{d}\langle U_{tot}\rangle}{\mathrm{d}t} = 2\nu_{ei}U_p \sim \frac{1}{v_{osc}^3}\ln\left(\frac{v_{osc}}{2v_{th}}\right)\cdot v_{osc}^2 \sim \frac{\ln\left(\frac{v_{osc}}{v_{th}}\right)}{v_{osc}} \tag{5.8}$$

It follows that the collisional absorption rate *decreases* for increasing v_{osc} in the limit $v_{osc} \gg v_{th}$.

Note that it is not necessary to use a very strong *external* rf field amplitude to go into the range $v_{osc} \gg v_{th}$. In section 4.1 it was derived that the rf field amplitude in the plasma was given by $E_{int} = E_0/(1 - \omega_m^2/omega_d^2)$, so an alternative way to go into the strong-field limit is to use a field frequency ω_d close to the resonant Mie-frequency.

In figure 5.2 the scaled collision frequency ν_{ei}/ν_s is plotted against the ratio v_{osc}/v_{th}. The black line is the hypergeometric function, the red dashed line is the strong-field limit $v_{osc} \gg v_{th}$ and the dash-dotted blue line gives the weak field limit. In UCPs, the ratio of v_{osc}/v_{th} can be in the strong-field limit due to the low electron temperatures.

The effective collision frequency is clearly suppressed for $v_{osc}/v_{th} > 1$ and the application Spitzer frequency would lead to an overestimation of the absorbed energy.

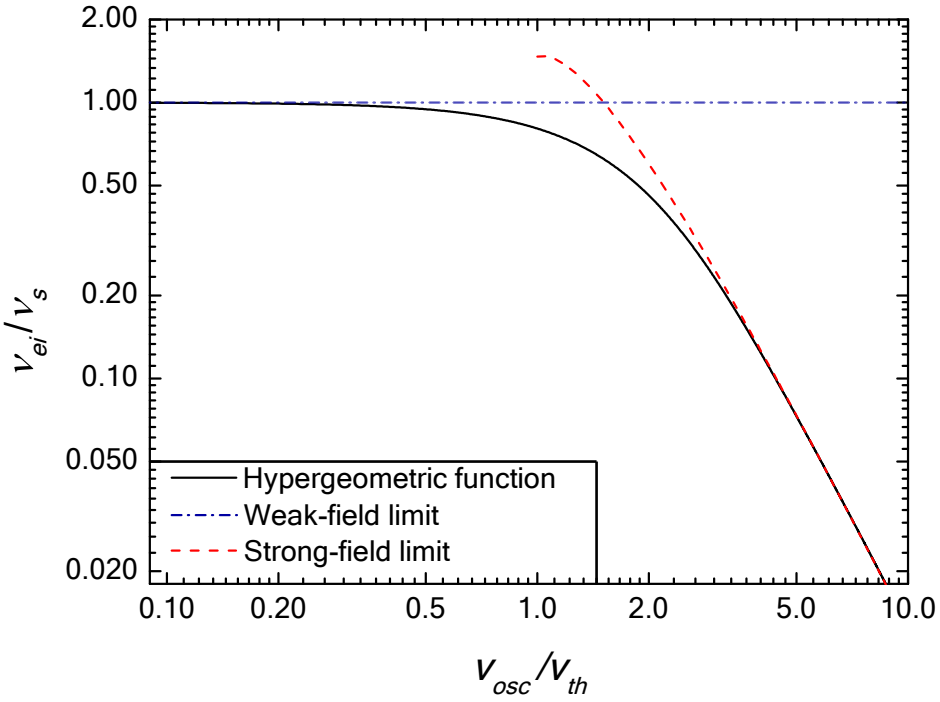

Figure 5.2: *Electron-ion collision frequency ν_{ei}/ν_s as a function of the ratio of quiver and thermal velocity*

The decrease in the collision frequency can be understood from the Rutherford scattering cross section σ_R which depends on the relative velocity v_{rel} of the electron: $\sigma_R \sim \frac{1}{v_{rel}^4}$. The average value of v_{rel}^4 increases due to the presence of the quiver velocity. A larger field amplitude E_{int} leads to a larger quiver velocity and therefore the collision cross section σ_R decreases as a function of v_{osc} and with that the collision frequency

(since $\nu \sim \sigma$ [1]).

The second modification to the collsion frequency of equation (5.5) concerns the Coulomb logarithm $\ln(\Lambda_e) = \ln\left(\frac{b_{max}}{b_{min}}\right)$, where b_{min} and b_{max} are the two cut-offs of the well-known Coulomb collision integral [42]:

$$\nu_s = \sqrt{\frac{2}{3\pi}}\omega_p \Gamma^{3/2} \int_{b_{min}}^{b_{max}} \frac{\mathrm{d}b}{b} \tag{5.9}$$

where b is the impact parameter, also illustrated in figure A.1 in section 3.2. The two cut-offs are required since the integral diverges both in $b \to 0$ and $b \to \infty$.

In standard plasma physics textbooks it is assumed that an electron approaching an ion with an impact parameter larger than the Debye length does not interact with the ion, since the electron-ion interaction is (Debye-)shielded by other electrons in the plasma [1, 42]. Therefore the upper limit is chosen equal to the Debye length: $b_{max} = \lambda_D = v_{th}/\omega_p$ with ω_p the plasma frequency.

The minimal impact parameter b_{min} is defined as the impact parameter which leads to a 90 ° collision. At a distance $r = b_{min}$, the potential energy is twice the relative kinetic energy between the ion and electron at $r \to \infty$ [42]. These type of collisions are very rare in a conventional plasma since the coupling parameter $\Gamma_e = \frac{\langle U_{pot} \rangle}{\langle U_{kin} \rangle} \ll 1$. The expression for the minimal impact parameter becomes $b_{min} = \frac{e^2}{4\pi\epsilon_0 m_e v_{th}^2}$ [42].

The influence of the rf field is implemented in the collision theory by defining a new effective velocity: $v_{eff} = \sqrt{v_{th}^2 + v_{osc}^2}$ [45]. Under that the assumption the cut-off parameters become:

$$\begin{aligned} b_{max} &= \frac{v_{eff}}{\max(\omega_d, \omega_p)} \\ b_{min} &= \frac{e^2}{4\pi\epsilon_0 m_e v_{eff}^2} \end{aligned} \tag{5.10}$$

where $\max(\omega_d, \omega_p) = \omega$ if $\omega_d > \omega_p$ and vice versa.

For strongly coupled plasmas these two cut-offs are not justified anymore, because $\Gamma_e > 1$. Ultracold plasmas with initial temperature $T_e(0) = 0$ are heated quickly to the value $\Gamma_e = 1$ due to disorder-induced heating as shown in chapter 3, which means that these ultracold plasmas are close to the region where this theory is not applicable anymore. Therefore, weakly-coupled ultracold plasmas were simulated with $\Gamma_e(t = 0) < 0.2$, as will be shown in the next section.

5.3 Numerical simulations of collisional absorption

5.3.1 Simulation conditions

Numerical simulations were performed to test the derived expressions and principles in the previous sections. Since the theory for the collision frequency only applies to weakly coupled plasmas, an initial electron temperature of $T_e(0) = 70$ K was chosen which leads to an initial coupling parameter of $\Gamma_e(0) \approx 0.2$.

The rf field frequency ω_d should be chosen significantly far away from the Mie-frequency, because at the the Mie-frequency the internal field amplitude $E_{int} = E_0/(1-\omega_m^2/\omega_d^2)$ diverges. An additional prerequisite is that the frequency ω_d should not be chosen smaller than ω_m, because this would lead to a 'stripping' of the boundary of the plasma. The underlying mechanism behind this effect is the dependence of the Mie-frequency on position in a non-uniform particle distribution. The electron density n_e of the plasma is generally not a uniform function and evolves in time. Initially, the electron cloud expands due to its temperature resulting in a net plasma potential, as was shown in the introduction in chapther 4. As a result the Mie frequency $\omega_m = \sqrt{(n_e(r)e^2)/(3m_e\varepsilon_0)}$ becomes also dependent on the position in the plasma.

This is illustrated in figure 5.3, where the ion and electron density are shown as a function of the radius of the plasma at the end of a simulation at $\omega_m t = 20$. Both the ion and electron density were uniform at $\omega_m t = 0$, the initial ion temperature was $T_i = 0$ K and the initial electron temperature was $T_e = 70$ K.

The ion density is still approximately uniform in the original plasma sphere of radius R_b, but the electron density has evolved into a monotonously decreasing function of radial position. This means that the Mie-frequency $\omega_m \sim \sqrt{n_e(r)}$ is also monotonously decreasing. The value of the Mie-frequency, scaled with the initial Mie-frequency $\omega_{m,0}$, is shown on the right axis of figure 5.3. If for example an rf field is applied with a frequency $\omega \approx \omega_{m,0}/2$ the electrons at $r = R_b$ from figure 5.3 will be in resonance and they will be driven out of the plasma.

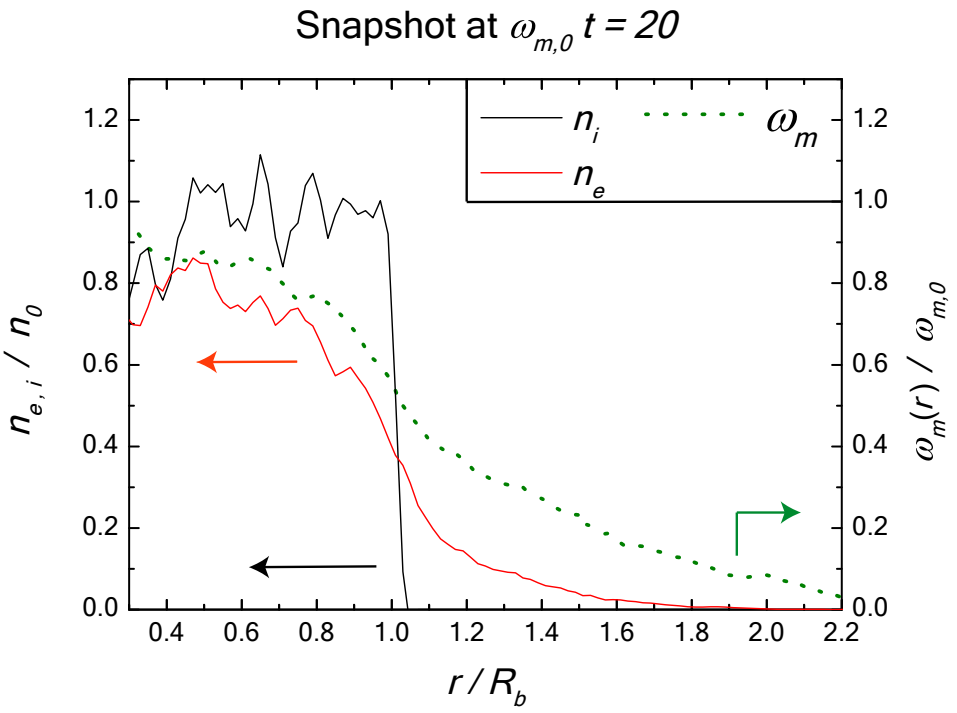

Figure 5.3: Left axis*: Electron (red) and ion density (black) scaled with the initial density at* $\omega_m t = 0$ *as a function of the distance to the center of the plasma.*
Right axis*: Mie-frequency* $\omega_m(r)$ *(dotted olive) scaled with the uniform Mie-frequency at* $\omega_m t = 0$

5.3.2 Influence of collisionless absorption

The goal is to study collisional absorption as independently as possible from other absorption mechanisms. This means that the applied field frequency ω_d should be far away from the dominant resonance ω_0 of the plasma potential, as was in figure 4.13 in chapter 4. Therefore, an estimation is made of the resonance frequency of the plasma potential by simulating the ultracold plasma with Coulombic particle-interactions, but without an rf field.

The used parameters in the simulation were an electron temperature of $T_e(0) = 70$ K, an ion temperature of $T_i(0) = 0$ K, $N_e = N_i = 4000$ electrons and ions initialized in a sphere with an initially uniform densities of $n_{e,0} = n_{i,0} = 10^{-16}$ m^{-3}.

As a result of the escape of the thermal electrons a plasma potential is quickly built up, usually in a time scale $\omega_m t < 2$ and gradually evolves or deepens in the remaining simulation time $2 < \omega_m t < 20$. The development of the potential was also explained in the introduction of chapter 4 and can be reviewed in figure 4.1. Conclusively, the plasma potential is not static and it can be assumed that the rate of collisionless absorption is the largest at the end of the interval, $\omega_m t = 20$, since the plasma potential is at its steepest at the end of the simulation.

The average plasma potential at the end of the simulation $\omega_m t = 20$ is plotted as a function of the distance to the center of the plasma r in figure 5.4 . The red line is the average radial force an electron experiences as a function of the distance to the center of the plasma. In the center of the plasma $r < (3/4)R_b$ the influence of the plasma potential of the electrons is negligible, but in the region $(3/4)R_b < R_b$ the electron experiences an approximately linear restoring force. In the region $r > R_b$ the restoring force becomes non-linear with respect to x and decrease to zero.

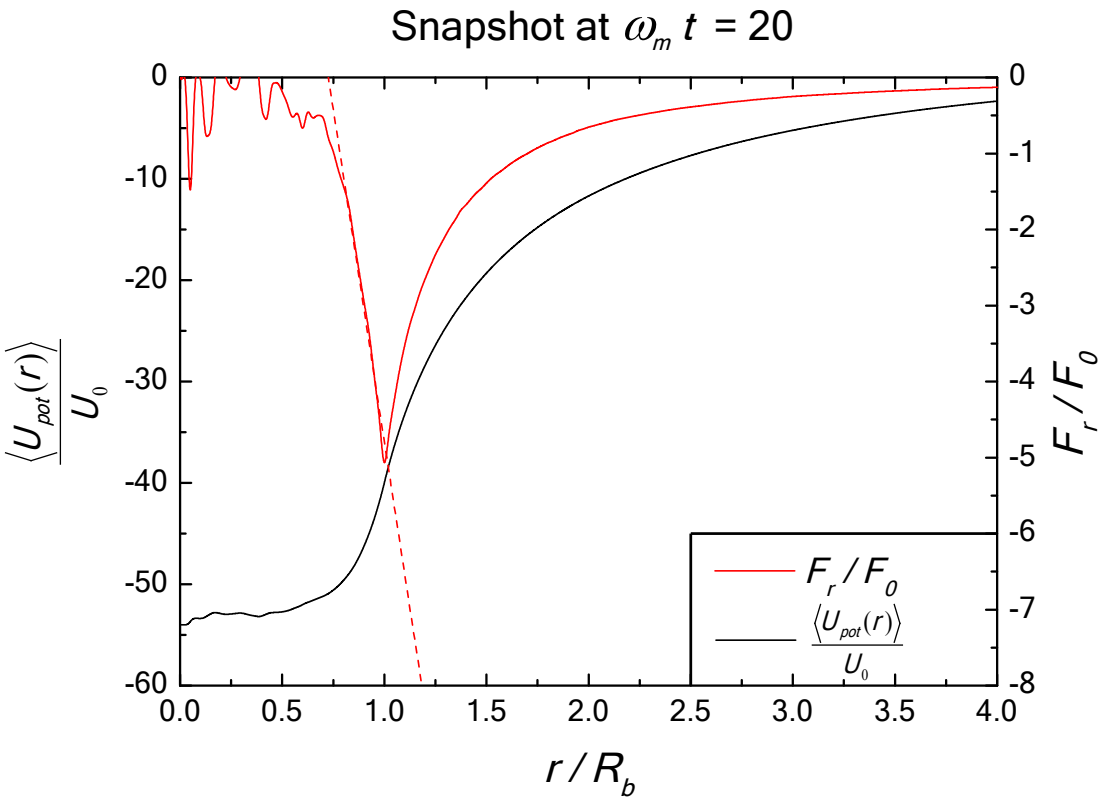

Figure 5.4: *Left(black): Average potential energy as a function of the radius. Right(red): Average radial force on a electron scaled with the typical Coulomb force F_r/F_0.*

Suppose the plasma potential is not gradually evolving and deepening for $0 < \omega_m t < 20$ but *static* during the simulation and moreover equal to the potential at $\omega_m t = 20$ from figure 5.4. The amount of collisionless absorption in that *static* potential could be regarded as a limit, or worst-case scenario, for the amount of collisionless absorption in the evolving potential.

It can be assumed that the dominant frequency of a typical plasma potential is on the order of the oscillation frequency of the electrons in the plasma potential [8]. The majority of the electrons (about 80-90 %) will reside in the region $r < R_b$ during the simulation. An approximation of a cross-section of the plasma potential, in the

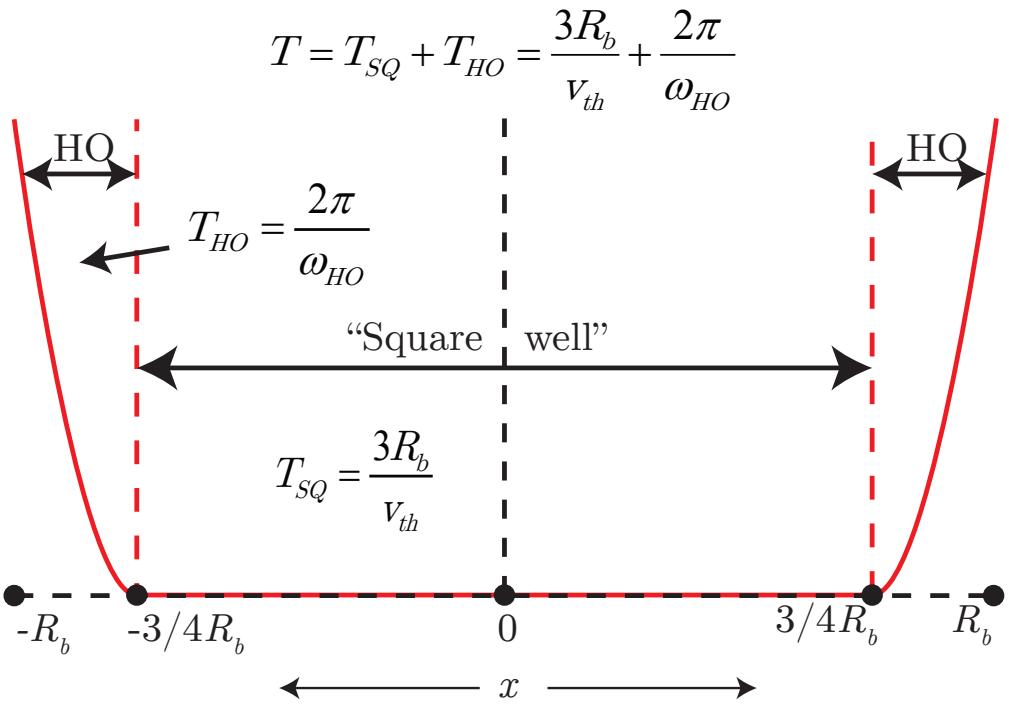

Figure 5.5: *Approximation of the cross-section of the potential between $x = -R_b$ and $x = R_b$.*

range $-R_b < x < R_b$, is shown in figure 5.5. The potential can be regarded as a harmonic potential with a connecting flat potential placed in the middle of the harmonic potential. The total period of the electrons T with a bounded motion in $-R_b < x < R_b$ is given by $T = T_{HO} + T_{SQ}$, where $T_{HO} = 2\pi/\omega_{HO}$ is the harmonic oscillator period and $T_{SQ} = 3R_b/v_{th}$ is the time it takes an electron with thermal velocity v_{th} to traverse through the flat potential region, which can be regarded as a square well period.

A linear fit is applied to the force in the region $(3/4)R_b < r < R_b$ to estimate the harmonic frequency, as shown in figure 5.4 by the red dashed line. The slope of the fit α can be related to harmonic frequency; $\omega_{HO} = \sqrt{\frac{\alpha F_0}{m_e R_b}} = (3.5 \pm 0.1) \cdot 10^9$ rad/s and from that $T_{HO} = (1.79 \pm 0.05)$ ns. The thermal velocity is $v_{th} = \sqrt{k_b T_e / m_e}$ with $T_e = 70$ K and the original plasma radius is given by $R_b = (3N_e/4\pi n_e)^{1/3}$ with N_e the number of electrons. This leads to a square well period of $T_{SQ} \approx 4.2$ ns. From this it follows that the total oscillation frequency of the electrons in the potential is $\omega_0 = 2\pi/T \approx 1.05 \cdot 10^9$ rad/s.

As previously mentioned the plasma potential is only gradually evolving into the potential of figure 5.4, and therefore the value of ω_0 is a certain worst-case scenario for

the amount of collisionless absorption. It can be concluded that at any time before the end of the simulation $\omega_0 < 1.05 \cdot 10^9$ rad/s.

As explained in the introduction the second prerequisite is to choose the field frequency larger than the Mie-frequency ω_m.

Therefore, a field frequency $\omega_d = 1.41 \cdot 10^{10}$rad/s $\approx 14\omega_0 \approx 4\omega_m$ was chosen, expected to result in a negligible amount of collisionless absorption from previous results in chapter 4. Furthermore this frequency only leads to small amplification of the field amplitude inside the plasma since $E_{int} = E_0/(1 - \omega_m^2/\omega_d^2) \approx 1.06E_0$.

The change of the total energy is fully taken up by the electrons. Therefore the mean energy gain of the electrons is simply the total energy of the plasma divided by the number of electrons present in the plasma.

An alternative point of view is that the amount of energy absorption is equal to the work that is performed by the induced electric field in the plasma. From the work-energy theorem of classical mechanics [46], it follows that the amount of work performed by an induced field on an ion is equal to the change in the energy of the ion: $\frac{\mathrm{d}U}{\mathrm{d}t} = e\vec{E}' \cdot \vec{v_i}(t) \approx 0$ since the ions are nearly stationary in the time scales of the simulations, so only the electrons contribute to the change of the total energy of the system.

The total energy gain was expressed in terms of $N_e U_0$, where N_e is the number of electrons in the plasma and $U_0 = e^2/(4\pi\varepsilon_0 a_0)$ is the typical Coulombic interaction energy with Wigner-Seitz radius a_0.

5.3.3 Results

In figure 5.6 the energy gain, expressed in terms of $N_e U_0$, is plotted as a function of time for two different field amplitudes. The total energy at $t = 0$ is given by $U_{tot}(0)$, N_e is the number of electrons in the plasma and $U_0 = e^2/(4\pi\varepsilon_0 a_0)$ is the typical Coulombic interaction energy with Wigner-Seitz radius a_0.

The cycle-averaged energy is gradually increasing and the fast oscillations $\sim \omega_d$ are due to the presence of the rf field. The amplitudes of the oscillations are not constant indicating the presence of other oscillations, besides the rf field oscillation at frequency ω_d. Those other oscillations are probably related to the Mie-frequency or the resonance frequency of the plasma potential.

It would be convenient to distil the slowly increasing part from the rapidly oscillating part. Especially at larger field strengths the amplitudes of these oscillations become very large. The first suggestion might be to average the energy over the period of the oscillation in figure 5.6. The problem is that the oscillation frequency of the oscillations in figure 5.6 is not a priori known. A simple 1D jellium model as in section 4.1, which assumes a fluid description, could be used to estimate the oscillating frequency. However, an averaging procedure over the interval $t \in [0, T_{osc}]$, with T_{osc} the period of the oscillation is quite sensitive for a small mismatch of the factor ω_0, which would lead to the addition of other harmonics to the current oscillations.

An alternative could be to subtract the energy of an electron oscillating in an rf field, since the collisional absorption is assumed to be due to the deflection of an rf field oscillation of the electron by the stationary ions. The energy of an electron in an rf field,

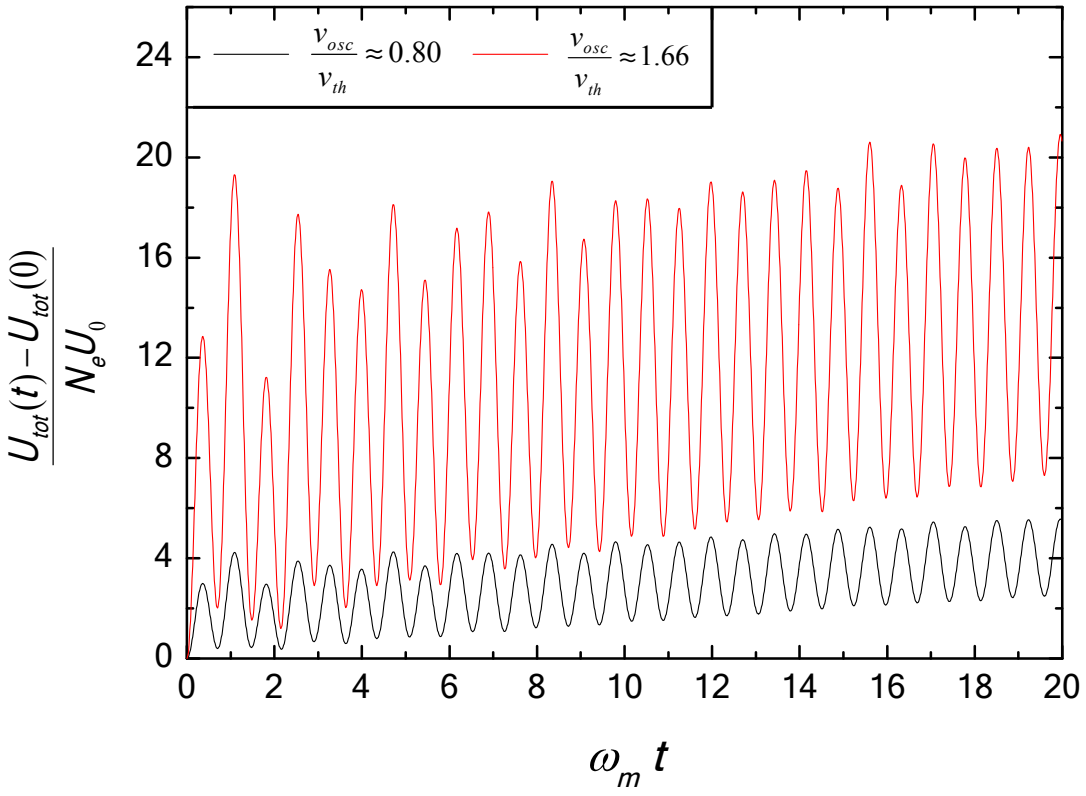

Figure 5.6: *Energy gain as a function of time for two different quiver velocities* v_{osc}.

which is called the quiver energy, equals $U_{quiver} = 2U_p \sin^2(\omega t)$; a factor that oscillates in time but does not contribute to an average increase of the energy.

The result of this subtraction is shown in figure 5.7. The black line shows the scaled energy increase for $v_{osc}/v_{th} \approx 1.66$ and in the blue dashed line the quiver energy is subtracted from $\bar{\epsilon}$. Remaining oscillations are still present, but with a smaller amplitude and therefore it would be easier to estimate the energy gain by linear fit of the blue dashed line.

However, a more practical way to distil the linear energy increase is by spectral filtering of the Fourier spectrum. The energy gain plotted in figure 5.7 is just a discrete set of N_D=2000 data points and thus could be expanded by using the discrete fourier transform in the series $\sum_{k=0}^{N_D-1} Y(k) \exp\left(2\pi i \frac{kn}{N_D}\right)$, for $n = 0, 1, 2, ..., N_D - 1$ [41]. The discrete variable n refers to a specific data point in the set which corresponds to a certain time in our case. The expansion parameter k is limited by the number of data points and $Y(k)$ is the amplitude of the corresponding exponential. The values of $Y(k)$ determine the contribution of a certain harmonic oscillation $\exp\left(2\pi i k \frac{n}{N_D}\right) = \exp\left(2\pi i k \frac{t}{t_f}\right) = \exp(i\omega t \cdot k)$ in the analyzed data set. The discrete variable n corresponds to a time in the time simulation and N_D corresponds to the total simulation time $t_f = 20\omega_m$.

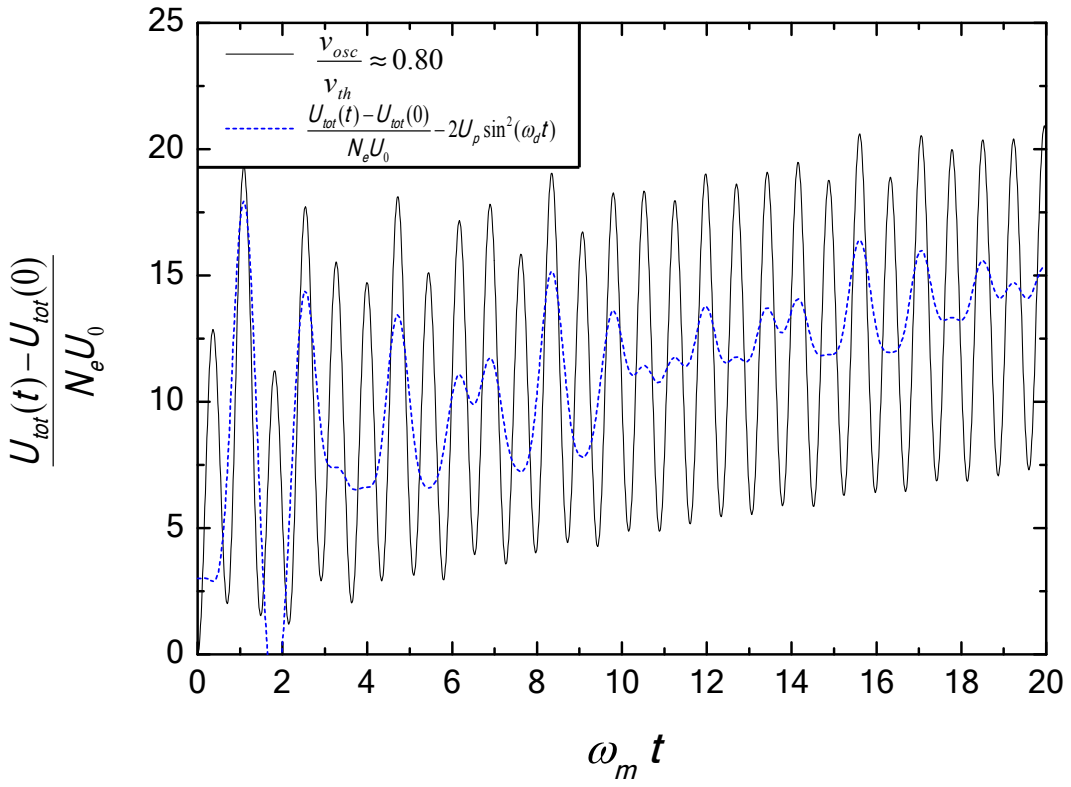

Figure 5.7: *Energy gain as a function of time (black). The blue dashed line results from the subtraction of the quiver energy from the energy gain.*

Therefore, the Fourier series can be written in terms of the exponentials $\exp\left(2\pi ik\frac{n}{N_D}\right) = \exp\left(2\pi ik\frac{t}{t_f}\right) = \exp\left(it\frac{\pi}{10}\omega_m k\right) = \exp\left(i\omega_k t\right)$, with $\omega_k = k \cdot \frac{\pi}{10}\omega_m$.

From this it follows that the slowest possible oscillation in figure 5.7 that can be described by the Fourier series ($k = 1$) has a frequency $\omega = \frac{\pi}{10}\omega_m$. The total simulation time t_f should be increased if it is desired to describe slower oscillations with Fourier series.

The fastest possible oscillation in the expansion on the other hand equals $\omega_{N_D-1} = 199.9\pi\omega_m$ since the amount of data points in the simulation equalled $N_D = 2000$. This time the spacing between the successive data points in a set should be increased to describe faster oscillations.

The Fourier spectrum of the original energy oscillations $\frac{U_{tot}(t)-U_{tot}(0)}{N_e U_0}$ of figure 5.7 is shown in figure 5.8. The y-axis gives the absolute value of the complex Fourier amplitude $|Y_k|$, which indicates the contribution of a certain harmonic oscillation at the frequency ω on the x-axis to the original function $\frac{U_{tot}(t)-U_{tot}(0)}{N_e U_0}$.

The largest peak in the spectrum at $\omega/\omega_d = 2$ corresponds to the quiver energy since

$2U_p \sin^2(\omega_d t) = U_p[1 - \cos(2\omega_d t)]$. Apart from this oscillations there a few small peak visible in the region $0.5 < \omega/\omega_d < 1.5$, probably related to the Mie-frequency and the natural plasma frequency ω_0.

First the largest peak between the red dashed lines, corresponding the quiver energy, is removed from the spectrum. An inverse Fourier transform is applied to the new spectrum, which results in the red dashed line; the black line corresponds to the original energy function $\frac{U_{tot}(t)-U_{tot}(0)}{N_e U_0}$. The result is already an improvement compared to the method of simply subtracting the quiver energy in figure 5.7, although there is still a significant oscillation left.

A further improvement is obtained if the small peaks in the region $0.5 < \omega/\omega_d < 1.5$ are removed too. Therefore, all the peaks in the region between the straight blue lines are removed. The inverse Fourier transformation is applied to the new spectrum. The result is the blue straight line in figure 5.9.

The effective electron-ion collision frequency ν_{ei} is easily found by a linear fit of the blue curve. This yields a value β for the slope defined as:

$$\beta = \frac{\mathrm{d}}{\mathrm{d}\omega_m t}\left(\frac{U_{tot}(t) - U_{tot}(0)}{N_e U_0}\right) = \frac{1}{\omega_m t}\frac{\mathrm{d}\langle U\rangle}{\mathrm{d}t} \tag{5.11}$$

which can be used to calculate $\nu_{ei} = \frac{U_0 \omega_m \beta}{U_p}$; see equation (5.4).

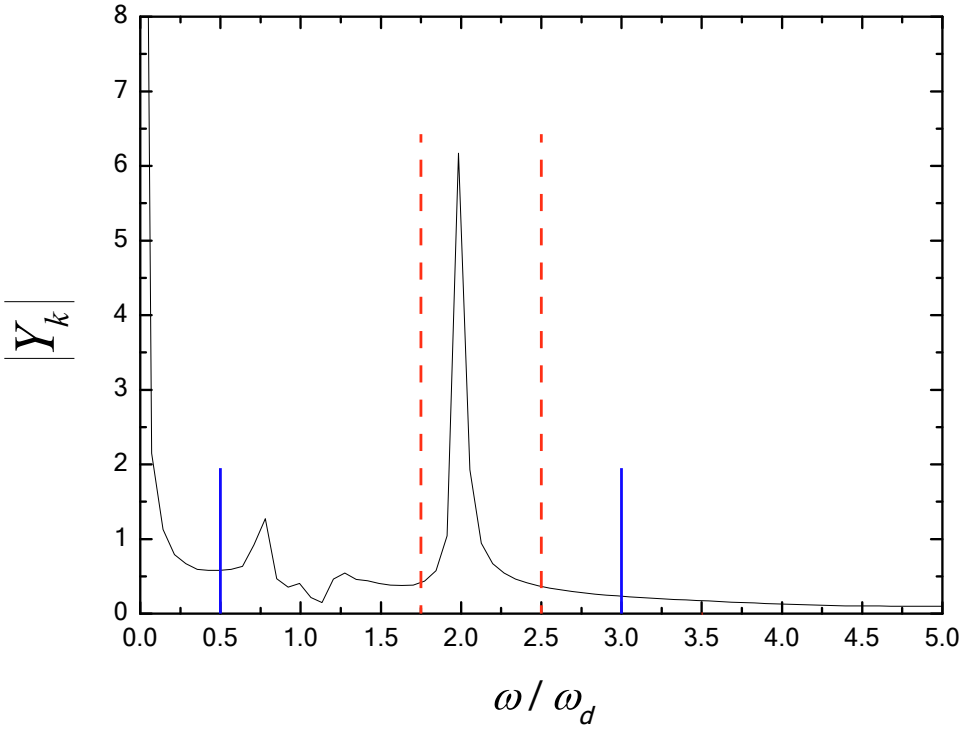

Figure 5.8: *Fourier spectrum of the energy gain from figure 5.7.*

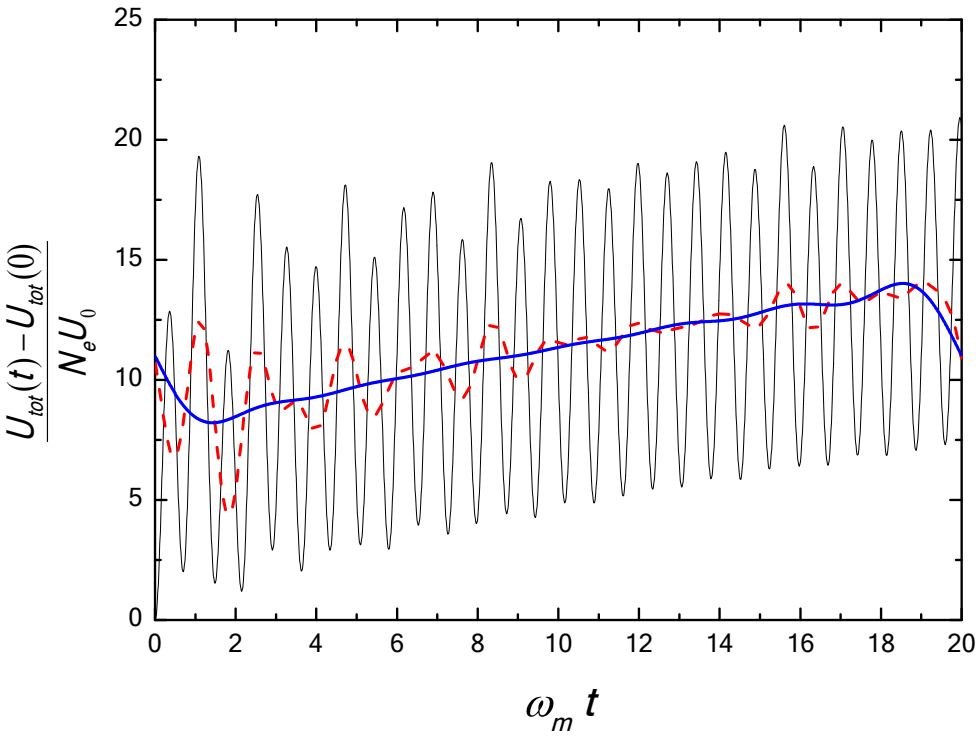

Figure 5.9: *Energy gain as a function of time (black). The red dashed line results after spectral filtering of the largest peak in the spectrum. The blue solid line results after spectral filtering, including the smaller peaks, from the spectrum.*

The average energy increase has been calculated for different field amplitudes or quiver velocities v_{osc}. The results are shown in figure 5.10 The left axis and the black points show the obtained slope β which is plotted as a function of the quiver velocity v_{osc} in units of $v_{th,0}$, the thermal velocity at $t = 0$. The right axis displays the collision frequency ν_{ei} in units of the Spitzer frequency of equation (5.5).

In the region $0.02 < v_{osc}/v_{th} < 2$ the effective energy absorption increases, but for $v_{osc}/v_{th,0} > 2$ the external field is so strong that the amount of collisional absorption decreases as a function of the applied field strength. This confirms the expectation that for strong rf fields the quiver velocity effectively takes over the role of the thermal velocity, as explained in section 5.2.

The blue triangles, on the right axis, display the effective collision frequency, scaled with the Spitzer frequency at $t = 0$. The collision frequency effectively vanishes for very high quiver velocities. In this region the effective electron velocity in the plasma is very close to the quiver velocity and increasing the effective velocity could be interpreted as decreasing the electron-ion (Rutherford) cross-section.

The blue triangles do not agree with the theoretical curve from figure 5.2. The first reason is that neither the thermal velocity nor the Spitzer frequency ν_s is a constant, but increases during the simulation due to the collisional absorption itself. The amount

of increase of the temperature depends strongly on the strength of the applied field, if $v_{osc} > v_{th,0}$ this increase in temperature becomes relevant. For example, the average electron temperature at $v_{osc}/v_{th,0} \approx 4$ was $\langle T_e \rangle \approx 260$ K; considerably larger than the initial temperature $T_e = 70$ K. For $v_{osc}/v_{th,0} < 0.5$, the increase in temperature is insignificant.

The second reason is that the number of electrons which experience electron-ion collisions is not equal to the total amount of simulated electrons. The faster electrons escape from the plasma early on and therefore do not contribute to absorption anymore. The amount of electrons inside the original plasma sphere, where all the ions are residing, varied between 70-100% depending on the strength of the field.

The third reason of the mismatch is that the electron density in the plasma does not remain uniform during the simulation, as was shown in the introduction of this chapter. Therefore the Mie-frequency and likewise the plasma frequency occurring in equation (5.5) for the Spitzer frequency, are not constants but decrease as a function of time.

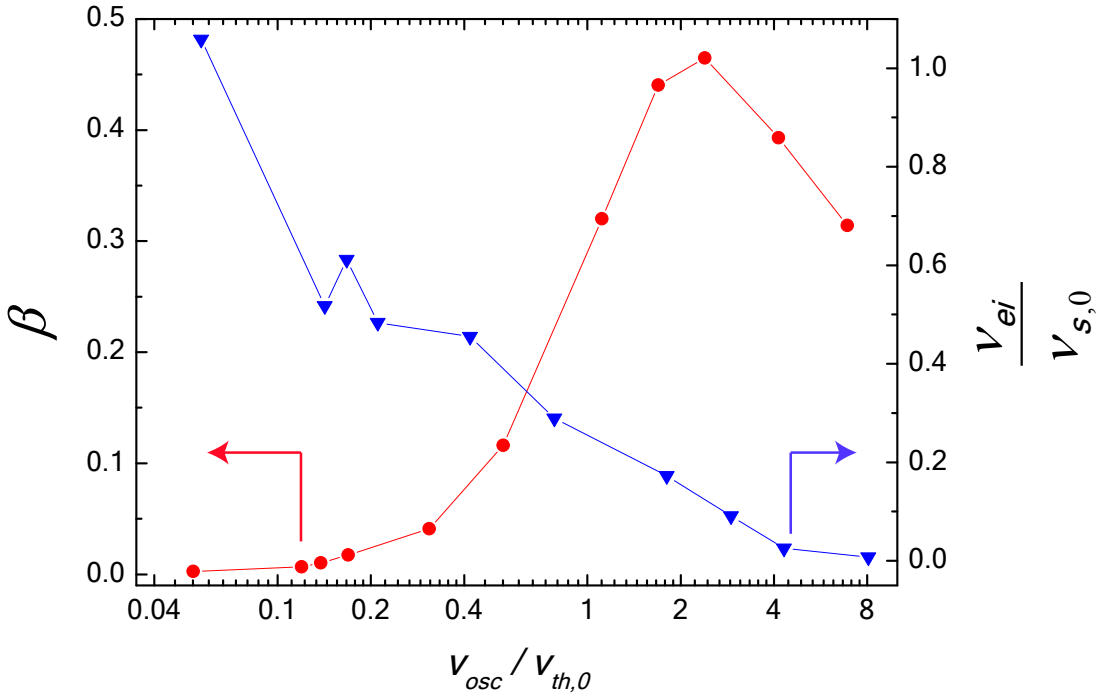

Figure 5.10: *Left(red): Energy absorption $\langle U \rangle / U_0$ per unit $\omega_m t$ as a function of quiver velocity. Right (blue): Electron-ion frequency as a function of quiver velocity.*

In figure 5.11 the effective frequency is scaled with the average Spitzer $\bar{\nu}_s$ frequency of the plasma, which requires the three aforementioned parameters that were averaged over the simulation interval: the electron temperature, the number of electrons in the plasma and the electron density. With the averaged electron temperature and the averaged plasma frequency the Spitzer frequency could be calculated for every point with equation (5.5). The resulting calculated energy gain was multiplied with the fraction $\frac{N_{e,p}}{N_e}$, where

$N_{e,p}$ is the number of electrons in the plasma, to correct for the fact that the number of colliding electrons is not equal to the total number of electrons.

The result is shown in figure 5.11, which shows a good agreement between simulations and analytical theory. The wide green error bars indicate the uncertainties in ν_{ei}/ν_s (vertical) and in v_{osc}/v_{th} (horizontal). The uncertainty in the v_{osc} is especially large for large velocities, due to the increase of the electron temperature during the simulation. Despite the crude averaging procedures the main characteristics of the theoretical curve are confirmed by the simulation. The collision frequency is clearly suppressed for strong applied rf fields, making the standard Spitzer frequency inapplicable to apply for strongly rf-driven plasmas. The Spitzer frequency would lead to an significant overestimation of the amount of collisional absorption, although it has been used in the context of rf absorption by UCPs.

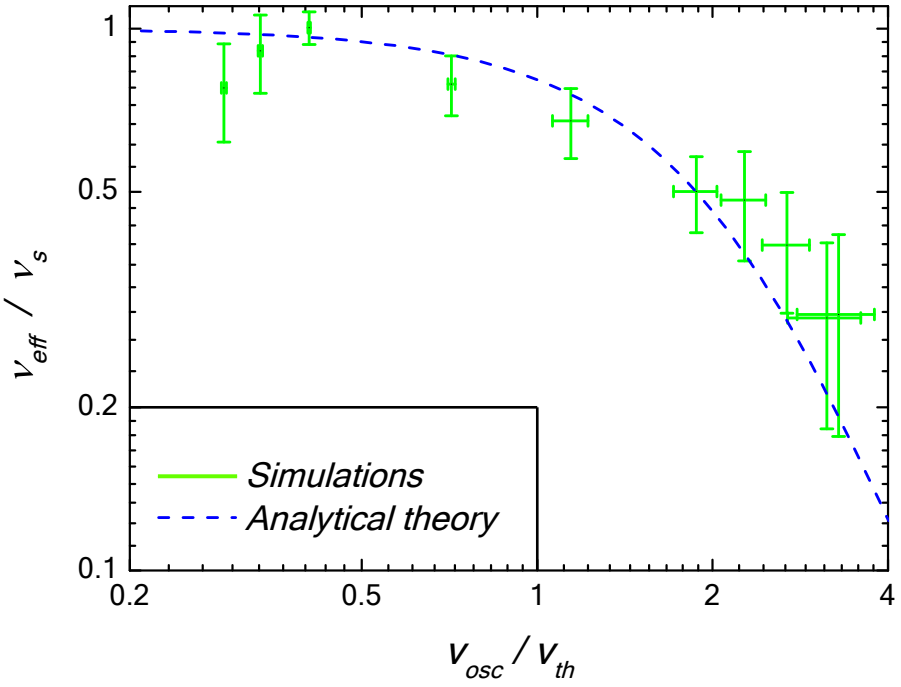

Figure 5.11: *The electron-ion collision frequency, simulation and analytical result, plotted as a function of the scaled velocities.*

5.4 Conclusions

In this chapter heating by collisional absorption was simulated and compared to the available analytical theories. This phenomena arises from the deflection of rf oscillating electrons in the Coulomb fields of the ions. The collisional absorption was studied under

the condition that the amount of collisionless absorption is negligible. The prerequisite on the applied rf field frequency was that it is far away from the resonance frequency ω_0 of the plasma potential. The plasma potential was calculated by simulating a set of electrons and ions with initial temperatures of $T_e(0) = 70$ K and $T_i(0) = 0$ K and without an external rf field. The resonance frequency ω_0 was estimated and appeared to be close to the value of the Mie-frequency ω_m.

The second requirement was that the field frequency $\omega_d > \omega_m$, to make sure that no part of the plasma was at a Mie-resonance with the applied field.

The total energy change of the plasma was studied for different field amplitudes, which implies different quiver velocities v_{osc}. The energy gain was found to be rapidly oscillating on top of a gradual increase. This gradual increase could be filtered out by analyzing and removing parts of the Fourier spectrum of the energy gain, resulting in an almost linear increase of the energy.

The collision frequency significantly decreases as function of applied rf field amplitude. An explanation is that the Rutherford cross section for electron-ion collisions ($\sigma_R \sim 1/v_{rel}^4$) decreases due to the addition of an (increasing) quiver velocity and in consequence the electron-ion frequency decreases too. The total energy gain increased as a function of v_{osc} for small fields, or values of v_{osc}, but started to *decrease* as a function v_{osc} for very strong fields thereby confirming the predictions from the recent analytical theories of collisional absorption in UCPs [8].

A direct comparison of the simulations was made with the analytical theory. The general behavior of the simulation in figure 5.11 in the decrease of the effective collision frequency is obtained, but there is a large uncertainty in the simulation data. One of the problems is that the analytical theory assumes a certain constant electron temperature during the process of collisional absorption, but as a matter fact this electron temperature increases too as a result of the absorption. Especially for larger fields this effect becomes significant.

The second problem is that the amount of electrons inside the plasma is not constant, since a significant part of the electrons escape from the plasma due to their initial temperature. As a result, the density becomes non-uniform as well as the Mie-frequency and both values need to be averaged over the simulation time.

These effects arise in principle from the existence of the boundary of the plasma in our simulation. The analytical theories are all derived from the assumption of an infinitely extended plasma. The infinite plasma could be mimicked by making use of periodic boundaries. The implementation of periodic boundaries is straightforward for molecular dynamics of particles interacting with short-range (e.g. Lennard-Jones or VanderWaals) potentials, but unfortunately it is far from trivial for particles interacting with longe-range potentials such as the Coulombic potentials [47].

Conclusions and Recommendations

Numerical simulations were performed to investigate the different heating mechanism of the electrons occurring in rf-driven ultracold plasmas.

Before the introduction of an external rf-field, the intrinsic heating mechanisms of the numerical plasma were studied. Two heating mechanisms were observed: disorder-induced heating and three-body recombination. Disorder-induced heating is related to the uncorrelated state in which the plasma is created by photo-ionization. Due to the random initial positions of the electrons, an excess of potential energy exists in the plasma which is rapidly converted into thermal energy until the total energy in the plasma is equally redistributed between thermal and potential energy. The consequence of disorder-induced heating is that strong coupling between the electrons in the plasma does not develop in ultracold plasmas. The time scale of the disorder-induced heating was found to be on the order of the inverse Mie-frequency, confirming theoretical expectations as well as earlier numerical work [22].

The heating by three-body recombination was studied at times immediately after the disorder-induced heating phase and compared to analytical theories. The binding energy of the electrons was calculated and a kinetic bottleneck could be identified close to analytical predicted value [27], which distinguishes the free electrons from the electrons which are bound to an electron.

Possibilities to prevent or counteract these electron heating mechanisms are far from trivial in contrast to several suggestions made to prevent *ionic* disorder-induced heating [2, 48]. The disorder-induced heating phase cannot be prevented due to the nature of the photo-ionization process. The only suggestion so far to reduce the *electron* heating is based on the occurrence of the three-body recombination [28]. The idea is to deliberately add highly-bound Rydberg atoms to the plasma. These atoms will be ionized due to the collisions with free electrons in the plasma and those electrons will loose energy in this collision.

In the next two chapters an external rf field was introduced to study two different absorption mechanisms: collisionless absorption an collisional absorption.

The first of these processes can be interpreted as energy absorption due to the collision of an electron with the boundary of the plasma. Ultracold plasmas do not remain neutral and develop a certain positive plasma potential that keeps the lighter electrons trapped in the plasma. As a result the electron start to oscillate in this potential, the energy absorption arises due to the disturbance by the rf field on this electron oscilla-

tion. The amount of energy absorption depends strongly on the ratio of the harmonic resonance frequency of the plasma potential with the rf field frequency. In a harmonic plasma potential there is only net absorption *exactly* at the resonance frequency, but for the more realistic error potential a significant net absorption was also found for rf field frequencies close to the harmonic resonance frequency.

Therefore a rf field frequency was chosen significantly larger than the natural frequency of the plasma, to study the process of collisional absorption for different rf field amplitudes. It was found that the electron-ion collision frequency is suppressed by the application of an rf field due to a decreasing Rutherford cross-section for electron-ion collisions. Therefore, the amount of energy absorption was less than might intuitively be expected and for very strong rf fields the amount of collisional absorption even decreased as a function of field amplitude. Predictions from analytical theories could be confirmed, although the relative uncertainty for a direct verification of the analytical expression for the collision frequency.

The solution might be to use periodic boundary condition, although the implementation of periodic boundary conditions is problematic for particles exerting Coulomb forces [47].

Eventually, the goal is to study the radiative acceleration of an ultracold plasma. Therefore it is necessary to develop a particle tracer method that takes into account the retardation effects, that is by using the Liénard-Wiechert potentials to calculate the inter-particle forces instead of Coulomb potentials.

Bibliography

[1] P. M. Bellan, *Fundamentals of Plasma Physics*. Cambridge University Press, 1st ed., 2008.

[2] T. C. Killian, T. Pattard, T. Pohl, and J. M. Rost, "Ultracold neutral plasmas," *Physics Reports*, vol. 449, pp. 77–130, 2007.

[3] T. C. Killian, S. Kulin, S. D. Bergeson, L. A. Orozco, C. Orzel, and S. L. Rolston, "Creation of an ultracold neutral plasma," *Phys. Rev. Lett.*, vol. 83, no. 23, 1999.

[4] H. J. Metcalf and P. van der Straten, *Laser Cooling and Trapping*. Springer-Verlag New York inc., 1st edition ed., 1999.

[5] P. W. Smorenburg, *Coherent phenomena in the interaction of pulsed particle beams and radiation*. PhD thesis, Eindhoven University of Technology, April 2013.

[6] Morawetz, "Relation between classical and quantum particle systems," *Phys. Rev. E.*, vol. 66, 2002.

[7] S. X. Hu, B. Militzer, V. N. Goncharov, and S. Skupsky, "Strong coupling and degeneracy effects in inertial confinement fusion implosions," *Phys. Rev. Lett.*, vol. 104, 2010.

[8] P. W. Smorenburg, L. P. J. Kamp, and O. J. Luiten, "Heating mechanisms in radio-frequency-driven ultracold plasmas," *Phys. Rev. A.*, vol. 85, 2012.

[9] G. Taban, M. P. Reijnders, B. Fleskens, S. B. Van der Geer, O. J. Luiten, and E. J. D. Vredenbregt, "Ultracold electron source for single-shot diffraction studies," *EPL*, vol. 91, 2010.

[10] P. W. Smorenburg, L. P. J. Kamp, and O. J. Luiten, "Ponderomotive manipulation of cold subwavelength plasmas," *Phys. Rev. E.*, vol. 87, 2013.

[11] S. B. van der Geer and M. J. de Loos, *General Particle Tracer*. Pulsar Physics, 3.10 x32 ed., 2011.

[12] J. Barnes and P. Hut, "A hierarchical *O(N log N)* force-calculation algorithm," *Nature*, vol. 324, pp. 446–449, 1986.

[13] J. D. Jackson, *Classical Electrodynamics*. John Wiley and Sons, 3rd edition ed., 1999.

[14] W. K. H. Panofsky and M. Philips, *Classical Electricity and Magnetism*. Dover Publications, Inc., 2nd edition ed., 1962.

[15] T. Pohl, T. Pattard, and J. M. R. Rost, "Kinetic modeling and molecular dynamics simulation of ultracold neutral plasmas including ionic correlations," *Phys. Rev. A.*, vol. 70, 2004.

[16] M. S. Murillo, "Ultrafast dynamics of strongly coupled plasmas," *Phys. Rev. Lett.*, vol. 96, 2006.

[17] T. B. Mitchell, J. J. Bollinger, X. P. Huang, W. M. Itano, and D. H. E. Dubin, "Direct observations of the structural phases of crystallized ion plasmas," *Phys. Plasmas*, vol. 6, no. 5, 1999.

[18] K. Huang, *Statistical Mechanics*. John Wiley and Sons, 2nd ed., 1987.

[19] M. Bonitz, "Correlation time approximation in non-markovian kinetics," *Phys. Lett. A*, vol. 221, 1996.

[20] M. S. Murillo, "Using fermi statistics to create strongly coupled ion plasmas in atom traps," *Phys. Rev. Lett.*, vol. 87, 2001.

[21] Y. C. Chen, C. E. Simien, S. Laha, P. Gupta, Y. N. Martinez, P. G. Mickelson, S. B. Nagel, and T. C. Killian, "Electron screening and kinetic-energy oscillations in a strongly coupled plasma," *Phys. Rev. Lett.*, vol. 93, 2004.

[22] S. G. Kuzmin and T. M. O'Neil, "Numerical simulation of ultracold plasmas: How rapid intrinsic heating limits the development of correlation," *Phys. Rev. Lett.*, vol. 88, no. 6, 2002.

[23] M. Mitchner and C. H. Kruger, *Partially Ionized Gases*. John Wiley and Sons, 1973.

[24] E. Hinnov and J. G. Hirschberg, "Electron-ion recombination in dense plasmas," *Phys. Rev.*, vol. 125, no. 3, 1962.

[25] D. R. Bates, A. E. Kingston, and R. W. P. McWhirter, "Recombination between electrons and atomic ions," *Proc. Royal Society of London Series A.*, vol. 267, 1962.

[26] P. Mansbach and J. Keck, "Monte-carlo trajectory calculations of atomic excitation and ionization by thermal electrons," *Phys. Rev.*, vol. 181, no. 1, 1969.

[27] G. Bannasch and T. Pohl, "Rydberg atom formation in stronlgy correlated ultracold plasmas," *Phys. Rev. A.*, vol. 84, 2011.

[28] T. Pohl, D. Comparat, M. Zahzam, T. Vogt, P. Pillet, and T. Pattard, "Use of rydberg atoms to control electron temperatures in ultracold plasmas," *Eur. Phys. J. D.*, vol. 40, 2006.

[29] P. Mulser and M. Kanapathipillai, "Collisionless absorption in clusters out of linear resonance," *Phys. Rev. A.*, vol. 71, 2005.

[30] P. Mulser, D. Bauer, and H. Ruhl, "Collisionless laser-energy conversion by anharmonic resonance," *Phys. Rev. Lett.*, vol. 101, 2008.

[31] D. F. Zaretsky, P. A. Korneev, S. V. Popruzhenko, and W. Becker, "Landau damping in thin films irradiated by a strong laser field," *J. Phys. B.: At. Mol. Opt. Phys.*, vol. 37, 2004.

[32] D. N. Walker, R. F. Fernsler, D. D. Blackwell, W. E. Amatucci, and S. J. Messer, "On collisionless energy absorption in plasmas: Theory and experiment in spherical geometry," *Phys. Plasmas*, vol. 13, 2006.

[33] D. Bauer and P. Mulser, "Vacuum heating versus skin layer absorption of intense femtosecond laser pulser," *Phys. Plasmas*, vol. 14, 2007.

[34] P. B. Parks, T. E. Cowan, R. B. Stephens, and E. M. Campbell, "Model of neutron-production rates from femtosecond-laser-cluster interactions," *Phys. Rev. A.*, vol. 63, 2001.

[35] D. F. Zaretsky, P. A. Korneev, and S. V. Popruzhenko, "Collisionless absorption of intense laser radiation in nanoplasma," *Quantum Electronics*, vol. 37, 2007.

[36] P. Mulser and D. Bauer, *High power laser-matter interaction.* Springer, 1st ed., 2010.

[37] J. J. Sakurai, *Modern Quantum Mechanics, revised edition.* Addision-Wesly, 1994.

[38] R. Shankar, *Principles of Quantum Mechanics.* Springer Science and Business Media, Inc., 2nd edition ed., 1994.

[39] L. D. Landau and E. M. Lifshitz, *Quantum Mechanics*, vol. 3. Pergamon Press Ltd., 3rd ed., 1977.

[40] P. A. Korneev, S. V. Popruzhenko, D. F. Zaretsky, and W. Becker, "Collisionless heating of a nanoplasma in laser-irradiated clusters," *Laser. Phys. Lett.*, vol. 2, no. 9, 2005.

[41] C. L. Philips, J. M. Parr, and E. A. Riskin, *Signals, Systems and Transforms.* Pearson Prentice Hall, 4th edition ed., 2008.

[42] J. A. Bittencourt, *Fundamentals of Plasma Physics*. Springer-Verlag New York, inc, 2004.

[43] D. R. Nicholson, *Introduction to Plasma Theory*. John Wiley and Sons, 1983.

[44] V. P. Silin, "Non-linear high-frequency plasma conductivity," *Sov. Phys. JETP*, vol. 20, 1965.

[45] P. Mulser, F. Cornolti, E. Bsuelle, and R. Schneider, "Time-dependent electron-ion collision frequency at arbitrary laser intensity-temperature ratio," *Phys. Rev. E.*, vol. 63, 2000.

[46] H. Goldstein, C. Poole, and J. Safko, *Classical Mechanics*. Addison Wesley, 3rd ed., 2000.

[47] M. Mazars, "Long ranged interactions in computer simulations and for quasi-2d systems," *Physics Reports*, vol. 500, 2011.

[48] G. Bannasch, T. C. Killian, and T. Pohl, "Strongly coupled plasma via rydberg blockade of cold atoms," *Phys. Rev. Lett.*, vol. 110, 2013.

Appendix

A.1 Thomson derivation of the probability s_1 of a thermalizing collision

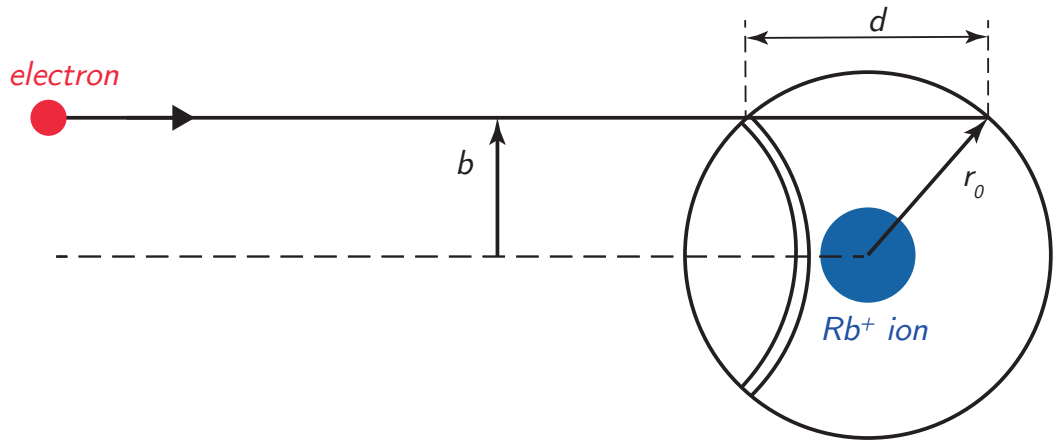

Figure A.1: *Probability of a thermalizing collision.*

The probability s_1 can be calculated with the aid of figure (A.1). A incoming electron having an impact parameter b approaches the R_b^+ ion and travels through the 'Thomson sphere' with radius r_0 ($> b$). Under the assumption of negligible deflection, the electron covers distance a $d = 2\sqrt{r_0^2 - b^2}$ through the sphere in which a thermalization can occur.

A mean free path l is defined, which is the distance over which the amount of non-thermalized electrons in the Thomson sphere decreases to $1/e$ part of the electrons that entered the sphere. In consequence the probability equals $e^{-d/l}$ that an electron with a specific impact parameter b does not experience a thermalization during its way through the sphere.

The probability of having a impact parameter between b and $b + \mathrm{d}b$ is $2\pi b\mathrm{d}b/\pi r_0^2$ and

as result s_1 becomes:

$$s_1 = 1 - \frac{2}{r_0^2}\int_0^{r_0} be^{-2\sqrt{r_0^2-b^2}/l}\mathrm{d}b = 1 + 2\left(\frac{e^{-\beta}}{\beta^2} + \frac{e^{-\beta}}{\beta} - \frac{1}{\beta^2}\right) \tag{A.1}$$

in which $\beta = 2r_0/l$. This parameter is very small for plasmas at low densities and by applying $\beta \ll 1$ equation (A.1) becomes:

$$s_1 \cong \frac{4r_0}{3l} \tag{A.2}$$

From equations (3.15) and (A.2) the Thomson result is found:

$$\alpha_{ei} = \overline{v}_e \frac{4\pi r_0^3}{3l} \tag{A.3}$$

The mean free path for electron-electron momentum transfer can be written as [23]:

$$l \cong \frac{1}{n_e \overline{Q}_{ee}} \tag{A.4}$$

in which $\overline{Q}_{ee}$ is the energy-averaged electron-electron momentum transfer cross section. It is the cross-section in which a incident electron loses momentum in the incident propagation direction. The value of $\overline{Q}_{ee}$ for a collision with a screened Coulomb potential can be found in standard plasma physics textbooks [42]:

$$\overline{Q}_{ee} \cong 6\pi \bar{b}_0^2 \ln(\Lambda) = \frac{3\pi}{2} r_0^2 \ln(\Lambda_e) \tag{A.5}$$

It must be noted that those derivations are based on the assumption of the existence of a screened electron potential with a Debye length λ_D. The existence of this screening effect follows from the assumption that thermal energy $k_b T_e$ is larger than the typical potential energy; that is for $\Gamma_e^{-1} > 1$.

Finally, substitution of equations (3.12), (A.2), (A.5) into equation (A.3) and numerical evaluation of the physical constants gives the Thomson result:

$$\alpha_{Th} = 2.1 \cdot 10^{-20} \frac{n_e}{T_e^{9/2}} \ln(\Lambda_e) \tag{A.6}$$

It is important to note that the Thomson derivation does not take into account the re-ionizations of electrons with a an energy above the kinetic bottleneck as shown in figure 3.7 and an overestimation of the electron-ion recombination coefficient could be expected.

A.2 Electron transitions in the perturbed harmonic potential

The matrix element $|\langle f^0|x|i^0\rangle|^2$ can be calculated if the states $|i^0\rangle$ are known explicitly. For an electron in an harmonic oscillator the different eigenstates $\Psi_n(x)$ are proportional

to the Hermite polynomials $H_n(\xi)$ [38]:

$$\Psi_n(x) = \left(\frac{m_e\omega_0}{\pi\hbar 2^{2n}(n!)^2}\right)^{1/4} \exp\left(-\frac{m_e\omega_0}{2\hbar}x^2\right) H_n\left[\sqrt{\frac{m_e\omega_0}{\hbar}}x\right] \tag{A.7}$$

The Hermite polynomials preserve the orthogonality for the different eigenstates. The following recursion relations apply to the Hermite polynomials [38]:

$$\begin{aligned} 2yH_n(y) - 2nH_{n-1}(y) &= H_{n+1}(y) \\ \int_{-\infty}^{\infty} H_n(y)H_n'(y)\exp\left(-y^2\right)\mathrm{d}y &= \sqrt{\pi}2^n n!\delta_{n,n'} \end{aligned} \tag{A.8}$$

$$\langle k|x|n\rangle = \int_{-\infty}^{\infty} H_k\left(\sqrt{\frac{m_e\omega_0}{\hbar}}x\right) H_n\left(\sqrt{\frac{m_e\omega_0}{\hbar}}x\right) \frac{\sqrt{\frac{m_e\omega_0}{\hbar}}x\exp\left(-\frac{m_e\omega_0}{\hbar}x^2\right)}{\sqrt{\pi}2^{n+k}n!k!}\mathrm{d}x \tag{A.9}$$

Using the substitution $\Delta = \sqrt{\frac{\hbar}{m_e\omega_0}}$ and immediately after that a second substitution $y = \frac{x}{\Delta}$:

$$\begin{aligned} \langle k|x|n\rangle &= \int_{-\infty}^{\infty} H_k\left(\frac{x}{\Delta}\right) H_n\left(\frac{x}{\Delta}\right) \frac{x\exp\left(-\frac{x^2}{\Delta^2}\right)}{\sqrt{\pi}\Delta 2^{n+k}n!k!}\mathrm{d}x \\ &= \frac{\Delta}{\sqrt{2^{n+k}\pi n!k!}} \int_{-\infty}^{\infty} H_k\left(y\right) H_n\left(y\right) y\exp\left(-y^2\right)\mathrm{d}y \end{aligned} \tag{A.10}$$

Using the first relation from equation (A.8), which can also be written as $yH_n(y) = \frac{1}{2}\left(H_{n+1}(y) + 2nH_{n-1}(y)\right)$:

$$\langle k|x|n\rangle = \frac{\Delta}{\sqrt{2^{n+k}\pi n!k!}} \int_{-\infty}^{\infty} H_k\left(y\right) \frac{1}{2}\left[H_{n+1}(y) + 2nH_{n-1}(y)\right]\exp\left(-y^2\right)\mathrm{d}y \tag{A.11}$$

From performing the integral with the second (normalization) condition of equation (A.8):

$$\begin{aligned} \langle k|x|n\rangle &= \frac{\Delta}{\sqrt{2^{n+k}\pi n!k!}}\left[\frac{1}{2}\sqrt{\pi}2^k k!\delta_{k,n+1} + n\sqrt{\pi}2^k k!\delta_{k,n-1}\right] \\ &= \frac{\Delta}{2}\left[\sqrt{2(n+1)}\delta_{k,n+1} + \frac{2n}{\sqrt{2n}}\delta_{k,n-1}\right] \\ &= \sqrt{\frac{\hbar}{2m_e\omega_0}}\left[\delta_{k,n+1}\sqrt{n+1} + \delta_{k,n-1}\sqrt{n}\right] \end{aligned} \tag{A.12}$$

A.3 Mulser-Bauer theory

The change in kinetic energy is given by

$\frac{1}{2}m_e\left(\vec{v}^2(t') - \vec{v}^2(t)\right) = \frac{1}{2}m_e\Delta\vec{v}^2$ and $\Delta\vec{v}^2$ becomes:

$$\begin{aligned}\Delta\vec{v}^2 =& 2\vec{v}_{osc}^2\sin^2(\omega_d t_0) - 2\vec{e_i}\cdot\vec{v}_{osc}v_0\left[\sin(\omega_d t_0) - \sin(\omega_d t)\right] \\ &- 2\vec{e_f}\cdot\vec{v}_{osc}\left|v_0\vec{e_i} - \sin(\omega_d t_0)\vec{v}_{osc}\right|\left[\sin(\omega_d t') - \sin(\omega_d t_0)\right] \\ &+ \vec{v}_{osc}^2\left[\sin^2(\omega_d t') - \sin^2(\omega_d t)\right] - 2\vec{v}_{osc}^2\sin(\omega_d t')\sin(\omega_d t_0)\end{aligned} \tag{A.13}$$

where t is a certain time *before* the collision at time t_0 and t' is a certain time *after* the collision. In the hard-sphere model the electron does not feel any potential force from the ion before the collision at t_0, so the time $t < t_0$ before the collision can be any time arbitrarily close to t_0. By taking the limit $t \to t_0$, equation (A.13) simplifies to:

$$\begin{aligned}\Delta\vec{v}^2 =& 2\vec{v}_{osc}^2\sin^2(\omega_d t_0) - 2\vec{e_f}\cdot\vec{v}_{osc}\left|v_0\vec{e_i} - \sin(\omega_d t_0)\vec{v}_{osc}\right|\left[\sin(\omega_d t') - \sin(\omega_d t_0)\right] \\ &+ \vec{v}_{osc}^2\left[\sin^2(\omega_d t') - \sin^2(\omega_d t_0)\right] - 2\vec{v}_{osc}^2\sin(\omega_d t')\sin(\omega_d t_0)\end{aligned} \tag{A.14}$$

The direction of reflection $\vec{e_f}$ is in an arbitrary direction due to the $\sin(\omega_d t_0)$ term in equation (5.2): t_0 can be chosen arbitrarily. Therefore, $\Delta\vec{v}^2$ needs to be averaged over one oscillation period of the rf field $2\pi/\omega_d$:

$$\begin{aligned}\frac{\omega}{2\pi}\int_{t_0}^{t_0+2\pi/\omega}\Delta\vec{v}^2\mathrm{d}t_0 =& \vec{v}_{osc}^2 - 2\vec{e_f}\cdot\vec{v}_{osc}\overline{\left|v_0\vec{e_i} - \sin(\omega_d t_0)\vec{v}_{osc}\right|}\sin(\omega_d t') + \vec{v}_{osc}^2\sin^2(\omega_d t') \\ &+ 2\vec{e_f}\cdot\vec{v}_{osc}\overline{\left|v_0\vec{e_i} - \sin(\omega_d t_0)\vec{v}_{osc}\right|\sin(\omega_d t_0)} - \frac{1}{2}\vec{v}_{osc}^2 = \Delta\vec{v}^2(t')\end{aligned} \tag{A.15}$$

where the long bar above the second and fourth term indicates that the time t_0 in these expressions needs to be averaged over one rf cycle.

The time after the collision can be any value $t' > t_0$, so t' has to be averaged over one rf cycle too:

$$\overline{\Delta\vec{v}^2(t')} = \frac{\omega}{2\pi}\int_{t'}^{t'+2\pi/\omega}\Delta\vec{v}^2(t')\mathrm{d}t' = \vec{v}_{osc}^2 + 2\vec{e_f}\cdot\vec{v}_{osc}\overline{\left|v_0\vec{e_i} - \sin(\omega_d t_0)\vec{v}_{osc}\right|\sin(\omega_d t_0)} \tag{A.16}$$

For a weak electric field $|\vec{v}_{osc}| \ll |\vec{v}_0|$ the last term in equation (A.16) can be approximation by a Taylor expansion:

$$\begin{aligned}\left|v_0\vec{e_i} - \vec{v}_{osc}\sin(\omega_d t_0)\right| &= v_0\left\{1 - 2\frac{|\vec{v}_{osc}|}{v_0}\cos(\vec{e_i},\vec{v}_{osc})\sin(\omega_d t_0)\right\}^{\frac{1}{2}} \\ &= v_0 - |\vec{v}_{osc}|\cos(\vec{e_i},\vec{v}_{osc})\sin(\omega_d t_0)\end{aligned} \tag{A.17}$$

where $(\vec{e_i}, \vec{v}_{osc})$ is the angle between the incoming electron and the polarization of the electric field. The substitution of this expression into equation (A.16) results in:

$$\begin{aligned}\overline{\Delta\vec{v}^2} &= \vec{v}_{osc}^2 + 2\vec{e_f}\cdot\vec{v}_{osc}\overline{[v_0 - |\vec{v}_{osc}|\cos(\vec{e_i},\vec{v}_{osc})\sin(\omega t_0)]\sin(\omega_d t_0)} \\ &= \vec{v}_{osc}^2 + 2\vec{e_f}\cdot\vec{v}_{osc}\overline{\left[v_0\sin(\omega_d t_0) - |\vec{v}_{osc}|\cos(\vec{e_i},\vec{v}_{osc})\sin^2(\omega_d t_0)\right]} = \vec{v}_{osc}^2 + \vec{e_f}\cdot\vec{v}_{osc}\,|\vec{v}_{osc}|\,\overline{\cos(\vec{e_i},\vec{v}_{osc})} \\ &= \vec{v}_{osc}^2\end{aligned} \tag{A.18}$$

since the average angle between the electric field and the incoming angle $\overline{\cos(\vec{e_i},\vec{v}_{osc})} = 0$. The net energy gain of the electron after the collision equals $\frac{1}{2}m_e\overline{\Delta\vec{v}^2}$ and can be written as:

$$\frac{1}{2}m_e\overline{\Delta\vec{v}^2} = \frac{1}{2}m_e\vec{v}_{osc}^2 = \frac{\left(eE'\right)^2}{2m_e\omega_d^2} = 2U_p \tag{A.19}$$

where $U_p = (eE_0)^2/(4m_e\omega_d^2)$ is the ponderomotive potential that was briefly mentioned in section 4.2.